THE UNIVERSITY *of* EDINBURGH

Impact of network structure and fluid properties on two-phase flows in complex networks

Cong Chao

A thesis submitted for the Degree of Doctor of Philosophy

The University of Edinburgh

2019

Declaration

The author declares that the work undertaken in this thesis has been carried out and composed by her unless stated or acknowledged otherwise. This work has not been submitted or accepted in the fulfilment of any other degree or qualification, at any other university.

Acknowledgments

I own a lot of gratitude to my supervisor, Professor Xianfeng Fan, for his unwavering and untiring support for my PhD project. The PhD work, publications and the thesis would not be possible without his patience and supervisions. I deeply appreciate for all the invaluable advice, guidance and encouragement given by my supervisor.

I would like to express my deepest gratitude to my second supervisor, Dr Timm Krüger, for his relentless support and advices throughout the course of this PhD project. I am also thankful to and acknowledge Dr Adam Stokes and his student Lijun Teng for their efforts on the manufacture of microfluidic devices in Chapter 7 of this thesis. I also would like to appreciate for the help provided by technicians in the School of Engineering. They are Kevin Anderson, Scott Cummings, Andy Mullen, and Douglas Carmichael. I am indebted to all the staff of the Institute for Materials and Processes for providing me with the necessary support and care all the times.

I would also like to thank to reviewers and editors from the Journals of Chemical Engineering Science, Langmuir and Lab on the chip. They very constructive and helpful suggestions given by these experts improved my manuscript, and finally made some contents in Chapter 4, Chapter 5, Chapter 6 and Chapter 7 to be published.

Last, I express many thanks to my dear parents, all my friends and families, who sacrificed their precious time and inspired me to complete this study. I would always remember the encouragement and accompany from my mother.

Abstract

Immiscible two-phase flows in porous media is of great importance to many fields, such as water management in fuel cells, micro-reactors, electronic chips, microbubbles-aided drug delivery, oil recovery, CO_2 sequestration, and underground water remediation. The transport of two-phase flows in the porous media directly affects the system performance, heat and mass transfer efficiency. Resistance to a two-phase flow is normally regarded as the criterion to evaluate the transport performance of two-phase flows, and it is measured by the pressure drop for fluids flowing through the system. This PhD thesis experimentally and theoretically investigates the effect of two-phase interfaces on pressure resistance in both constricted microchannels and complex capillary networks, the effect of fluid properties, network structure and channel geometry on fluid transport and the pressure drop, evaluates the pressure drop required for dislodging a bubble from the complex capillary network and estimates the pressure distribution in a complex capillary network.

Two-phase interfaces play a significant role for two-phase flow in porous media, especially when the porous media possess pore with a diameter less than “the effective pore throat”, irregular pore shape, complex flow path structure, and interconnected channels, etc. Investigations of the effect of interface on the pressure drop in constricted microchannels (i.e. microchannel with a gradually decreasing pore size) indicate that the capillary force applied to a two-phase flow is mainly due to the interface. If a flow channel with a diameter is larger than the “effective pore throat”, the capillary resistance to the interface, or to the two-phase flow, is almost zero. If the flow channel has a pore size less than the “effective pore throat”, capillary force to two-

phase interfaces takes significant effect, and the resistance to two-phase flows increases suddenly when the two-phase interface reaches the effective pore throat. The ‘effective pore throat’ is between 150 to 650 microns depending on capillary tip size and it is very different from the geometrical throat of a channel. To predict the pressure drop for a two-phase flow in constricted capillaries, a new equation has been derived based on Darcy-Weisbach equation to calculate the frictional pressure drop in constricted capillaries. The effect of the capillary tip diameter, capillary gradient, surface tension, viscosity, gas type, and contact angle on the effective pore throat of constricted capillaries has been studied in detail. Experimental measurement indicates that effective pore throat depends on fluid surface tension and the capillary geometry, but not on liquid viscosity. The higher the fluid surface tension, the larger the diameter of the effective pore throat. A channel with a large tip diameter or gradient will give a large effective pore throat diameter. Fluid viscosity only affects the magnitude of the resistant pressure drops of fluid flows in constricted capillaries, but does not affect the effective pore throat diameter. The effective pore throat and the pressure profile measured in this study can be explained by the pore contact angle, but cannot be explained by the contact angle measured on a flat surface of the same materials.

Resistance to two-phase interface in complex capillary network has been investigated further by measuring the pressure drop required to dislodge a bubble (i.e. dislodging pressure) from microfluidic networks with multiple bifurcations. More than 500 individual experiments have been conducted to quantitatively characterize the factors affecting the dislodging pressure from a lab-on-a-chip network. The experimental results indicate that the dislodging pressure is determined by bubble length, channel dimensions, bifurcation, bifurcating angle, surface tension and fluid viscosity. Based on the experimental results, the network structure is a dominant factor. The dislodging

pressure increases with the increase in network complexity. The effect of the network structure, bubble position, proximal channels on the bubble dislodgement in microfluidics networks has been further studied by employing networks with one bifurcation. The results indicate that bifurcations, multiple channels, and curvature of channels, all affect bubble dislodging pressure and the pressure distribution in capillary networks. A parameter *cj* is used to characterize how the overall pressure applied to the system distributes to an individual channel. The c_j value is smaller for the channel with complicated surrounding network, such as multiple bifurcations and multiple microchannels with varied diameters. The c_j value increases with bifurcating angle of microchannel *j*, and a high bifurcating angle results in a decrease of c_j value in the proximal microchannel.

Theoretical investigation on resistance to two-phase interfaces has been conducted in both constricted microchannels and complex capillary network. Theoretical equations have been derived based on Darcy-Weisbach equation to predict the pressure drop in the constricted structure of microchannel. Combined with homogenous flow model and separated flow model, our newly-derived equation can be used to predict the pressure drop for two-phase flows in constricted microchannels with the deviation of below ±20%. For complex capillary network, a theoretical equation has been derived, and it indicates that the bubble dislodging pressure is the function of bubble length, channel dimension, and network structure. The equation theoretically agrees well with the experimental results. The effect of network structure on the pressure drop was characterized by introducing the parameter, c_j. The analysis of model parameters NB_j and MA_j shows that parameter c_j, rather than the channel size, dominates the dislodging pressure for bubbles with a length greater than 2 mm, and the increase rate

of the dislodging pressure is significantly affected by both channel size and parameter c_j.

Table of Contents

List of Publications

Journal Papers:

1. **C. Chao**, X. Xu, S. O. Kwelle, X. F. Fan, Significance of gas-liquid interfaces for two-phase flows in micro-channels, **Chem. Eng. Sci.** 192 (**2018**) 114-125.
2. **C. Chao**, G. W. Xu, X. F. Fan, Effect of surface tension, viscosity, pore geometry and pore contact angle on effective pore throat, **Chem. Eng. Sci.** 197 (**2019**) 269-279.
3. **C. Chao**, X. Q. Jin, L. J. Teng, A. A. Stokes, X. F. Fan, Bubble dislodgment in a capillary network with microscopic multi-channel and multi-bifurcation features, **Langmuir** (**2019**) 35 (8), 3194–3203.
4. **C. Chao**, X. Q. Jin, X. F. Fan, Effect of network structure on the bubble dislodgment and pressure distribution in microfluidic networks with multiple bifurcations, **Chem. Eng. Sci.** (**2019**) 115176.
5. X. Q. Jin, **C. Chao**, K. J. Wu, C. Y. Xia; X. F. Fan, The effect of CO_2 phase on drainage process by analysis of transient differential pressure, **Chem. Eng. Sci.** (**2020**) 115581.
6. D. Nagy, **C. Chao**, B. Marzec, F. Nudelman, M. C. Ferrari, X. F. Fan, Effect of Ag Co-catalyst on TiO_2–Cu_2O nanocomposites structure and apparent visible photocatalytic activity, Journal of Environmental Management, **J. Environ. Manage, (2020)**, 260, 110175.
7. **C. Chao**, X. Q. Jin, X. F. Fan, Evolution of liquid film surrounding microbubbles and its impact on pressure drop in laser-etched microfluidics, **Langmuir** (Under review).
8. **C. Chao**, Y. M. Deng, R. Dewil, X. F. Fan, Post-combustion Carbon Capture (Under review).

International conference, papers and presentations

1. **C. Chao**, X. F. Fan, Impact of interface movement on resistant pressure drop in micro-capillaries, UK-China International Particle Technology Forum, Yangzhou, China, Sep, 2017. (Invited talk)
2. Presentation and Poster in Chemical Engineering Research Conference, University of Edinburgh, 04, 2018.
3. Oral presentation in International seminar and workshop on oil and gas, India, April, 2019.
4. **C. Chao**, X. F. Fan, Effect of network structure and pore wetting on the migration and dislodgment of microbubble/droplets in microfluidics and porous media, Nano Petro Science and Technology International Conference and 5th International Symposium on Application of NanoGeosciences in Petroleum Engineering, Beijing, China, Dec, 2019.

List of Figures

List of Tables

Abbreviation list

γ	Surface tension	μ	Dynamic viscosity
μ_m	Dynamic viscosity of mixture	ρ	Fluid density
We	Weber number	*Bo*	Bond number
Ca	Capillary number	*De*	Dean number
Re	Reynolds number	*L*	Length of flow path
f	Darcy friction factor	*r*	Radius of flow path
R_c	Radius of curvature of the microchannel	D	Diameter of flow path
d	Thickness of thin liquid film	φ	Porosity
S_w	Saturation of the wetting phase	*S*	Spreading parameter
HFM	Homogeneous flow model	SFM	Separated flow model
ϕ^2	Two-phase friction multiplier	x	Mass quality of two-phase mixture
m	Fluid mass flow rate	$(\Delta P_f)_{TP}$	Frictional pressure drop for two-phase flows
X	Lockhart-Martinelli parameter	*G*	Total mass flux
$\Delta P_{contraction}$	Pressure drop due to the sudden contraction	C_c	Contraction coefficient
ΔP_c	Capillary pressure drop	ΔP_{loss}	Pressure loss in junctions
ΔP_{total}	Overall pressure drop	ω_j	The average lateral outflow angle
λ_j	Flow ratio	*W*, *H*	Width and height of microchannel
θ_s	Static contact angle	θ_{adv}	Advancing contact angle
θ_{rec}	Receding contact angle	u	Fluid superficial velocity
R_H	Hydraulic resistance	k	Capillary radius gradient
Q	Volumetric flowrate	θ_j	Branch angle of microchannel j

l_b	Bubble length	D_{eff}	Effective dynamic diameter of the corner liquid
c_j	Pressure loss parameter	ΔP_j	Pressure drop in microchannel
ΔP	Overall pressure drop in microfluidic networks	K	Absolute permeability of the microchannel

Chapter 1 Introduction

1.1 Project background and Motivation

Understanding of two-phase flows in porous media is essential in many biological and chemical applications, such as, enhanced oil recovery[1-3], cooling electronics[4], fuel cells[5, 6], microreactors[7], microbubble-aided drug delivery and gas embolotherapy[8-11]. Resistance to two-phase flows is an essential criterion to characterize the flow transport, heat and mass transfer in porous media.

For example, in microbubble-mediated therapy, microbubbles are expected to deliver the therapeutic molecular to the targeted tissues or cells with high therapeutic effect and low undesirable side-effects[12, 13]. The microbubble encapsulates the drugs with hard shell (e.g. PLA[14]), and after arriving the targeted sites, drug-loaded microbubbles rupture and release the drugs with the aid of ultrasound. Microbubble can not only protect the drugs against degradation but also increase the therapeutic effect due to cavitation induced by microbubble rupture, i.e. the enhanced permeation and retention (E.P.R.) effect[15, 16]. However, the blood vessels are composed of thousands of vessels and capillaries which are highly interconnected, and the resistance to microbubble flow maybe too high due to the extremely small diameter of microvessels, especially the micro-capillaries (several microns)[17]. The resistance would stop microbubbles moving further, which may lodge in somewhere of microvessels, and causes the vascular blockage. With the development of lab-on-a-chip technology, microfluidic network can be used to mimic the flow conditions of drug delivery systems in blood vessels based on scaling laws and basic fabrication

technologies[18]. With detailed investigation into the resistance to microbubble flow in microvessels, it is possible to evaluate if the microbubble can be driven by the blood pressure to the targeted tissues. In proton exchange membrane (PEM) fuel cells, one challenge to maintain the performance and durability of fuel cells is the water management on the gas diffusion layer, which is the pathway for reactant gases and liquid water[19, 20]. Understanding the resistance to gas-liquid flows through the porous membrane will provide a new version for designing the passage to optimize the mass transport of gas diffusion layer.

The resistance to microbubbles in a pore network is controlled by pore structure, pore surface properties, fluid properties and the interaction between fluids and pores. Porous network is formed by two sets of elements: pore body and pore throat with various sizes and lengths[21, 22]. Single microchannels have been used to mimic pores and throats, through altering the geometry of microchannels, such as the cross-sectional shape, lengths, and sizes. The complexity in the investigation into two-phase flows in porous media is not only caused by a huge number of pores and throats, but also the complicated connectivity of inner channels, or the network structure, and the interaction between fluids and pore network[23, 24]. The study on the two-phase flows in single microchannels and complex network will help to understand the mechanism of two-phase flows in porous media from two aspects: effect of individual pore on the flow resistance to bubbles and the effect of overall structure on the flow resistance to bubbles.

1.2 Thesis structure

This thesis is structured to 8 chapters.

Chapter 1 introduces the project background, motivations and objectives. Chapter 2 provides the relevant theoretical background and literature review of related work. The fundamentals and principle of multiphase flows in porous media, flow resistance, capillary pressure drop, frictional pressure drop, bubble dislodgment, tree-shaped networks, and related fundamental equations and theories are discussed in Chapter 2. Chapter 3 gives the major experimental methodologies and materials, such as the measurement of pressure drop for air-liquid flows through a constricted capillary.

The main body of this thesis is composed of Chapter 4 to Chapter 7. These four chapters present the experimental results, theoretical modelling, and discussions on the impact of network structure and fluid properties on the resistance to two-phase flows in single microchannels and complex capillary network at the microscopic scale.

Chapter 4 investigates the impact of the fluid interface on the two-phase flows in constricted microchannels through comparing the difference in the pressure drop for single-phase flow and two-phase flow. The effective pore throat has been defined based on the sudden increase in the resistance pressure in the measured pressure profiles, which indicates the threshold of pore size where capillary force starts to take effect in microchannels. Simulations were conducted to predict the two-phase flows in constricted microchannels through combining the new-derived Darcy-Weisbach equation with the homogenous flow model and the separated flow models. Chapter 5 further studies the effect of factors including the surface tension, fluids viscosity, gas

types, capillary gradient and capillary tip diameter, on the size of the effective pore throat.

Chapter 6 and 7 investigate the bubble dislodgment in complex capillary network with multi-microchannel and multi-bifurcation features. Chapter 6 focuses on the experimental investigations on the pressure required to dislodge a bubble from the complex network, and the effect of bubble length, channel sizes and network structures on the dislodging pressure. Chapter 7 further proposed one theoretical equation to illustrate the underlying physics of bubble dislodgment from microfluidic networks. The equation has been validated through the experimental data. In addition, the complexity of the network structure has been characterized by introducing a parameter c_j. It was found that a small c_j value of a microchannel indicates a greater impact of network structure on the bubble dislodgment. The c_j value increases with the bifurcating angle of microchannel j, and a high bifurcating angle results in a decrease of c_j value of the proximal microchannel.

Chapter 8 concludes the main findings and highlights the significance of this study. The limitations of this work are addressed and the future work is therefore pointed out.

1.3 References

1. Andrianov, A., et al., *Immiscible Foam for Enhancing Oil Recovery: Bulk and Porous Media Experiments.* Industrial & Engineering Chemistry Research, 2012. **51**(5): p. 2214-2226.10.1021/ie201872v

2. Farajzadeh, R., et al., *Foam-oil interaction in porous media: Implications for foam assisted enhanced oil recovery.* Advances in Colloid and Interface Science, 2012. **183**: p. 1-13.10.1016/j.cis.2012.07.002

3. Rossen, W.R. and P.A. Gauglitz, *Percolation Theory of Creation and Mobilization of Foams in Porous-Media.* Aiche Journal, 1990. **36**(8): p. 1176-1188.DOI 10.1002/aic.690360807

4. Marcinichen, J.B., et al., *Advances in Electronics Cooling.* Heat Transfer Engineering, 2013. **34**(5-6): p. 434-446.10.1080/01457632.2012.721316

5. Calabriso, A., et al., *Bubbly flow mapping in the anode channel of a direct methanol fuel cell via PIV investigation.* Applied Energy, 2017. **185**: p. 1245-1255.10.1016/j.apenergy.2016.01.042

6. Liang, M.C., et al., *An analytical model for the transverse permeability of gas diffusion layer with electrical double layer effects in proton exchange membrane fuel cells.* International Journal of Hydrogen Energy, 2018. **43**(37): p. 17880-17888.10.1016/j.ijhydene.2018.07.186

7. Kreutzer, M.T., et al., *Inertial and interfacial effects on pressure drop of Taylor flow in capillaries.* Aiche Journal, 2005. **51**(9): p. 2428-2440.10.1002/aic.10495

8. Bull, J.L., *Cardiovascular bubble dynamics.* Crit. Rev. Biomed. Eng., 2005. **33**(4): p. 299-346, http://www.ncbi.nlm.nih.gov/pubmed/15982185

9. Eshpuniyani, B., J.B. Fowlkes, and J.L. Bull, *A bench top experimental model of bubble transport in multiple arteriole bifurcations.* International Journal of Heat and Fluid Flow, 2005. **26**(6): p. 865-872.10.1016/j.ijheatfluidflow.2005.10.002

10. Tay, L.M. and C. Xu, *Coating microbubbles with nanoparticles for medical imaging and drug delivery.* Nanomedicine (Lond), 2017. **12**(2): p. 91-94.10.2217/nnm-2016-0362

11. Boissenot, T., et al., *Ultrasound-triggered drug delivery for cancer treatment using drug delivery systems: From theoretical considerations to practical applications.* J Control Release, 2016. **241**: p. 144-163.10.1016/j.jconrel.2016.09.026

12. Bettinger, T. and F. Tranquart, *Design of Microbubbles for Gene/Drug Delivery.* Adv Exp Med Biol, 2016. **880**: p. 191-204.10.1007/978-3-319-22536-4_11

13. Sirsi, S.R. and M.A. Borden, *State-of-the-art materials for ultrasound-triggered drug delivery.* Adv Drug Deliv Rev, 2014. **72**: p. 3-14.10.1016/j.addr.2013.12.010

14. Eisenbrey, J.R., et al., *Development and optimization of a doxorubicin loaded poly(lactic acid) contrast agent for ultrasound directed drug delivery.* J Control Release, 2010. **143**(1): p. 38-44.10.1016/j.jconrel.2009.12.021

15. Maeda, H., *Toward a full understanding of the EPR effect in primary and metastatic tumors as well as issues related to its heterogeneity.* Advanced Drug Delivery Reviews, 2015. **91**: p. 3-6.10.1016/j.addr.2015.01.002

16. Maeda, H., *Tumor-selective delivery of macromolecular drugs via the EPR effect: background and future prospects.* Bioconjug Chem, 2010. **21**(5): p. 797-802.10.1021/bc100070g

17. Sugihara-Seki, M. and B.M. Fu, *Blood flow and permeability in microvessels.* Fluid Dynamics Research, 2005. **37**(1-2): p. 82-132.10.1016/j.fluiddyn.2004.03.006

18. Nguyen, N.T., et al., *Design, fabrication and characterization of drug delivery systems based on lab-on-a-chip technology.* Adv Drug Deliv Rev, 2013. **65**(11-12): p. 1403-19.10.1016/j.addr.2013.05.008

19. Sinha, P.K., P.P. Mukherjee, and C.Y. Wang, *Impact of GDL structure and wettability on water management in polymer electrolyte fuel cells.* Journal of Materials Chemistry, 2007. **17**(30): p. 3089-3103.10.1039/b703485g

20. Wong, C.W., et al., *Transient capillary blocking in the flow field of a micro-DMFC and its effect on cell performance.* Journal of the Electrochemical Society, 2005. **152**(8): p. A1600-A1605.10.1149/1.1949067

21. Blunt, M.J. and H. Scher, *Pore-level modeling of wetting.* Physical Review E, 1995. **52**(6): p. 6387-6403.10.1103/PhysRevE.52.6387

22. Blunt, M.J., *Flow in porous media - pore-network models and multiphase flow.* Current Opinion in Colloid & Interface Science, 2001. **6**(3): p. 197-207.Doi 10.1016/S1359-0294(01)00084-X

23. Steinbrenner, J.E., et al., *Impact of channel geometry on two-phase flow in fuel cell microchannels.* Journal of Power Sources, 2011. **196**(11): p. 5012-5020.10.1016/j.jpowsour.2011.02.032

24. Senn, S.M. and D. Poulikakos, *Tree network channels as fluid distributors constructing double-staircase polymer electrolyte fuel cells.* Journal of Applied Physics, 2004. **96**(1): p. 842-852.10.1063/1.1757028

Chapter 2 Theory and literature background

2.1 Porous media

Multiphase flows in porous media are very common in natural and industrial systems. Typical examples (as shown in Fig. 2.1) are blood flows which carries oxygen, nutrients and other substances flows in blood vessels, gas and proton exchanging through gas diffusion layer in fuel cells; foam/gas-aided oil recovery in depleting oil fields, and the storage of CO_2 in porous geological formations, etc. The porous reservoir rock contains pores and throats as shown in Fig. 2.1 (b), which creating flow path, accumulating hydrocarbon, and providing sealing mechanism for prohibiting hydrocarbon penetration to surface layers[1]. In proton exchange membrane fuel cells, the gas diffusion layer (GDL) is a very complex porous membrane, which ensures the reactants effectively diffuse to the catalyst layer, as shown in Fig. 2.1(c). The GDLs with a thickness of 100-300 μm, are commonly constructed from porous carbon paper, or carbon cloth with a PTFE coating to avoid the liquid water congestion in the GDL pores[2]. In porous media, Darcy's equation has been used to express the relation of pressure drop and fluid velocity for the flow of two or more immiscible fluids, which was proposed by Henry Darcy in 1856[3].

$$v = -\frac{k}{\mu}(\Delta P - \rho g) \tag{2-1}$$

Where v is the mean fluid velocity, μ is the liquid viscosity, ρ is the fluid density, g is the gravitational acceleration, and k is the permeability of the porous media, which indicates how easily a fluid penetrates the medium. ΔP is the pressure drops for fluids flows through the porous medium.

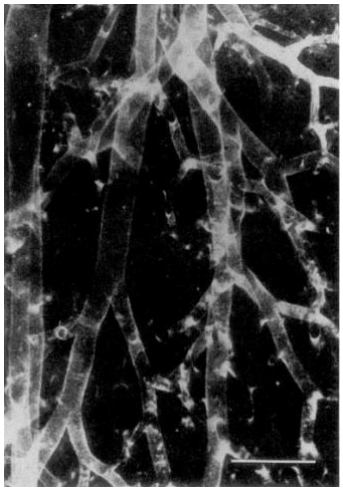

(a)

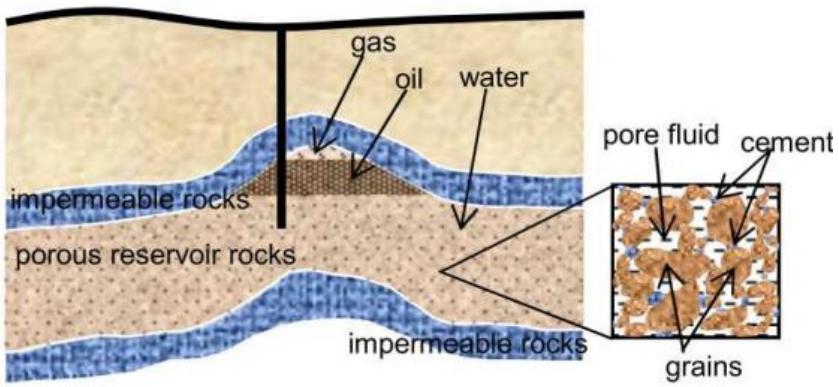

(b)

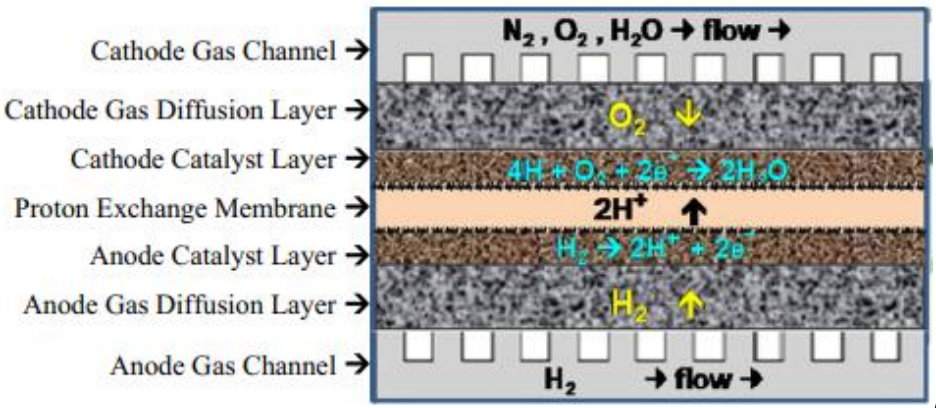

(c)

Fig. 2. 1 (a) Bronchogram of human small airways, scale bar, 1cm[4]; (b) porous oil reservoir rock[5]; (c) composition of gas diffusion layer in proton exchange membrane fuel cells[6]

2.1.1 Pore and Pore Throat

Porous media are composed of solids and the pore voids. The pore voids are commonly segmented into pore (spaces) and pore throats[7, 8]. Pore space is defined

as the volume of voids that can be filled by water or air, and pore throat is the smaller pore which connects two larger pores. The pore spaces govern the value of porosity, and the pore throats control the fluids transport and migration in the media, and therefore the permeability[9]. It is thought that the fluids (oils, liquids and gases) would always be bound in the smaller capillary pores. The transport efficiency of the fluids in the porous media will therefore be affected by the size and types of the pore and pore throats. For example, the porosity in conventional high-quality reservoirs is high, in which the pores are fully connected. Reservoir rocks have pore sizes larger than 30 μm and pore throat sizes larger than 10 μm. With large pore throats, the driving pressure required to overcome capillary resistance to recover the oil would be smaller[10]. However, for tight rocks, the typical size of pore throat may be less than 0.1 μm based on the data shown in Fig. 2.2. The fewer connection of pores and smaller size of pore throat make the multiple phases difficult to deliver or transport in tight rocks and shales. In this way, these types of rocks require further special treatment, such as advanced drilling technology, correct way of completion and stimulation to produce gas in commercial scale[11].

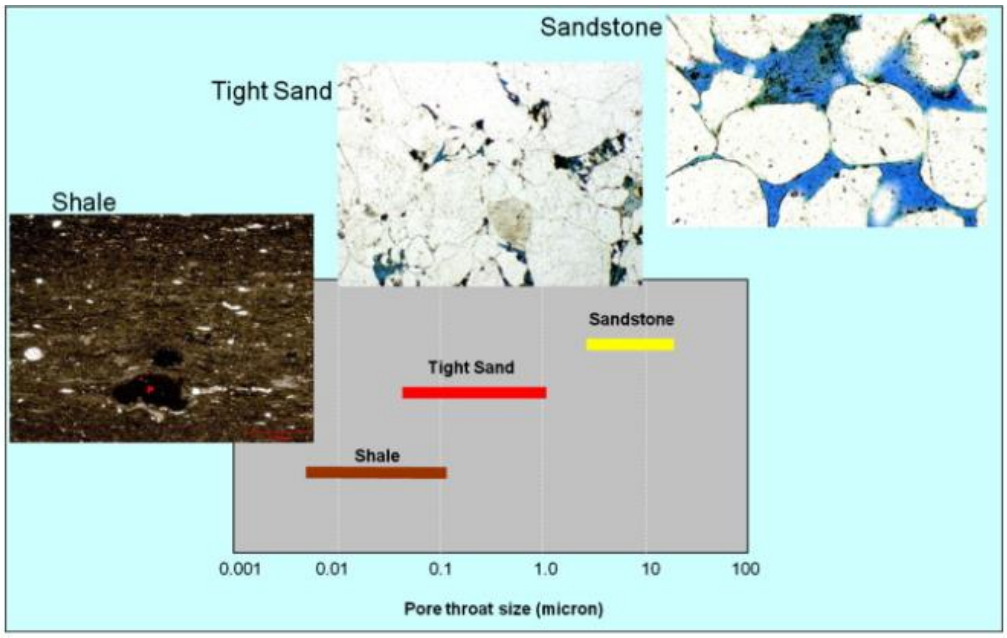

Fig. 2. 2 Pore throat sizes in siliciclastic rocks[11]

Experiments on porous media at pore scale still have some limitations due to the complexity of the multiphase flows processes, the difficulty of measurement at pore scale, and uncertainties in experimental results[12]. Computational and theoretical approaches have been employed as a substitute to obtain a more detailed understanding of multiphase flows in porous media. Computational methods can be classified as, conventional continuum-scale numerical models and pore-scale models in general. Continuum-scale models does not apply at pore scale, therefore, pore-network models are typically employed to mimic the geometrical features of interstitial spaces of porous media. It is composed of pore bodies (large voids) and pore throats (narrow voids) which are connected to pore bodies[7, 8, 12]. The topology of a network can be characterized by the spatial location of pore bodies and the connectivity of pore elements. The geometry of pore network refers to the geometrical shape and size of pore bodies and pore throats. Pore-scale models are of great importance to understand the effect of the geometry and topology of pore space on the physics of multiphase flows. For example, geometrical shape of the pore plays non-negligible role in fluids wetting in porous media. A circular pore can only allow one phase to occupy at one time as shown in Fig 2.3. For a pore with an angular shape or irregular shape, the wetting phase may occupy the corners and the non-wetting phase occupies the main part of the pore[7].

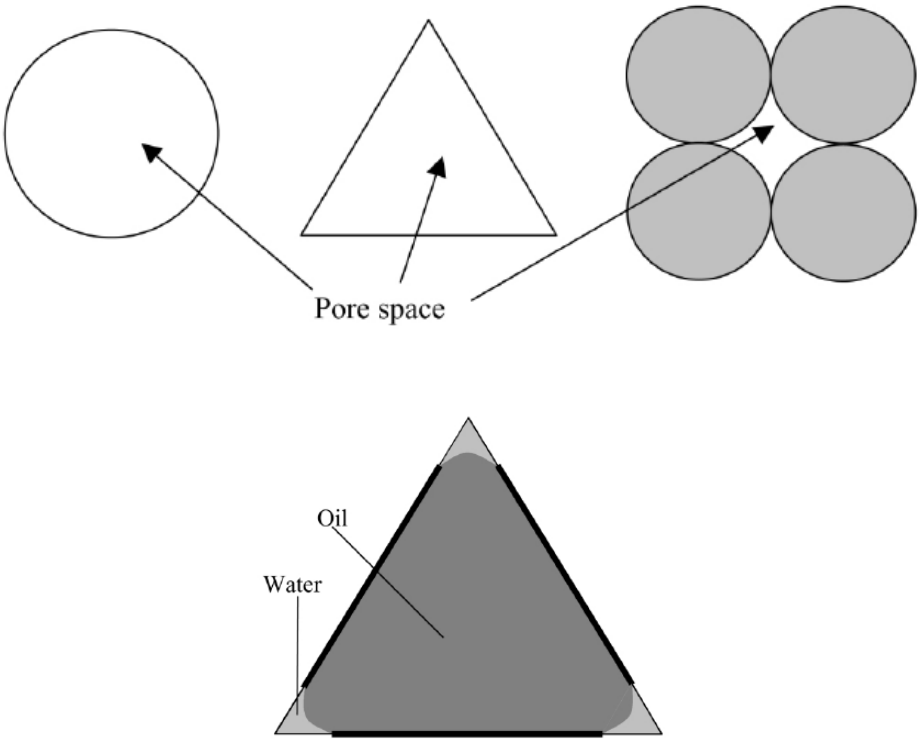

Fig. 2. 3 Cross-sectional view of different types of pore shape[7].

2.1.2 Microchannel and thin films

Investigations on multiphase flows in porous media are commonly conducted from the simplest case-a microchannel/capillary with smooth and clean wall, and regular cross-section. If such a capillary is filled initially with the wetting fluid, nonwetting fluid will be forced to displace the wetting fluid from the capillary, i.e. 'drainage'. Then a thin liquid film will be formed between the microchannel wall and the gas phase. Due to the negligible of gravitational force and shear force of gas phase, the liquid film is commonly assumed to be stagnant and thus does not contribute to the frictional pressure drop [13, 14]. The thickness of this lubricating liquid film (d) in a circular capillary with a diameter D can be calculated through the equation (2-2), which was developed by Bretherton[15],

$$\frac{d}{D} = 0.67Ca^{2/3} \quad (2\text{-}2)$$

The stability of the thin liquid film closely depends on the surface roughness, surface defects, velocity of the non-wetting fluids, as well as the microchannel geometry, etc. Any small perturbation with a wavelength longer than the threshold value λ_{tr} will lead to the rupture of the film because of Waals interactions [16, 17]. For a circular cross-section microchannel, the liquid film is uniform. In the microchannel with rectangular cross-section, the liquid film is not uniform as two local minima in the film thickness (as shown in Fig. 2.4b) occur due to the liquid drainage towards the corners of the channel[17].

$$\lambda_{tr} = \left(\frac{\gamma}{A}\right)^{1/2} h_o^2 \quad (2\text{-}3)$$

where γ is the surface tension, A is the Hamaker constant, and h_o is the initial thickness of the uniform film.

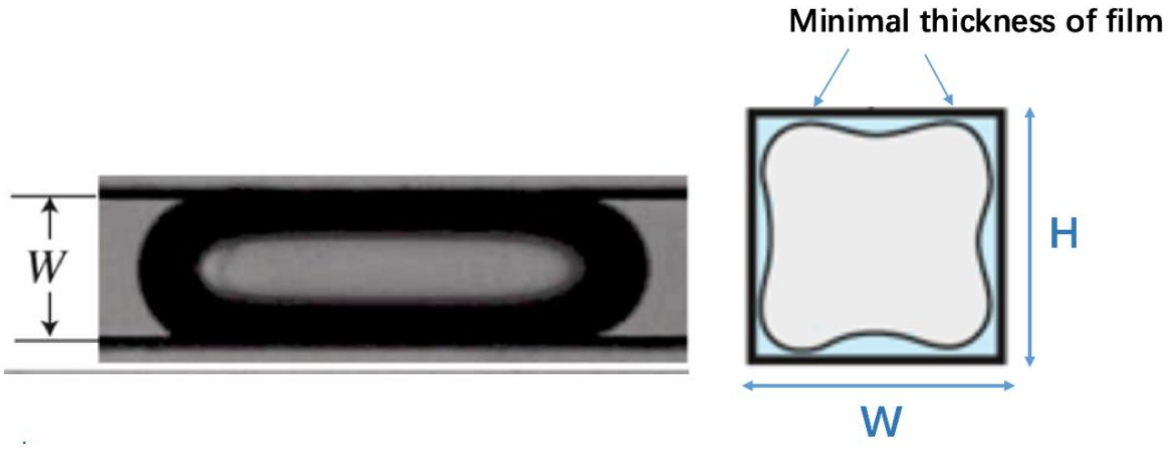

(a) (b)

Fig. 2. 4 (a) Schematic of a bubble in a microchannel with rectangular cross-section[17]; (b) minimal thickness of the liquid film

2.1.3 Microfluidics

The complexity of pore structure can be increased through using a microchannel with irregular cross-section, or capillary network with multiple branches[18] and various bifurcating angles[19-21]. Examples are shown in Fig. 2.5. Microfluidic devices are manufacturing microminiaturized devices containing channels and chambers through which fluids flow or are confined. Microfluidic devices have been frequently used to mimic human arterioles, airways in the lung[22], water distribution networks[23], solar panels, and the cooling of electronics[24], etc. Glass was first used to fabricate microfluidic chips through photolithographic and chemical etching. More recently, polymers, such as polydimethylsiloxane (PDMS) and polymethyl-methacrylate (PMMA), are used as an alternative for fabricating microfluidic systems as they are biocompatible, low-cost and easily treated by several techniques, including injection moulding, soft lithography, laser ablation, X-ray photolithography and hot embossing[25]. As microfluidics always deal with very small volumes of fluids, it has many advantages in using microfluidics, such as lower hardware cost and reagents consumption, shorter response time[26, 27], higher mixing efficiency and lower thermal resistance[28], whereas, these are achieved at the expense of increased pressure drop which may be induced by the parallel or serpentine microchannels. Many research articles focus on the optimization of power requirement and pressure drop in tree-shaped networks through adjusting one factor to achieve the optimal topology, such as channel geometry (height, width, aspect ratios, length, and cross-sectional shape)[29, 30], branch level and branching angles [21, 31]. Due to the potentially large number of degrees of freedom involved in the network design, it is still a very challenging problem.

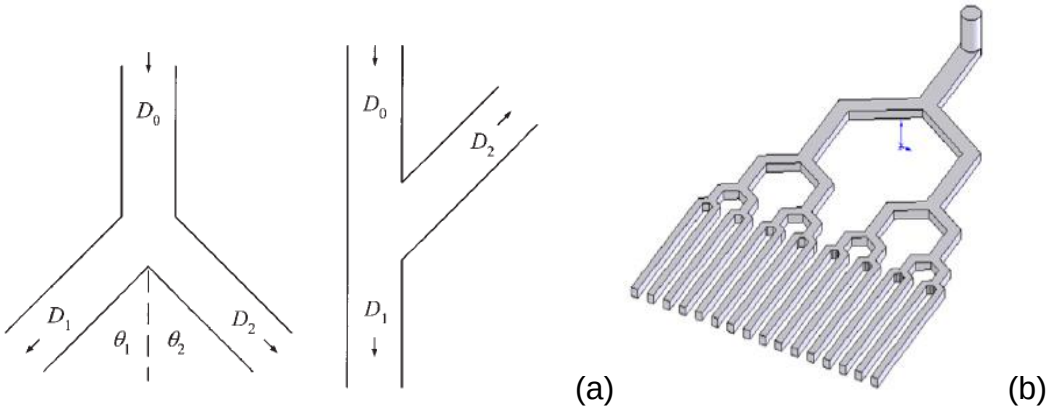

Fig. 2. 5 (a) Y-shaped bifurcation and oblique bifurcation, flow direction is indicated through arrows and D_0, D_1, and D_2 are width of the branches[32]; (b) a symmetrical tree-network with the bifurcating angle of 120˚[20]

2.2 Multiphase flows

2.2.1 Flow patterns

Flow patterns (or flow regime in some references) of a multiphase fluid system is the temporally and spatially geometrical distribution of each phase. The characterization of flow patterns helps to optimize the transport efficacy for multiphase flows, and to validate empirical and numerical models which proposed to predict the pressure drop for multiphase flows in porous media. Flow patterns are dependent on the fluid properties, channel diameters and geometry, operation conditions, etc. Typical flow patterns for two-phase flows are shown in Fig. 2.6, which were recorded in transparent channels through high-speed camera and microscopy.

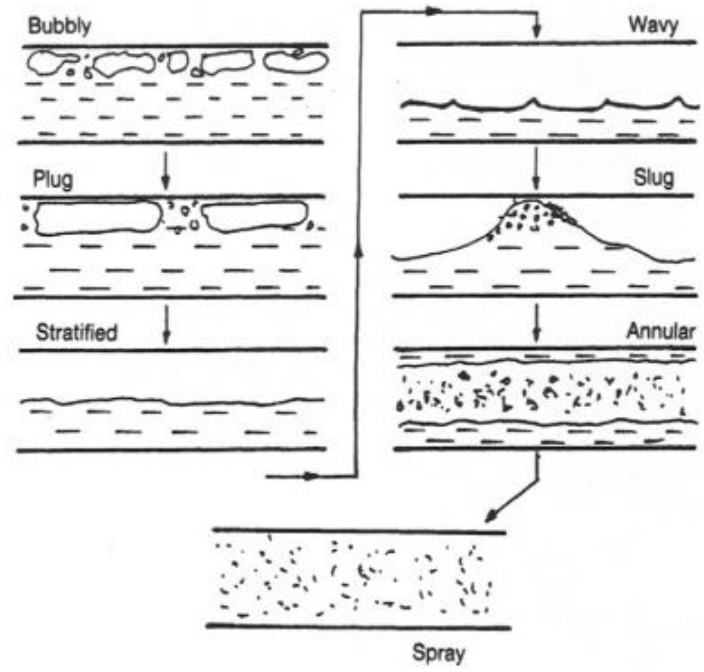

(a)

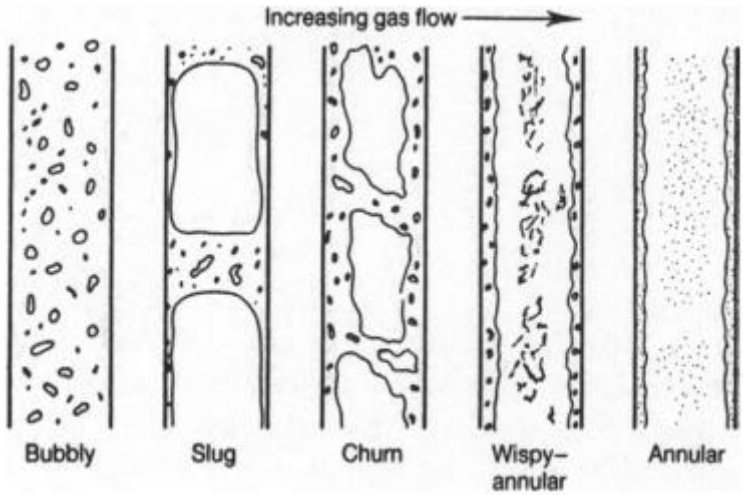

(b)

Fig. 2. 6 Flow patterns in (a) horizontal gas-liquid flow, and (b) vertical gas-liquid flow [33]

In the bubbly flow, there are tiny bubbles with various diameters confined to the region near the top of the channel. With the increase of the gas flowrate, the average size of the bubble becomes larger. Once bubbles coalesce to become a gas plug which will occupy the entire cross-section of the channel, plug flow occurs. On increasing the

gas flowrate, a continuous gas layer forms in the upper part of the channel, which is stratified flow. The interface between the gas and the liquid is smooth for the stratified flow. With the further increase of the gas flowrate, the interfacial shear stress is sufficient to generate waves on the liquid surface, i.e. wavy flow. As the gas flowrate continues to increase, the liquid wave moves in the direction of gas flow until the liquid crest approaches the top of the channel, and this is known as slug flow. Needs to mention, slug flow in vertical flow is different from the same name ‘slug’ flow in horizontal flow, as shown in Fig. 2.6 b. At the higher gas flowrate, annular flow is formed and when the liquid film becomes very thin, the majority of the liquid will be dispersed as droplets in the gas phase, i.e. mist flow[33].

2.2.2 Factors affecting flow resistance

2.2.2.1 Permeability and porosity

One of the most important macroscopic parameter for evaluating the transport capacity of the porous media is permeability. Prediction of the flow behaviour in porous media requires the estimation of the permeability. Direct measurement is often difficult to achieve, or time-consuming especially for porous media with low connectivity[34]. Many attempts to establish a relationship among permeability, porosity, capillary pressure, and water saturation have been made[35, 36].

The types of the reservoirs can be divided by permeability into: conventional reservoir (permeability more than 1 mD), near tight (permeability between 1 and 0.1 mD) and tight reservoirs (permeability less than 0.1 mD), as shown in Fig. 2.7. In most cases, if the large pore space is associated with larger pore throat size, the permeability of

the reservoir will increase with the increase of porosity. However, the relationship is not systematic in some cases. For example, sandstone reservoirs may have large pore space, while the pore throat is small, then the predicted permeability would be greater than it should be if the prediction is based on the large pore spaces. Therefore, a pore throat cutoff method was defined to separate the volumes of the pores for recognizing the abnormal relationship of pore size and pore throats. The pore volumes which are controlled by the large pore throat were termed as macro-porosity. Pore volumes controlled by the small pore throat were termed as micro-porosity[9], and in this case, pore size has no effect as it is controlled by the pore throat size.

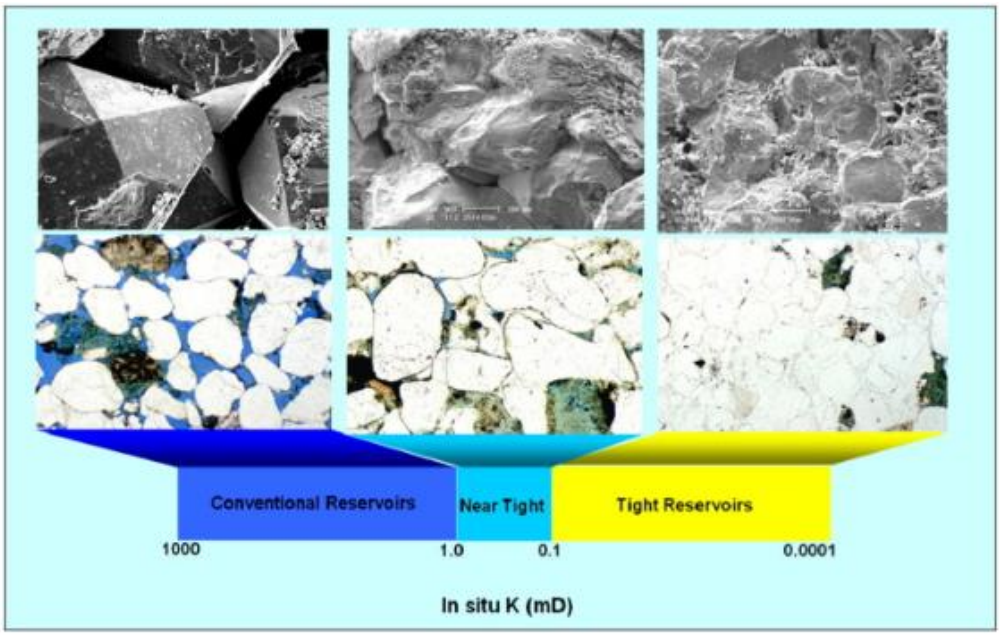

Fig. 2. 7 Indication of conventional reservoir, near tight and tight reservoirs

Coates[37] et al proposed an equation to predict the permeability, given as,

$$K = (10^4)(\varphi^4)\left[(macro - porosity/micro - porosity)^2\right] \quad (2\text{-}4)$$

Where *K* is the permeability in millidarcies, and φ is the porosity. In this equation, the porosity was treated as two parts: macro-porosity which is active in pore network and contributes to the fluids flow, and micro-porosity which does not contribute to fluids flow[35].

Pore-scale modelling is an alternative method to empirical equations for predicting the permeability. Network models represent a void space of a rock by a regular two- or three-dimensional lattice of wide pores which are connected with narrower throats[7]. Normally, the pore or throat will be assumed as the cylindrical or spherical, and the pore sizes are spatially uncorrelated. However, natural porous media have more random topology and correlated pore sizes. To obtain accurate predictions of the permeability, it is very important to determine the detail of pore space geometry, which is the major challenge. In addition, the simple network models based on regular (spherical or cylindrical) lattices have limited ability to predict the macroscopic properties, let alone obtain the accurate prediction.

For two-phase flows in the porous media, for example, rock, the ability of one fluid to flow is reduced due to the presence of the other fluid. Therefore, a relative permeability has been introduced and defined as the ratio between the effective permeability of a given phase and the absolute permeability of the rock. Relative permeability can be calculated based on capillary pressure curves derived from mercury-injection methods through mainly three approaches: Purcell approach, Burdine approach and Mualem model.

Purcell[38]: $k_{rw} = \frac{\int_0^{S_w} dS_w/(P_c)^2}{\int_0^1 dS_w/(P_c)^2}$ (2-5)

Where k_{rw} and S_w are the relative permeability and saturation of the wetting phase, P_c is the capillary pressure as a function of S_w.

Burdine[39]: $k_{rw} = (\lambda_{rw})^2 \frac{\int_0^{S_w} dS_w/(P_c)^2}{\int_0^1 dS_w/(P_c)^2}$ (2-6)

Where λ_{rw} is the tortuosity ratio of the wetting phase, which can be calculated as follows,

$\lambda_{rw} = \frac{\tau_w(1.0)}{\tau_w(S_w)} = \frac{S_w - S_m}{1 - S_m}$ (2-7)

Where S_m is the minimum wetting-phase saturation from the capillary pressure curve, $\tau_w(1.0)$ and $\tau_w(S_w)$ are the tortuosities of the wetting phase when the wetting phase saturation is equal to 100% and S_w, respectively.

Mualem[40]: $k_{rw} = (\lambda_{rw})^n (\frac{\int_0^{S_w} dS_w/P_c}{\int_0^1 dS_w/P_c})^2$ (2-8)

Where *n* may be positive or negative.

2.2.2.2 Surface tension

In the bulk of a liquid, molecules have interactions with all neighbouring molecules. At an interface, the liquid molecule contacts with the liquid molecules in a half-space, and interacts with gas molecules in another half-space. Due to the low densities of gases, the interactions between liquid and gases are less. Therefore, a dissymmetry of interactions is formed on the interface of the liquid and gas, which results in a defect of surface energy. At the macroscopic scale, 'surface tension' was named to take this molecule effect into account, and the dimension is energy per unit surface (J/m^2 or

N/m). This means surface tension will increase with the intermolecular attraction and decrease with the interfacial surface area (molecular size).

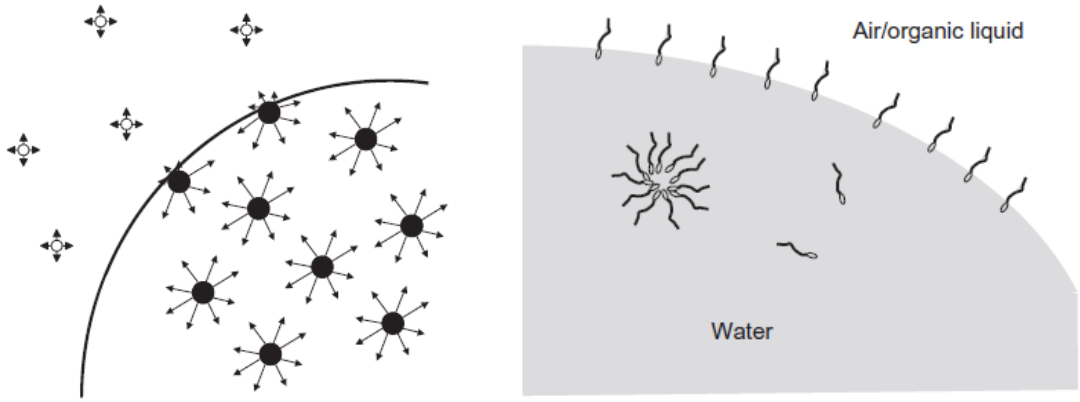

(a) (b)

Fig. 2. 8 Schematics of (a) molecules in the bulk of the liquid and near the gas-liquid interface; (b) surfactants in the liquid[41]

Adding surfactants which are long molecules with a hydrophilic head and a hydrophobic tail, into the liquid can reduce or adjust the surface tension. It is achieved through modifying the interaction forces between the particle and surface, including van der Waals force, electrostatic force and hydrophobic force[42]. At the macroscopic scale, surface tension is reduced by the migration of the surfactants to the interface which results in a reduction of the interfacial energy. The contact angle is also reduced as the deposition of surfactants on the solid surface changes the surface tension between the solid and the liquid. Surfactant applies significantly in enhanced oil recovery, which is called surfactant flooding. The addition of alkali to surfactant flooding helps to reduce the amount of surfactant required in practice, and this process is known as alkaline/surfactant/polymer flood (ASP) [43].

2.2.2.3 Wettability

Wettability is the ability of one fluid to spread on a solid surface, and it is determined by the contact angle. A liquid will spread on a substrate in a film if the energy of the system is lowered by the presence of the liquid film, i.e. total wetting. Otherwise, the liquid forms a droplet on the surface of the solid, i.e. partial wetting. In this case, the line which contacts among three phases is called the contact line or triple line. The spreading parameter *S* determines the wetting is partial or total.

$$S = \gamma_{sg} - \gamma_{sl} - \gamma_{lg} \quad (2\text{-}9)$$

Where γ_s, γ_l, and γ_{s-l} is the surface tension of solid phase, liquid phase and interface between solid and liquid phase, respectively. If *S*>0, the liquid will spread on the solid surfaces, if *S*<0, the liquid forms a droplet.

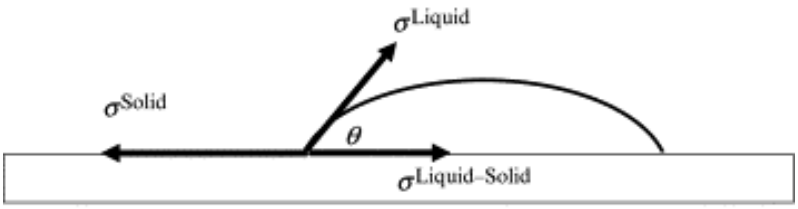

Fig. 2. 9 The balance of surface tension of liquid, solid and interfacial free energy between solid and liquid[44]

The Young's equation is commonly used to express the relationship of surface tension of three phases with the contact angle, given as equation (2-10). In the cases of partial wetting, if the contact angle is less than 90˚, the surface is hydrophilic if the liquid has a water base; when the contact angle is more than 90˚, the surface is 'hydrophobic'. However, if the liquid is oil-based, opposite wetting behaviour occurs as Fig. 2.10b

indicates. Contact angle is affected not only by the surface tension of three phases which were shown in equation (2-10), but also by physic-chemical properties of three phases (such as the chemical reaction between the liquid and solid), and surface roughness.

$$\sigma_s = \sigma_l \cdot cos\theta + \sigma_{s-l} \quad (2\text{-}10)$$

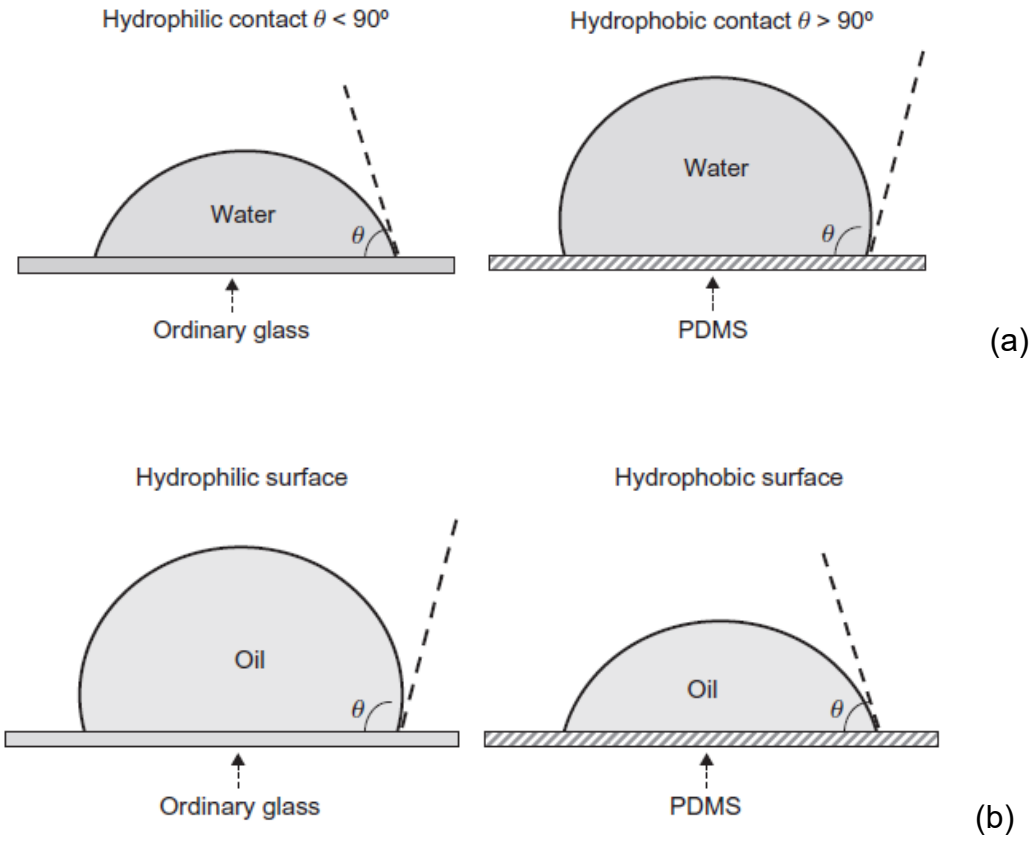

Fig. 2. 10 (a) Water and (b) silicone oil spreads on different surfaces

There are two types of contact angle: static and dynamic contact angle. Static contact angle is measured through using a microscope attached with a camera, and the recorded image can be analyzed by a software. Dynamic contact angle refers to the contact angle when the droplet is in movement. It is accomplished by adding liquids to

a static droplet on a surface, which pushes the front of the liquid to wet the uncovered surfaces, as shown in Fig. 2.11. Hoffman first proposed an expression for the dynamic contact angle based on the experimental measurements, and Voinov and Tanner[45] developed a more workable correlation based on Hoffman[46],

$$\theta_d^3 - \vartheta_s^3 = ACa \tag{2-11}$$

Where θ_d and θ_s is the dynamic and static contact angles.

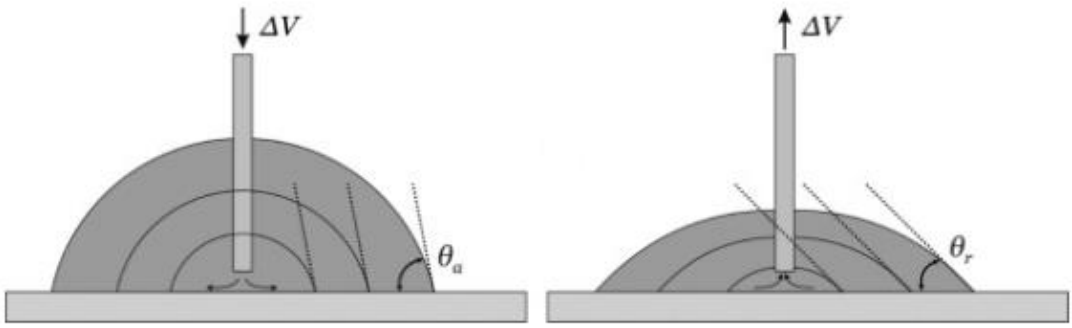

Fig. 2. 11 Measurement of advancing contact angle and receding contact angle. The advancing/receding contact angle is determined by increasing/decreasing the amount of volume in a droplet[47].

The difference of advancing contact angle and the receding contact angle for a contact line moving in an opposite direction at the same velocity is defined as the contact angle hysteresis[48]. As it is induced by the surface effects (such as surface roughness, chemical heterogeneity, surface deformation), contact angle hysteresis is often regarded as a mean of assessing the mean roughness of the surface. Experimentally, static contact angle hysteresis can be measured through three methods: tilted plate method, sessile drop method and Wilhelmy method. These methods are relatively simple as tilted plate method only requires a camera; the sessile drop method requires

a camera, a needle and a pump; and Wilhelmy method needs a motor and force measurement device. Through vibrating the droplet or the surface, the contact angle hysteresis can be reduced when a stable contact angle is required during the investigations[49].

2.2.2.4 Viscosity

The viscosity of a fluid (gas and liquid) is a measure of its resistance to deformation at a given rate. The viscosity of a Newtonian fluid has thermodynamic characteristics and it is affected by pressure and temperature of the fluid. The sensitivity of viscosity to temperature is greater than pressure[50]. Normally, it increases with temperature for gaseous systems at low densities, while decreases with the increase of temperature in liquids[51]. Simple examples of Newtonian fluids are water and blood plasma. For non-Newtonian fluids, three types are categorized based on fluid behaviour: time-independent fluids, time-dependent fluids, and viscoelastic fluids.

The Hagen-Poiseuille equation is a fluidic law to calculate the pressure drop in a long cylindrical pipe, and it applies to laminar, incompressible Newtonian fluid flows with no-slip at the solid boundary. It suggests that the resistance to fluids flow in porous media is greater when the fluid is more viscous.

2.2.3 Typical examples in natures

2.2.3.1 Oil recovery

Oil fuels the vast majority of the world's mechanized equipment, and is also the primary feedstock for many chemicals. With the significant increase of energy demand, it is not only important to regenerate old oil fields which are in the declining production, but also to find new alternative fuels. As the oil is still the main energy, enhancing oil recovery rate is one way to release the pressure of energy risks. A particular method is to use enhanced oil recovery technology after the primary and secondary oil recovery. Primary production is the process by which oil naturally flows from the underground to the surface. Secondary recovery involves the injection of water into the oil reservoir to force oil to the surface[52]. From Fig. 2.12, it is obvious that EOR is an effective method to produce the residual oil from all kinds of hydrocarbons.

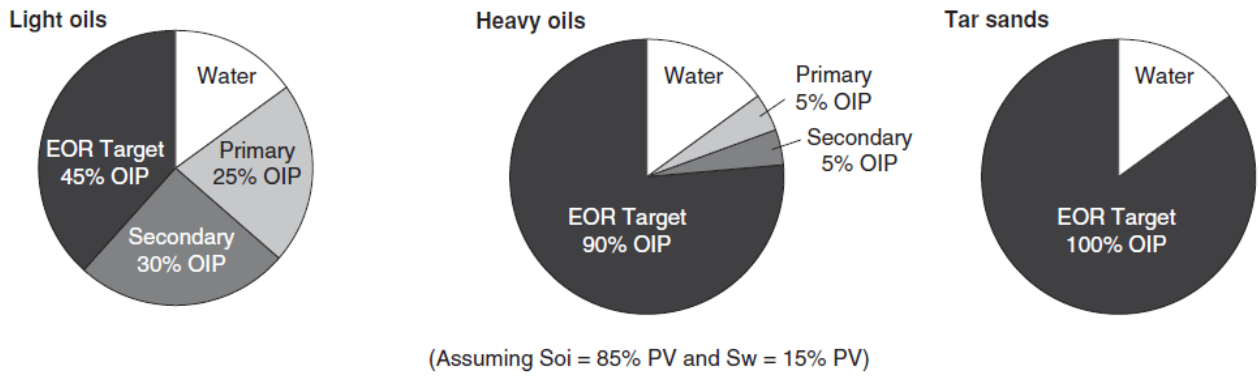

Fig. 2. 12 EOR target for different hydrocarbons[53]

Enhanced oil recovery implies to recover the oil retained in the pores due to capillary forces, and the oils which are immobile or nearly immobile due to the high viscous. EOR techniques are generally thermal methods, gas injections and chemical methods.

Depending on the different lithology, the most frequent used methods are shown in Fig. 2.13. Thermal methods are best suited for heavy oils and tar sands, and it supplies heat to vaporize some oil in the reservoirs. Oil viscosity can be reduced significantly, and thus the mobility ratio is increased[53]. Sandstone reservoirs have the highest potential to implement EOR techniques as most techniques have been tested at pilot and commercial scale. Polymer flooding is the most important chemical EOR method in sandstone reservoirs, and the injection of alkali, surfactant, alkali-polymer, surfactant-polymer and alkali-surfactant-polymer has been tested in a number of oil fields. Even though the high concentration and cost of surfactants and co-surfactants limit the polymer flooding use, it is still considered as a promising EOR process since the 1970's[1]. For light, condensate and volatile oil reservoirs, gas flooding (N_2, hydrocarbon gas, and CO_2) has been the most frequently used methods during last decades. Among these gases, CO_2 has been widely used because it is cheap and readily available from natural sources. Polymer flooding and gas flooding mainly aim at lowering the interfacial tension of oil-fluids and improving the mobility ratio in reservoirs.

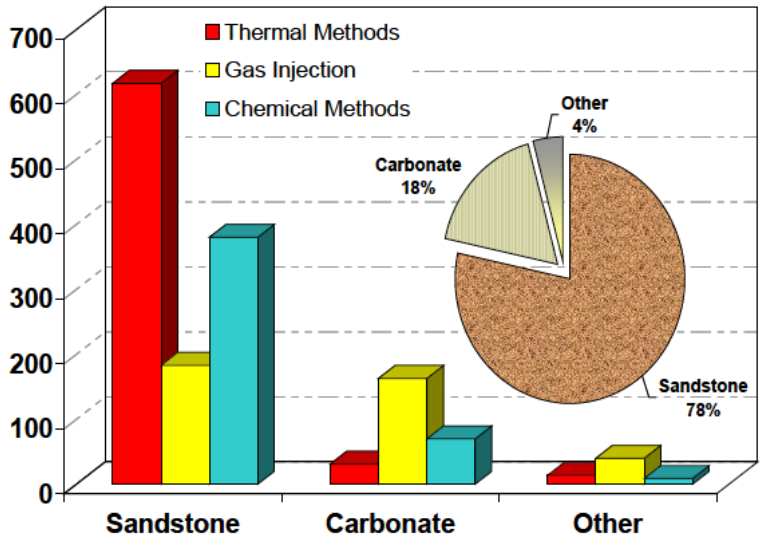

Fig. 2. 13 EOR methods based on lithology[1]

2.2.3.2 Microbubble-aided drug delivery

In cancer treatment, a large number of anticancer drugs, especially cytotoxic drugs, show efficient in targeting cell division and preventing cancer cells proliferation, while the use of cytotoxic drugs is hampered by significant side effects. Microbubbles have shown great potential to carry the active pharmaceutical chemicals as microbubbles and nanobubbles have sufficient loading capacity due to their large surface area to volume ratio[54, 55]. There are many strategies (Fig. 2.14) to carry therapeutic agents onto or into MBs depending on the properties of the drugs and MBs materials to further increase the loading capacity. MBs can protect drugs degradation and enhance the accumulation of drugs on the diseased sites, therefore it is expected to achieve high therapeutical efficiency and reduce the undesired side-effects on healthy tissues[56]. As MBs can be monitored by ultrasound, once they arrive at the diseased sites, ultrasound with sufficient intensity can be employed to rupture the MBs and then release the drugs. The strong stress and force enforced by the rupture of MBs also generate temporary holes on the cell or blood wall membrane in the close vicinity of the MBs, which can further increase the membrane permeability and drug intake efficiency significantly, as indicated in Fig. 2.15 [57, 58]. Some particulate systems are responding to X-rays, magnetic field, light, or hyperthermia, and each method has its assets and drawbacks. For example, ultrasound has good penetration, while it is difficult to target moving organs and large zones. Light can be precisely and easily tuned, however, it is invasive for the deep zone and limited to tissue penetration [59].

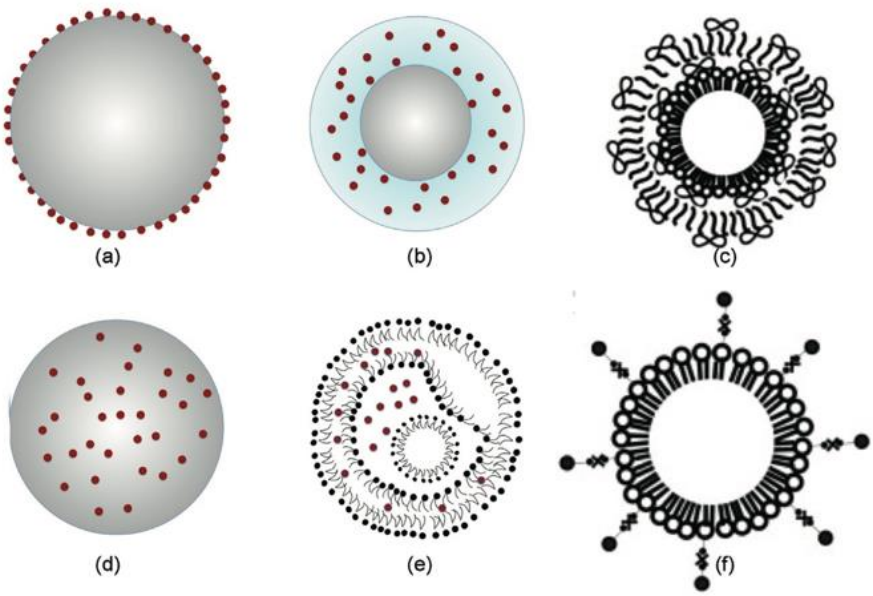

Fig. 2. 14 Schematics of methods to incorporate therapeutics into/onto MBs[60]: (a) attachment of therapeutics onto the surface of the MBs shells; (b) encapsulation of therapeutics in the shell of the MBs; (c) multilayered architecture, lipid MBs coated by one or several layers; (d) encapsulation of therapeutics inside the MBs; (e) echogenic liposomes; (f) liposomes or nanoparticles which containing drugs attached onto the surface of MBs.

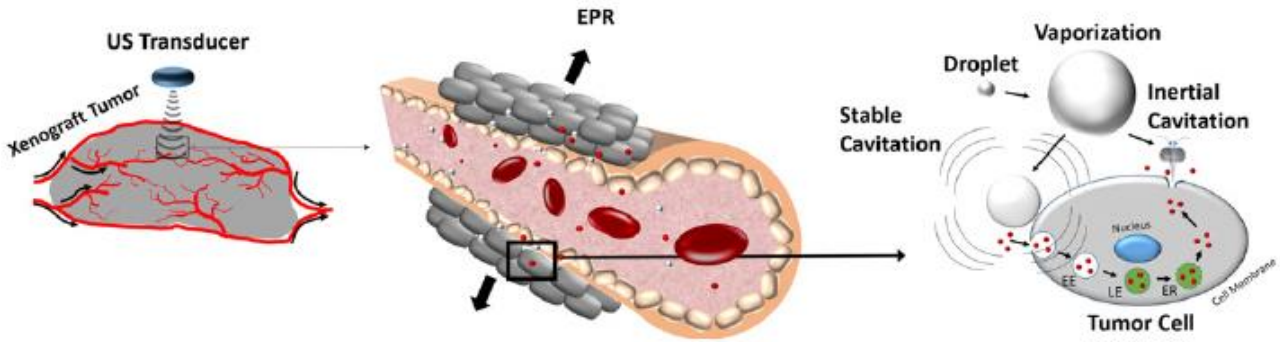

Fig. 2. 15 Schematic of the delivery of drug-loaded MBs to tumor tissues by applying ultrasound transducer; in which drugs-loaded MBs (red) are small enough to extravasate into tumor tissue via the enhanced permeability and retention effect (EPR),

inertial or stable cavitation induced by rupture of MBs promotes intracellular uptake of drugs [54].

Despite the encouraging potential obtained from many *in vitro* and *in vivo* studies, many uncertainties still hamper the clinical implementation of MBs in biological applications. A clear understanding of flow behaviours of drug-loaded MBs inside the blood vessel and mechanisms of MBs-cell interactions is essential to ensure whether the transport of drug-loaded MBs is feasible in such complex network with multiple microchannels with high interconnectivity and irregular shape. In addition, problems, such as he relatively short *in vivo* half-life of MBs, undesired premature of drug release, the appropriate ultrasound responsiveness, the safety clinically evaluation, the entrapment of MBs in some small capillaries, require fully evaluated before the drug-loaded MBs treatment can be used in clinical practice[61].

2.3 Hydraulic resistance to two-phase flows in a channel

The simplest representation of a multiphase flow in a pore is the pressure-driven flow of a gas-liquid interface through a channel. When the bubble size is comparable to the channel diameter, the walls starts to affect the bubble shape and the bubble mobility, which in turn, causes the hydraulic resistance for flow[62]. Hydraulic resistance to two-phase flows in a channel is a combination of viscous or frictional force, capillary force, buoyancy force, gravity force, and interactions among channel wall and fluids.

The magnitudes of inertial effects, gravitational forces (or buoyancy force) and viscous force to surface tension are given by the dimensionless numbers as,

$$We = \frac{\rho r u^2}{\gamma} \quad (2\text{-}12)$$

$$Bo = \frac{(\rho_w - \rho_o)\mathrm{g}l^2}{\gamma} \quad (2\text{-}13)$$

$$Ca = \frac{\mu u}{\gamma} \quad (2\text{-}14)$$

Where *We* is the Weber number, *Bo* is the Bond number and *Ca* is the Capillary number. *ρ* is the fluid density, subscripts *w, o* denoting the wetting and non-wetting phase. *r* is the radius of flow path, u is the fluid superficial velocity, γ is the surface tension. *g* is the gravitational acceleration, l is the characteristic length and μ is the fluid dynamic viscosity.

2.3.1 Frictional pressure drop

For single-phase flows, the frictional pressure loss for fluids flowing through a capillary with a constant diameter *D*, can be calculated through Darcy-Weisbach equation, given by,

$$\Delta P_f = f \frac{\Delta L \rho u^2}{2D} \quad (2\text{-}15)$$

where *L* is the length of flow path, u is the mean fluid superficial velocity and f is the Darcy friction factor.

For two-phase flows, Darcy-Weisbach equation combined with two models, the homogeneous flow (HFM) and the separated flow model (SFM), is commonly used to calculate the frictional pressure drop caused by wall friction in a horizontal capillary. The homogeneous flow model averages fluid properties based on the ratio of liquid and gas components [63], and equation (2-15) becomes,

$$\Delta P_{TP} = f_{TP} \frac{\Delta L \rho_m u^2}{2D} \quad (2\text{-}16)$$

where f_{TP} is the two-phase flow frictional factor. ρ_m is the homogenous mixture density, defined as,

$$\frac{1}{\rho_m} = \frac{x}{\rho_g} + \frac{1-x}{\rho_l} \quad (2\text{-}17)$$

where x is the mass quality, defined as $x = \frac{m_g}{m_g + m_l}$, in which m is the mass flow rate of gas (*g*) and liquid (*l*).

The separated flow model is based on the individual behaviour of each component [63]. Lockhart and Martinelli correlation [64] is commonly used in SFM to predict the frictional pressure drop for two-phase flows, $(\Delta P_f)_{TP}$, given as:

$$\left(\frac{\Delta P_f}{\Delta L}\right)_{TP} = \phi^2 \left(\frac{\Delta P_f}{\Delta L}\right)_{SP} \quad (2\text{-}18)$$

where $\left(\frac{\Delta P_f}{\Delta L}\right)_{SP}$ is the frictional pressure to single-phase flows in a capillary. ϕ^2 is the two-phase friction multiplier, widely calculated through equation (2-19).

$$\phi^2 = 1 + \frac{C}{X} + \frac{1}{X^2} \quad (2\text{-}19)$$

where Chisholm parameter *C* is a constant, ranging from nearly 0 to 21 depending on the channel diameter and mass flowrate. Some typical example of parameter *C* were shown in Table 2.1. *X* is the Lockhart-Martinelli parameter, given by

$$X^2 = \frac{(\Delta P_f / \Delta L)_l}{(\Delta P_f / \Delta L)_g} \quad (2\text{-}20)$$

$$\left(\frac{\Delta \mathrm{P}}{\Delta \mathrm{L}}\right)_l = \frac{G^2 (1-x)^2 f_l}{2D\rho_l}$$

$$\left(\frac{\Delta P}{\Delta L}\right)_g = \frac{G^2 x^2 f_g}{2D\rho_g}$$

where *G* is the total mass flux and the subscript *l, g* is the gas and liquid phase.

Table 2. 1 Value of parameter *C* in different flow regimes[65]

Liquid	**Gas**	***C value***
Turbulent	Turbulent	20
Laminar	Turbulent	12
Turbulent	Laminar	10
Laminar	Laminar	5

2.3.2 Capillary pressure for two-phase flows in a capillary

The resistance of a pore to a two-phase flow is different from that to a single phase flow due to the capillary effect induced by the two-phase interface [66]. It is important to understand the capillary pressure drop when two-phase flows in a capillary, as the presence of air bubble results in an increase in the resistance, which is the well-known 'Jamin' effect. It also occurs when oil drop-water flows in channels with varied diameters [67-69]. For example, Cobos et.al [69] found a sudden increase in the pressure drop when oil drops flow into the tapered section of a glass capillary with a diameter of 200 μm (tube) and 50 μm (throat). In low-permeability reservoirs, the 'Jamin effect' becomes severe with the progress of liquid displacement, and the resistance required to displace the oil phase from the reservoirs is significantly high

due to the great pore size variations and pore-pore throat ratios [10, 70]. The sudden increase in the resistance has been simply seen as the effect of the capillary pressure and the difference in fluids viscosity. The mechanism for this increase remains to be clarified, such as where exactly the pressure increase occurs, and what factors affect the sudden increase in the capillary resistance.

Capillary pressure, P_c across the bubble can be reasonably expressed as the function of surface tension and curvatures of the menisci based on Young–Laplace equation as reported in many literatures[71-74]. At the initial movement of the bubble, the curvature of menisci can be taken as the function of the cross-sectional area of the microchannel, the advancing and receding contact angle. It is equal to the pressure difference between non-wetting (P_n) and wetting phase (P_w) at equilibrium, given as Young-Laplace equation:

$$P_c = P_n - P_w = \frac{2\gamma}{R} \tag{2-21}$$

For the case in a cylindrical capillary with a radius r, $r = R \cdot cos\theta$ (θ is the contact angle, R is the spherical meniscus), equation (2-22) can be derived from Young-Laplace equation.

$$P_c = \frac{2\gamma cos\theta}{r} \tag{2-22}$$

Equation (22) has been used to describe the capillary pressure at both the equilibrium state and dynamic wetting processes in porous media [36, 75, 76]. However, Equation (2-22) was proposed mainly for the equilibrium state. To achieve more acceptable results for the capillary pressure calculated from Equation (2-22), in this study, the contact angle is substituted by the dynamic contact angle measured previously in glass capillaries with the diameter ranging from 100-1000 μm [77].

2.3.3 Pressure loss due to the sudden contraction of capillary

The sudden contraction in flow channel geometry will cause a small pressure drop when fluids flow in constricted tubes. In this study, we assume a sudden geometry contraction occurs at the point with a diameter D_t. For two-phase flows, the pressure drop due to the sudden contraction, $\Delta P_{contraction}$ is given by [78],

$$\Delta P_{contraction} = \frac{G^2}{2\rho_l}\left[\left(\frac{1}{C_C}-1\right)^2 + 1 - K^2\right]\left[1 + x\left(\frac{\rho_l}{\rho_g}-1\right)\right] \quad (2\text{-}23)$$

where *G* is the total mass flux of fluids. *K* is the ratio between the cross-sectional area of the contraction point (with a diameter D_t) to the area of the glass tube (with an inner diameter of 3 mm). x is the mass flow quality, ρ_l and ρ_g is the density of the liquid and gas, respectively. C_c is the contraction coefficient, which can be estimated from the function of *K*, given by [79],

$$C_C = \frac{1}{0.639(1-K)^{0.5}+1} \quad (2\text{-}24)$$

2.4 Hydraulic pressure drop for bubble dislodgment in a network

2.4.1 Bubble lodgment and dislodgment

When bubbles flow in small blood capillaries, the bubble shape may be deformed as tubular, and microbubble may be lodged/stuck with the progression of bubbles due to the pinning force in capillaries, i.e. bubble lodgment, as observed *in vitro* by Calderon

et al.[80] and *in vivo* by Samuel et al[81]. The process of removing the lodged bubbles from capillary network by increasing the liquid flowrate or driving pressure is named as bubble dislodgment. Schematic of air embolism in a capillary network is shown in Fig. 2.16. Samuel et al. observed that the perfluorocarbon bubbles with an average length of 76 ± 23 μm often lodged at the capillary bifurcation in the rats. In a bifurcation model patterned on poly (dimethyl siloxane) (PDMS), Calderon et al. found that the air bubble commonly lodged at the daughter channel of the bifurcation. They also investigated the impact of bubble size, parent to daughter channel ratio, and cross-sectional shape and area on the bubble lodgment. The two groups also observed that the driving pressure required to dislodge/remove a bubble is much higher than the pressure required for the bubble lodgment. In order to precisely control the bubble flow in a capillary network, it is worth to investigate the pressure required to dislodge the bubble from the network, and what factors affecting the bubble dislodgment in a capillary network.

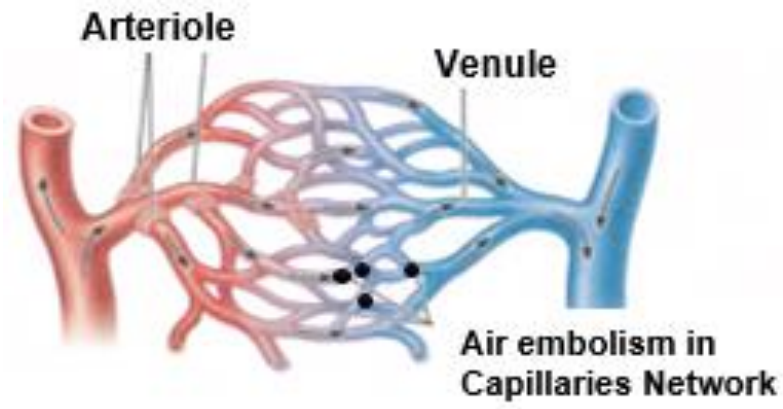

Fig. 2. 16 Schematic of air embolism in the capillary network

2.4.1.1 In single microchannels

Some work has been done to investigate the bubble dislodgment in single microchannels. Pioneering work on bubble dislodgment was conducted by Cavanagh et al., in which they experimentally examined the effect of bubble diameter, channel inclination angle and surface materials on the flow range for bubble suspension in single mini-channels[82]. They found that dislodging a bubble in the acrylic tube is more difficult than that in the glass tube, as the acrylic material has a higher spreading coefficient, causing a stronger strength of contact forces. Blackmore et al. experimentally studied the bubble adhesion and detachment between two parallel plates with a width of 11 mm and a thickness of 30-200 μm. They demonstrated that the effect of D_c/h (D_c is bubble contact diameter, and h is the channel height) on the Capillary number required to detach a bubble[83]. They found that the shearing force required to dislodge a bubble decreased with the increase of bubble contact length. They modelled the critical detachment state through equalling the drag force and adhesion force, while the viscous force was ignored due to the extremely low flow velocity. Metz et al. demonstrated that, the pinning force, as the threshold, must be overcome to initiate a bubble movement in a tapered channel [84]. In their model, the pinning force was simply assumed proportional to the length of contact line and liquid surface tension. However, this assumption makes it hard to distinguish the relative importance of surface tension, inertia, viscosity and contact angle on the bubble dislodgment. Mohammadi and Sharp also focused on the role of pinning force on the blockage of dry bubbles in a single square microchannel of around 1 mm size [85]. They suggested that the use of highly hydrophilic surface effectively reduces the bubble lodgement in single channels at low velocities.

2.4.1.2 In complex network

The network structures reported in literatures for the investigation into bubble flow behavior are mainly single straight channels[85-87], Y-type or U type channels[88-91]. A single channel cannot simulate the flow conditions of bubble lodgment in complex capillary network. For example, when an elongated bubble lodges in a single cylindrical channel, the pressure difference between the two ends of the bubble is the driving force to push the bubble, as there is no other pathway for the liquid to move forwards. However, a capillary network has many bifurcations. Fluids have several paths to flow in a highly-connected network, and it will consciously choose to travel to the channel with smaller resistance (without bubbles/with less bubbles). Based on the experimental results *in vivo*, particles and bubbles are more easily deposited in bifurcating regions[92], which means dislodging a bubble or particle would be more difficult from a network with multiple bifurcations than from a single microchannel.

Capillary network with multiple bifurcations enables to demonstrate the effect of multiple channels and bifurcations on the flow resistance and bubble dislodgment. Previous studies on bifurcation model mainly investigated the bubble splitting and to which daughter tubes the bubble would travel[88, 89, 91, 93]. A tree-like structure, which is the most complicated network reported in literature, has been intensively investigated for mixing efficiency, pressure drop, and mass and heat transfer rate in the applications of electronics cooling[94], fuel cells[95] and chemical reactors[96], [31, 97, 98]. However, most of the tree-like structures manufactured or simulated in literatures are symmetrical dichotomous, which have straight channels and junctions without smooth change. As most of the natural porous media have the irregular pore

space, various pore size and unsymmetrical geometry, the effect of network structure and geometry on the resistance to bubble flows in such network is worth to investigate.

2.4.2 Capillary pressure drop in a rectangular channel

For a rectangular microchannel, the capillary pressure drop ΔP_c could be expressed by the equation (2-25)[85, 99].

$$\Delta P_c = 2\gamma\left(\frac{1}{W_j}+\frac{1}{H_j}\right)(\cos\theta_{rec}-\cos\theta_{adv}) \quad (2\text{-}25)$$

where *W*, *H* is the channel width and height, respectively, and subscript *j* represents the corresponding microchannel.

For 'dry' bubbles (as shown in Fig. 2.17a), pinning force along the triple contact lines among the gas, liquid and channel wall also plays a role in resisting bubble motion. Pinning of the contact line is accompanied with contact angle hysteresis on a non-ideal surface, and it makes the bubble or droplet pinned even on an inclined plane[100]. In general, two different mechanisms have been proposed to explain the pinning force: manifestation of adhesion hysteresis and mechanical pinning by defects. In the adhesion mechanism, as the solid-liquid interface is not retracting its original path when it recedes, the adhesion and separation processes are not thermodynamic reversible, so energy dissipation will occur to separate the two surfaces. In the local defect mechanism, the contact line tends to be trapped when it retracts at certain position on the solid surface which is not homogeneous on a microscopic scale. When the contact line encountered the blemish, it will be pinned locally. Brien proposed a simplified model to qualitatively predict that the contact line pins, distorts and finally slides across the defect when pushing a small spherical object through a liquid-gas

interface[101]. The contribution of contact line pinning by surface heterogeneities to the stabilization of microbubbles on a substrate remains to be fully understood [102], as the properties of surface microbubbles, such as small contact angle, long lifetimes, are related to the contact pinning force of the microbubbles. It constrains microbubbles to grow or shrink only in height, and their footprints remain fixed[103].

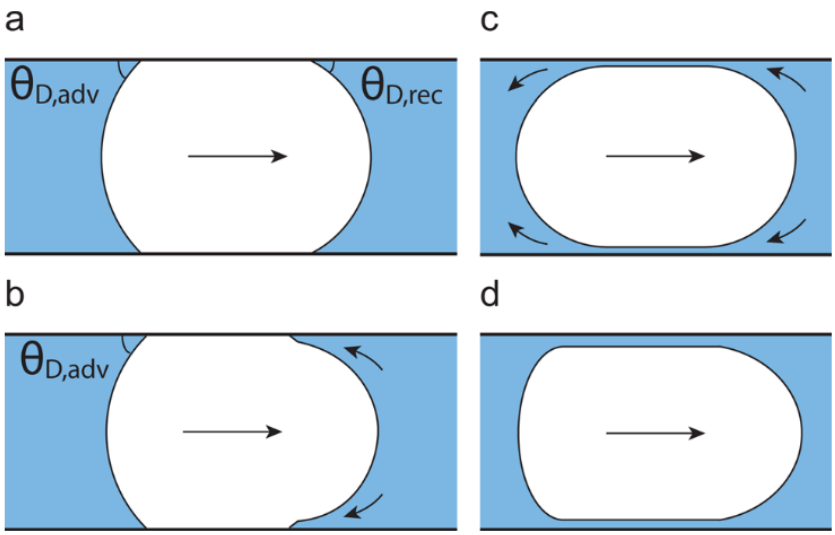

Fig. 2. 17 Schematics of (a) dry bubble; (b) partially lubricated bubble; (c) lubricated bubble with no triple contact line does not experience pinning force, and (d) bullet-shaped lubricated bubble[85].

2.4.3 Pressure losses in bifurcations

Pressure losses in a bifurcation or a junction are commonly assumed negligible in many vascular network flow modelling. This assumption stands true in large vessels or in the network with only one symmetric bifurcation [104, 105]. However, the pressure loss in bifurcations may play a significant role due to the accumulation of the pressure losses in successive bifurcations, especially when fluid flows in a complex

network. Pressure loss coefficients for T-junction has been estimated by Wood et al., and they also pointed out that a constant loss coefficient may not be adequate to represent the pressure loss phenomenon in different networks[106]. Mynard et al. [105] proposed a formulation to estimate the junction pressure losses, as shown in equation (2-26), based on the formulation described by Bassett et al.[107]. The results show that taking pressure loss in junctions into account, the modelling results are in good agreement with the high resolution computational fluid dynamics simulation results over a wide range of junction geometries and flow conditions[105].

$$\Delta P_{loss} = \frac{1}{2}\rho u_{inlet}^2(1 + \lambda_j^2\varphi_j^2 - 2\lambda_j\varphi_j cos\omega_j) \quad (2\text{-}26)$$

Where u_{inlet} is the velocity of inlet channel, and ω_j is the average lateral outflow angle between the bifurcating velocity vector and the axis of branch *j*, as shown in Fig. 2.18. λ_j is the flow ratio, defined as $\lambda_j = \frac{Q_j}{Q_{inlet}}$, and φ_j is the cross-sectional area ratio, defined as $\varphi_j = \frac{A_{inlet}}{A_j}$.

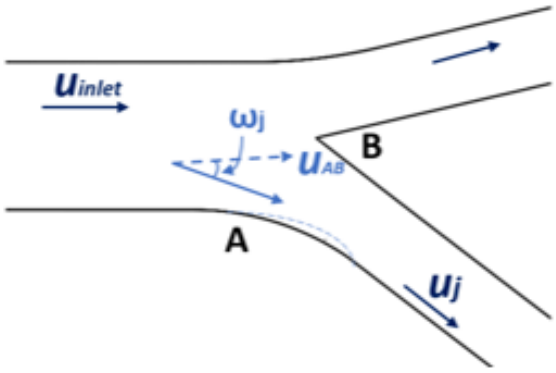

Fig. 2. 18 Schematics of the flow situation around a bifurcation, in which the vectors represent the direction of the centreline (dash line) and downstream of the bifurcation

2.4.4 Secondary flow in curved microchannels

Recently, the secondary flow inside a curved channel has received much attention as it was found in many areas from heat exchangers to human arterial systems[108-110]. In inertial microfluidics applications, the secondary flow is always introduced in laminar flow through changing the microchannel geometry, such as varying the channel curvature, and introducing obstacles (grooves, protrusion or fins) in the passage [108, 109, 111]. The secondary flow is induced by the pressure gradient which is generated due to the velocity mismatch in the centerline and the concave wall of the microchannel. In a straight channel, the velocity distribution is a parabolic profile, while in curved channels this profile will be disturbed because of the centrifugal force. Therefore, the maximal velocity position will shift from the centerline towards the concave wall of the microchannel, and this great velocity gradient will lead to a pressure gradient across the radial direction. The imbalance leads to the recirculation of the fluid and forms at least two Dean vortices with the direction from the center of the channel towards the concave wall of the channel, as shown in Fig. 2.19. The magnitude of instability or vortices is dependent on the Reynolds number or Dean number. The strength of Dean flow is characterized by the Dean number, which was firstly derived by Dean [112], given as,

$$De = Re(\frac{D}{2Rc})^{1/2} \quad (2\text{-}27)$$

Where D is the microchannel diameter, and R_c is the radius of curvature of the microchannel. In the inertial microfluidics with curved microchannels, when Re>1, the secondary flow normally needs to be taken into account [111, 113].

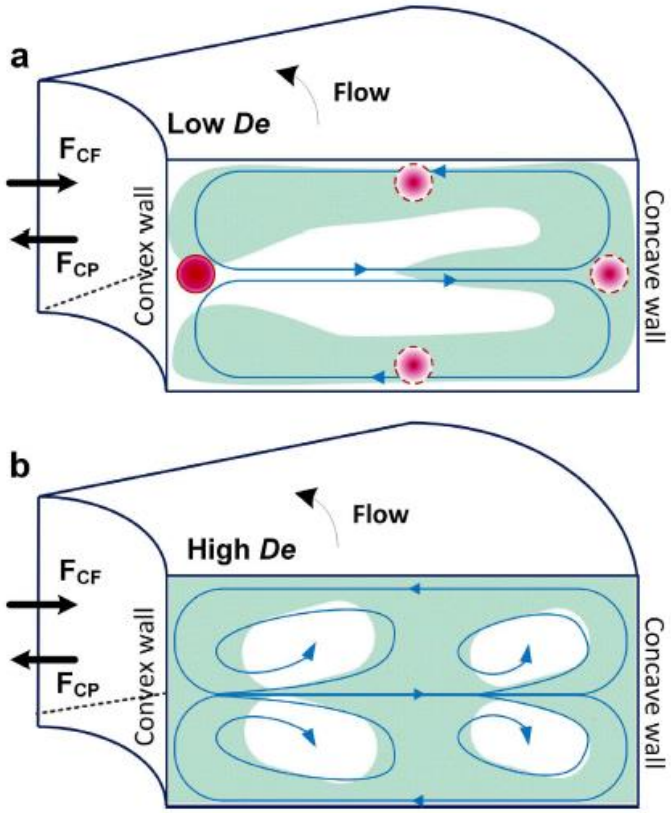

Fig. 2. 19 Schematics of two counter rotating vortices in a curved rectangular channel at (a) low *De* and (b) high *De*; F_{CF} is the centrifugal forces and F_{CP} is the centripetal forces on the parabolic velocity profile[110]

2.4.5 Electric circuit analogy

The electric circuit analogy method is based on the analogous behaviour of hydraulic electric circuits, with correlations of pressure to voltage, volumetric flowrate to current and hydraulic resistance to electric resistance [114, 115]. It helps the rapid prediction of pressure-driven laminar flow not only in microchannels, but also in complex microfluidic networks. Through using electric circuit analogy, the precise control of fluid flow in each segment of a complex network becomes feasible. In fluid mechanics, Hagen-Poiseuille equation is the base which expresses the relationship between

pressure drop and volumetric flowrate of fluids. In electric circuit, Ohm's law analogously explains the voltage drop and electric current in a resistor conductor, as shown in Fig. 2.20. The analogy is effective when the flow is laminar, viscous and incompressible, and the channel cross-section is not restricted to circular.

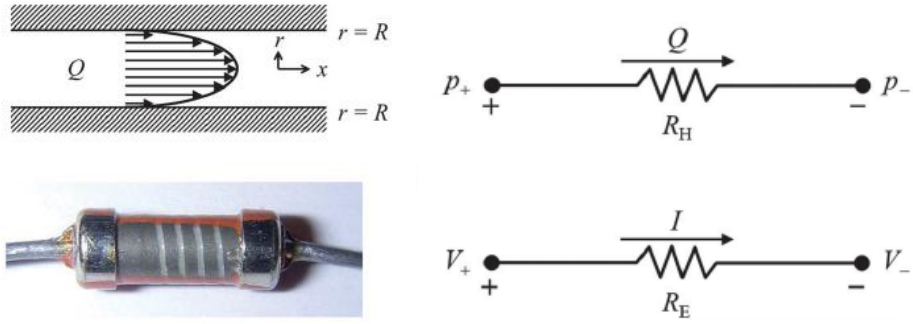

(a) (b)

Fig. 2. 20 (a) the physical similarities between the Poiseuille flow in a cylindrical channel and the flow of electricity in a resistor, (b) analogy of Hagen-Poiseuille's law and Ohm's law[115]

Hagen-Poiseuille law: $Q = \frac{\pi R^4}{8\eta}\left(-\frac{\Delta p}{dx}\right) = \frac{\pi R^4 \Delta p}{8\eta L}$ (2-28)

Simplifying equation (2-28), $\Delta p = QR_H$, $R_H = \frac{8\eta L}{\pi R^4}$ (2-29)

Where R_H is the hydraulic resistance (Pa·s·cm^{-3}), Equation (2-29) shows that the pressure drop through a channel is proportional to the volumetric flowrate and the hydraulic resistance; the value of R_H is normally constant for a fixed fluidic and geometric condition, and it is proportional to the channel length (L).

2.5 Reference

1. Alvarado, V. and E. Manrique, *Enhanced Oil Recovery: An Update Review.* Energies, 2010. **3**(9): p. 1529-1575.10.3390/en3091529
2. Pollet, B., et al., *Proton exchange membrane fuel cells*, in *Compendium of Hydrogen Energy*. 2016, Elsevier. p. 3-56.
3. Darcy, H.P.G., *Les Fontaines publiques de la ville de Dijon. Exposition et application des principes à suivre et des formules à employer dans les questions de distribution d'eau, etc*. 1856: V. Dalamont.
4. Hammersley, J.R. and D.E. Olson, *Physical models of the smaller pulmonary airways.* J Appl Physiol (1985), 1992. **72**(6): p. 2402-14.10.1152/jappl.1992.72.6.2402
5. Nguyen, G.D., A. El-Zein, and T. Bennett, *A conceptual approach to two-scale constitutive modelling for hydro-mechanical coupling.* arXiv preprint arXiv:1406.1052, 2014,
6. Indayaningsih, N., et al., *Preparation of carbon composite from coconut fiber for gas diffusion layer.* Ionics, 2016. **22**(8): p. 1445-1449.10.1007/s11581-016-1657-6
7. Blunt, M.J., *Flow in porous media - pore-network models and multiphase flow.* Current Opinion in Colloid & Interface Science, 2001. **6**(3): p. 197-207.Doi 10.1016/S1359-0294(01)00084-X
8. Blunt, M.J. and H. Scher, *Pore-level modeling of wetting.* Physical Review E, 1995. **52**(6): p. 6387-6403.10.1103/PhysRevE.52.6387

9. Lala, A.M.S. and N.A.A. El-Sayed, *Effect of pore framework and radius of pore throats on permeability estimation.* Journal of African Earth Sciences, 2015. **110**: p. 64-74.10.1016/j.jafrearsci.2015.05.019

10. Nelson, P.H., *Pore-throat sizes in sandstones, tight sandstones, and shales.* Aapg Bulletin, 2009. **93**(3): p. 329-340.10.1306/10240808059

11. Rezaee, R., A. Saeedi, and B. Clennell, *Tight gas sands permeability estimation from mercury injection capillary pressure and nuclear magnetic resonance data.* Journal of Petroleum Science and Engineering, 2012. **88-89**: p. 92-99.10.1016/j.petrol.2011.12.014

12. Joekar-Niasar, V. and S.M. Hassanizadeh, *Analysis of Fundamentals of Two-Phase Flow in Porous Media Using Dynamic Pore-Network Models: A Review.* Critical Reviews in Environmental Science and Technology, 2012. **42**(18): p. 1895-1976.10.1080/10643389.2011.574101

13. Warnier, M.J.F., et al., *Pressure drop of gas–liquid Taylor flow in round micro-capillaries for low to intermediate Reynolds numbers.* Microfluidics and Nanofluidics, 2009. **8**(1): p. 33-45.10.1007/s10404-009-0448-z

14. Kreutzer, M.T., et al., *Inertial and interfacial effects on pressure drop of Taylor flow in capillaries.* Aiche Journal, 2005. **51**(9): p. 2428-2440.10.1002/aic.10495

15. Bretherton, F.P., *The Motion of Long Bubbles in Tubes.* Journal of Fluid Mechanics, 1961. **10**(2): p. 166-188.Doi 10.1017/S0022112061000160

16. Vrij, A. and J.T. Overbeek, *Rupture of Thin Liquid Films Due to Spontaneous Fluctuations in Thickness.* Journal of the American Chemical Society, 1968. **90**(12): p. 3074-+.Doi 10.1021/Ja01014a015

17. Khodaparast, S., et al., *Dewetting of Thin Liquid Films Surrounding Air Bubbles in Microchannels.* Langmuir, 2018. **34**(4): p. 1363-1370.10.1021/acs.langmuir.7b03839

18. Haller, D., P. Woias, and N. Kockmann, *Simulation and experimental investigation of pressure loss and heat transfer in microchannel networks containing bends and T-junctions.* International Journal of Heat and Mass Transfer, 2009. **52**(11-12): p. 2678-2689.10.1016/j.ijheatmasstransfer.2008.09.042

19. Liu, Y., R.M. So, and C.H. Zhang, *Modeling the bifurcating flow in an asymmetric human lung airway.* J Biomech, 2003. **36**(7): p. 951-9.10.1016/s0021-9290(03)00064-2

20. Liu, H. and P.W. Li, *Even distribution/dividing of single-phase fluids by symmetric bifurcation of flow channels.* International Journal of Heat and Fluid Flow, 2013. **40**: p. 165-179.10.1016/j.ijheatfluidflow.2013.01.011

21. Wang, X.Q., A.S. Mujumdar, and C. Yap, *Effect of bifurcation angle in tree-shaped microchannel networks.* Journal of Applied Physics, 2007. **102**(7): p. 073530.Artn 07353010.1063/1.2794379

22. Varner, V.D. and C.M. Nelson. *Computational models of airway branching morphogenesis*. in *Seminars in cell & developmental biology*. 2017. Elsevier.

23. Wechsatol, W., S. Lorente, and A. Bejan, *Tree-shaped insulated designs for the uniform distribution of hot water over an area.* International Journal of Heat and Mass Transfer, 2001. **44**(16): p. 3111-3123.Doi 10.1016/S0017-9310(00)00338-0

24. Wang, X.Q., A.S. Mujumdar, and C. Yap, *Thermal characteristics of tree-shaped microchannel nets for cooling of a rectangular heat sink.* International Journal

of Thermal Sciences, 2006. **45**(11): p. 1103-1112.10.1016/j.ijthermalsci.2006.01.010

25. Brown, L., et al., *Fabrication and characterization of poly(methylmethacrylate) microfluidic devices bonded using surface modifications and solvents.* Lab on a Chip, 2006. **6**(1): p. 66-73.10.1039/b512179e
26. Cygan, Z.T., et al., *Microfluidic platform for the generation of organic-phase microreactors.* Langmuir, 2005. **21**(8): p. 3629-34.10.1021/la0471137
27. Metzker, M.L., *Emerging technologies in DNA sequencing.* Genome Res, 2005. **15**(12): p. 1767-76.10.1101/gr.3770505
28. Sudarsan, A.P. and V.M. Ugaz, *Fluid mixing in planar spiral microchannels.* Lab Chip, 2006. **6**(1): p. 74-82.10.1039/b511524h
29. Lorente, S., W. Wechsatol, and A. Bejan, *Tree-shaped flow structures designed by minimizing path lengths.* Int. J. Heat Mass Tran., 2002. **45**(16): p. 3299-3312.Pii S0017-9310(02)00051-0 Doi 10.1016/S0017-9310(02)00051-0
30. Murray, C.D., *The Physiological Principle of Minimum Work: I. The Vascular System and the Cost of Blood Volume.* Proc Natl Acad Sci U S A, 1926. **12**(3): p. 207-14.10.1073/pnas.12.3.207
31. Gosselin, L., *Optimization of tree-shaped fluid networks with size limitations.* International Journal of Thermal Sciences, 2007. **46**(5): p. 434-443.10.1016/j.ijthermalsci.2006.06.006
32. Roberts, B.W. and W.L. Olbricht, *The distribution of freely suspended particles at microfluidic bifurcations.* Aiche Journal, 2006. **52**(1): p. 199-206.10.1002/aic.10613

33. Holland, F.A. and R. Bragg, *7 - Gas–liquid two-phase flow*, in *Fluid Flow for Chemical Engineers (Second Edition)*, F.A. Holland and R. Bragg, Editors. 1995, Butterworth-Heinemann: Oxford. p. 219-267.

34. Parlett, C.M., et al., *Spatially orthogonal chemical functionalization of a hierarchical pore network for catalytic cascade reactions.* Nat Mater, 2016. **15**(2): p. 178-82.10.1038/nmat4478

35. Rezaee, M.R., A. Jafari, and E. Kazemzadeh, *Relationships between permeability, porosity and pore throat size in carbonate rocks using regression analysis and neural networks.* Journal of Geophysics and Engineering, 2006. **3**(4): p. 370-376.10.1088/1742-2132/3/4/008

36. Reeves, P.C. and M.A. Celia, *A functional relationship between capillary pressure, saturation, and interfacial area as revealed by a pore-scale network model.* Water Resources Research, 1996. **32**(8): p. 2345-2358.Doi 10.1029/96wr01105

37. Coates, G. and S. Denoo, *The producibility answer product.* The Technical Review, 1981. **29**(2): p. 55-63,

38. Purcell, W.R., *Capillary Pressures - Their Measurement Using Mercury and the Calculation of Permeability Therefrom.* Transactions of the American Institute of Mining and Metallurgical Engineers, 1949. **186**(2): p. 39-48, <Go to ISI>://WOS:A1949UP95300004

39. Burdine, N.T., *Relative Permeability Calculations from Pore Size Distribution Data.* Transactions of the American Institute of Mining and Metallurgical Engineers, 1953. **198**(3): p. 71-78, <Go to ISI>://WOS:A1953XR34700008

40. Mualem, Y., *A new model for predicting the hydraulic conductivity of unsaturated porous media.* Water resources research, 1976. **12**(3): p. 513-522,

41. Berthier, J., *Micro-drops and digital microfluidics*. 2012: William Andrew.

42. Free, M.L., *Chapter 13 - The Use of Surfactants to Enhance Particle Removal from Surfaces*, in *Developments in Surface Contamination and Cleaning (Second Edition)*, R. Kohli and K.L. Mittal, Editors. 2016, William Andrew Publishing: Oxford. p. 595-626.

43. Hirasaki, G.J., C.A. Miller, and M. Puerto, *Recent Advances in Surfactant EOR.* Spe Journal, 2011. **16**(4): p. 889-907.Doi 10.2118/115386-Pa

44. Tanaka, T., J. Lee, and P.R. Scheller, *Chapter 1.5 - Interfacial Free Energy and Wettability*, in *Treatise on Process Metallurgy*, S. Seetharaman, Editor. 2014, Elsevier: Boston. p. 61-77.

45. Fermigier, M. and P. Jenffer, *An Experimental Investigation of the Dynamic Contact-Angle in Liquid Liquid-Systems.* Journal of Colloid and Interface Science, 1991. **146**(1): p. 226-241.Doi 10.1016/0021-9797(91)90020-9

46. Hoffman, R.L., *A study of the advancing interface. I. Interface shape in liquid—gas systems.* Journal of colloid and interface science, 1975. **50**(2): p. 228-241,

47. Rapp, B.E., *Chapter 20 - Surface Tension*, in *Microfluidics: Modelling, Mechanics and Mathematics*, B.E. Rapp, Editor. 2017, Elsevier: Oxford. p. 421-444.

48. Eral, H.B., D.J.C.M. 't Mannetje, and J.M. Oh, *Contact angle hysteresis: a review of fundamentals and applications.* Colloid and Polymer Science, 2013. **291**(2): p. 247-260.10.1007/s00396-012-2796-6

49. Rodriguez-Valverde, M.A., F.J.M. Ruiz-Cabello, and M.A. Cabrerizo-Vilchez, *A new method for evaluating the most-stable contact angle using mechanical vibration.* Soft Matter, 2011. **7**(1): p. 53-56.10.1039/c0sm00939c

50. White, F.M., *Fluid mechanics*. 2003, McGraw-Hill, New York.

51. Demirel, Y., *Chapter 2 - Transport and Rate Processes*, in *Nonequilibrium Thermodynamics (Third Edition)*, Y. Demirel, Editor. 2014, Elsevier: Amsterdam. p. 75-118.

52. Hirsch, R.L., R. Bezdek, and R. Wendling, *CHAPTER 2 - Peaking of World Oil Production and Its Mitigation*, in *Driving Climate Change*, D. Sperling and J.S. Cannon, Editors. 2007, Academic Press: Burlington. p. 9-27.

53. Thomas, S., *Enhanced oil recovery - An overview.* Oil & Gas Science and Technology-Revue D Ifp Energies Nouvelles, 2008. **63**(1): p. 9-19.10.2516/ogst:2007060

54. Sirsi, S. and M. Borden, *Microbubble Compositions, Properties and Biomedical Applications.* Bubble Sci Eng Technol, 2009. **1**(1-2): p. 3-17.10.1179/175889709X446507

55. Sirsi, S.R. and M.A. Borden, *State-of-the-art materials for ultrasound-triggered drug delivery.* Adv Drug Deliv Rev, 2014. **72**: p. 3-14.10.1016/j.addr.2013.12.010

56. Boissenot, T., et al., *Ultrasound-triggered drug delivery for cancer treatment using drug delivery systems: From theoretical considerations to practical applications.* J Control Release, 2016. **241**: p. 144-163.10.1016/j.jconrel.2016.09.026

57. van Wamel, A., et al., *Vibrating microbubbles poking individual cells: drug transfer into cells via sonoporation.* J Control Release, 2006. **112**(2): p. 149-55.10.1016/j.jconrel.2006.02.007

58. Hu, Y., J.M. Wan, and A.C. Yu, *Membrane perforation and recovery dynamics in microbubble-mediated sonoporation.* Ultrasound Med Biol, 2013. **39**(12): p. 2393-405.10.1016/j.ultrasmedbio.2013.08.003

59. Janib, S.M., A.S. Moses, and J.A. MacKay, *Imaging and drug delivery using theranostic nanoparticles.* Advanced Drug Delivery Reviews, 2010. **62**(11): p. 1052-1063.10.1016/j.addr.2010.08.004

60. Huang, S.-L. and D.D. McPherson, *Ultrasound for Drug/Gene Delivery.* 2014: p. 269-283.10.1016/b978-0-12-407722-5.00016-5

61. Lentacker, I., S.C. De Smedt, and N.N. Sanders, *Drug loaded microbubble design for ultrasound triggered delivery.* Soft Matter, 2009. **5**(11): p. 2161.10.1039/b823051j

62. Olbricht, W.L., *Pore-scale prototypes of multiphase flow in porous media.* Annual Review of Fluid Mechanics, 1996. **28**(1): p. 187-213.DOI 10.1146/annurev.fl.28.010196.001155

63. Harirchian, T., *Two-phase flow and heat transfer in microchannels*. 2010: Purdue University.

64. Lockhart, R.W. and R.C. Martinelli, *Proposed correlation of data for isothermal two-phase, two-component flow in pipes.* Chem. Eng. Prog, 1949. **45**(1): p. 39-48,

65. Barreto, E.X., J.L.G. Oliveira, and J.C. Passos, *Frictional pressure drop and void fraction analysis in air-water two-phase flow in a microchannel.* International Journal of Multiphase Flow, 2015. **72**: p. 1-10.10.1016/j.ijmultiphaseflow.2015.01.008

66. Chao, C., et al., *Significance of gas-liquid interfaces for two-phase flows in micro-channels.* Chemical Engineering Science, 2018. **192**: p. 114-125.10.1016/j.ces.2018.07.026

67. Rossen, W.R. and P.A. Gauglitz, *Percolation Theory of Creation and Mobilization of Foams in Porous-Media.* Aiche Journal, 1990. **36**(8): p. 1176-1188.DOI 10.1002/aic.690360807

68. Roca, J.F. and M.S. Carvalho, *Flow of a drop through a constricted microcapillary.* Computers & Fluids, 2013. **87**(Supplement C): p. 50-56.10.1016/j.compfluid.2012.11.020

69. Cobos, S., M.S. Carvalho, and V. Alvarado, *Flow of oil-water emulsions through a constricted capillary.* International Journal of Multiphase Flow, 2009. **35**(6): p. 507-515.10.1016/j.ijmultiphaseflow.2009.02.018

70. Mcauliffe, C.D., *Oil-in-Water Emulsions and Their Flow Properties in Porous Media.* Journal of Petroleum Technology, 1973. **25**(Jun): p. 727-733.Doi 10.2118/4369-Pa

71. Dussan, E.B. and R.T.P. Chow, *On the Ability of Drops or Bubbles to Stick to Non-Horizontal Surfaces of Solids.* Journal of Fluid Mechanics, 1983. **137**(Dec): p. 1-29.Doi 10.1017/S002211208300227x

72. Younes, A., I. Hassan, and L. Kadem, *Investigation of Bubble Frequency for Slug Flow Regime in a Uniformly Heated Horizontal Microchannel.* Journal of Heat Transfer-Transactions of the Asme, 2017. **139**(6): p. 061501.Artn 06150110.1115/1.4035562

73. Paust, N., et al., *Capillary-driven pumping for passive degassing and fuel supply in direct methanol fuel cells.* Microfluidics and Nanofluidics, 2009. **7**(4): p. 531-543.10.1007/s10404-009-0414-9

74. Gaakeer, W.A., et al., *Liquid-liquid slug flow separation in a slit shaped micro device.* Chemical Engineering Journal, 2012. **207**: p. 440-444.10.1016/j.cej.2012.06.148

75. Washburn, E.W., *The dynamics of capillary flow.* Physical Review, 1921. **17**(3): p. 273-283.Doi 10.1103/Physrev.17.273

76. Dullien, F.A.L., in *Porous Media Fluid transport and pore structure* 1992, Academic Press: San Diego.

77. Li, X.X., et al., *An experimental study on dynamic pore wettability.* Chemical Engineering Science, 2013. **104**: p. 988-997.10.1016/j.ces.2013.10.026

78. Hewitt, G.F., G.L. Shires, and T.R. Bott, *Process heat transfer*. 1993, Boca Raton, Fla.: CRC [etc].

79. Friedel, L., *Two-phase Flow in Pipelines and Heat Exchangers* Chemie Ingenieur Technik, 1984. **56**(1): p. 17-17.10.1002/cite.330560105

80. Calderón, A.J., et al., *Microfluidic model of bubble lodging in microvessel bifurcations.* Applied Physics Letters, 2006. **89**(24): p. 244103,

81. Samuel, S., et al., *In vivo microscopy of targeted vessel occlusion employing acoustic droplet vaporization.* Microcirculation, 2012. **19**(6): p. 501-9.10.1111/j.1549-8719.2012.00176.x

82. Cavanagh, D.P. and D.M. Eckmann, *Interfacial dynamics of stationary gas bubbles in flows in inclined tubes.* Journal of Fluid Mechanics, 1999. **398**: p. 225-244.Doi 10.1017/S0022112099006230

83. Blackmore, B., D.Q. Li, and J. Gao, *Detachment of bubbles in slit microchannels by shearing flow.* Journal of Colloid and Interface Science, 2001. **241**(2): p. 514-520.10.1006/jcis.2001.7755

84. Metz, T., et al., *Capillary driven movement of gas bubbles in tapered structures.* Microfluidics and Nanofluidics, 2010. **9**(2-3): p. 341-355.10.1007/s10404-009-0551-1

85. Mohammadi, M. and K.V. Sharp, *The Role of Contact Line (Pinning) Forces on Bubble Blockage in Microchannels.* J Fluids Eng, 2015. **137**(3): p. 0312081-312087.10.1115/1.4029033

86. Suzuki, A. and D.M. Eckmann, *Embolism bubble adhesion force in excised perfused microvessels.* Anesthesiology, 2003. **99**(2): p. 400-8, http://www.ncbi.nlm.nih.gov/pubmed/12883413

87. Steinbrenner, J.E., et al., *Impact of channel geometry on two-phase flow in fuel cell microchannels.* Journal of Power Sources, 2011. **196**(11): p. 5012-5020.10.1016/j.jpowsour.2011.02.032

88. Calderon, A.J., et al., *A boundary element model of the transport of a semi-infinite bubble through a microvessel bifurcation.* Phys. Fluids 2010. **22**(6): p. 61902.10.1063/1.3442829

89. Calderón, A.J., J.B. Fowlkes, and J.L. Bull, *Bubble splitting in bifurcating tubes: a model study of cardiovascular gas emboli transport.* J. Appl. Physiol., 2005. **99**(2): p. 479-487,

90. Carlson, A., M. Do-Quang, and G. Amberg, *Droplet dynamics in a bifurcating channel.* International Journal of Multiphase Flow, 2010. **36**(5): p. 397-405.10.1016/j.ijmultiphaseflow.2010.01.002

91. Valassis, D.T., et al., *Microbubble transport through a bifurcating vessel network with pulsatile flow.* Biomed Microdevices, 2012. **14**(1): p. 131-43.10.1007/s10544-011-9591-x

92. Kim, C.S., et al., *Particle Deposition in Bifurcating Airway Models with Varying Airway Geometry.* Journal of Aerosol Science, 1994. **25**(3): p. 567-581.Doi 10.1016/0021-8502(94)90072-8

93. Eshpuniyani, B., J.B. Fowlkes, and J.L. Bull, *A bench top experimental model of bubble transport in multiple arteriole bifurcations.* International Journal of Heat and Fluid Flow, 2005. **26**(6): p. 865-872.10.1016/j.ijheatfluidflow.2005.10.002

94. Escher, W., B. Michel, and D. Poulikakos, *Efficiency of optimized bifurcating tree-like and parallel microchannel networks in the cooling of electronics.* International Journal of Heat and Mass Transfer, 2009. **52**(5-6): p. 1421-1430.10.1016/j.ijheatmasstransfer.2008.07.048

95. Senn, S.M. and D. Poulikakos, *Tree network channels as fluid distributors constructing double-staircase polymer electrolyte fuel cells.* Journal of Applied Physics, 2004. **96**(1): p. 842-852.10.1063/1.1757028

96. Chen, Y.P., et al., *Methanol steam reforming in microreactor with constructal tree-shaped network.* Journal of Power Sources, 2011. **196**(15): p. 6366-6373.10.1016/j.jpowsour.2011.03.044

97. Bello-Ochende, T., L. Liebenberg, and J.P. Meyer, *Constructal cooling channels for micro-channel heat sinks.* International Journal of Heat and Mass Transfer, 2007. **50**(21-22): p. 4141-4150.10.1016/j.ijheatmasstransfer.2007.02.019

98. Da Silva, A.K. and A. Bejan, *Constructal multi-scale structure for maximal heat transfer density in natural convection.* International Journal of Heat and Fluid Flow, 2005. **26**(1): p. 34-44,

99. Wong, C.W., et al., *Transient capillary blocking in the flow field of a micro-DMFC and its effect on cell performance.* Journal of the Electrochemical Society, 2005. **152**(8): p. A1600-A1605.10.1149/1.1949067

100. Hong, S.J., et al., *Anomalous contact angle hysteresis of a captive bubble: advancing contact line pinning.* Langmuir, 2011. **27**(11): p. 6890-6.10.1021/la2009418

101. O'brien, S.B.G., *The meniscus near a small sphere and its relationship to line pinning of contact lines.* Journal of colloid and interface science, 1996. **183**(1): p. 51-56,

102. Liu, Y.W., et al., *Contact line pinning and the relationship between nanobubbles and substrates.* Journal of Chemical Physics, 2014. **140**(5): p. 054705.Artn 05470510.1063/1.4863448

103. Tan, B.H., H. An, and C.D. Ohl, *Resolving the Pinning Force of Nanobubbles with Optical Microscopy.* Phys Rev Lett, 2017. **118**(5): p. 054501.10.1103/PhysRevLett.118.054501

104. Chnafa, C., et al., *Improved reduced-order modelling of cerebrovascular flow distribution by accounting for arterial bifurcation pressure drops.* J Biomech, 2017. **51**: p. 83-88.10.1016/j.jbiomech.2016.12.004

105. Mynard, J.P. and K. Valen-Sendstad, *A unified method for estimating pressure losses at vascular junctions.* Int J Numer Method Biomed Eng, 2015. **31**(7): p. e02717.10.1002/cnm.2717

106. Wood, D.J., L.S. Reddy, and J.E. Funk, *Modeling Pipe Networks Dominated by Junctions.* Journal of Hydraulic Engineering-Asce, 1993. **119**(8): p. 949-958.Doi 10.1061/(Asce)0733-9429(1993)119:8(949)

107. Bassett, M.D., et al., *A multi-pipe junction model for one-dimensional gas-dynamic simulations.* SAE transactions, 2003: p. 565-583,

108. Ahn, Y.C., W. Jung, and Z. Chen, *Optical sectioning for microfluidics: secondary flow and mixing in a meandering microchannel.* Lab Chip, 2008. **8**(1): p. 125-33.10.1039/b713626a

109. Kuppusamy, N.R., et al., *Numerical study of thermal enhancement in micro channel heat sink with secondary flow.* International Journal of Heat and Mass Transfer, 2014. **78**: p. 216-223.10.1016/j.ijheatmasstransfer.2014.06.072

110. Nivedita, N., P. Ligrani, and I. Papautsky, *Dean Flow Dynamics in Low-Aspect Ratio Spiral Microchannels.* Sci Rep, 2017. **7**: p. 44072.10.1038/srep44072

111. Zhang, J., et al., *Fundamentals and applications of inertial microfluidics: a review.* Lab Chip, 2016. **16**(1): p. 10-34.10.1039/c5lc01159k

112. Dean, W.R., *XVI. Note on the motion of fluid in a curved pipe.* The London, Edinburgh, and Dublin Philosophical Magazine and Journal of Science, 1927. **4**(20): p. 208-223,

113. Di Carlo, D., *Inertial microfluidics.* Lab Chip, 2009. **9**(21): p. 3038-46.10.1039/b912547g

114. Chen, Q., R.H. Fu, and Y.C. Xu, *Electrical circuit analogy for heat transfer analysis and optimization in heat exchanger networks.* Applied Energy, 2015. **139**: p. 81-92.10.1016/j.apenergy.2014.11.021

115. Oh, K.W., et al., *Design of pressure-driven microfluidic networks using electric circuit analogy.* Lab Chip, 2012. **12**(3): p. 515-45.10.1039/c2lc20799k

Chapter 3: Materials and Methods

3.1 Experimental methodologies

3.1.1 Measurement of pressure drop for two-phase flows in single constricted microchannels

Pressure drop characterizes the resistance for two-phase flows in microchannels and the experimental setup for measuring the resistant pressure across the inlet and the outlet of the capillaries is shown in Fig. 3.1a. The setup contains a liquid delivery pump (LC-20 AD, Shimadzu), a digital pressure transducer (DPI 280, Druck) with the resolution of 0.01 mbar to measure pressure drop, and a long working distance microscope (Brunel Microscope Ltd, 10x objective) fitted with a digital camera (AM7023 Dino-Eye, Dino-Lite Digital Micro- scope) to record the interface motion in tapered capillaries. The elapsed time and the pressure drop were recorded with a time interval of approximate 0.25 s and displayed on the computer through a LabView software.

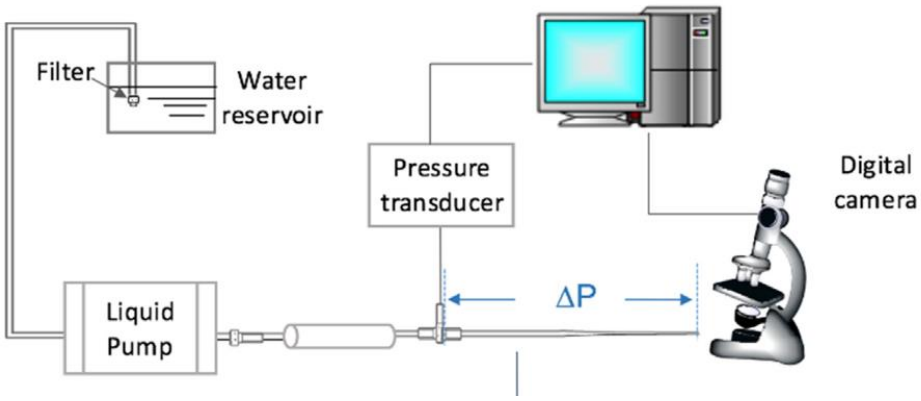

(a)

(b)

Fig. 3. 1 Illustration of (a) the experimental setup and (b) an interface in a constricted section of a capillary, in which the red point was labelled outside of the capillary wall to clearly demonstrate the position of the interface

To measure the pressure drop for two-phase flows, the gas with a fixed volume (0.05 ± 0.005 ml) was injected through a clean and sterile syringe into a constricted capillary initially filled with deionized (DI) water, to create a gas-liquid interface, as shown in Fig. 3. 1b. Then the valve was closed, and the liquid pump was operated. The pressure transducer recorded the pressure drop (ΔP) through the Labview once the pump starts. A filter in the water reservoir was used to ensure that no solid contaminants would block the fluid flow line. The constricted section of capillary was marked at different intervals as

reference points to read the interface position with the progress of experiment. The movement of an interface and the diameter of the marked point at which an interface flows through were imaged (as shown in Fig. 3. 1b) by the microscope and digital camera. Since the accuracy of measured flow path diameter depends on the measurement method and image quality, a LED light was located under the capillary to light the inner boundary line of glass capillary and to reduce the image distortion. The entire experimental process was conducted on a vibration-free horizontal workstation to minimize the external effects on measurement. All experiments were performed at room temperature and atmospheric pressure. Sufficient time was allowed to collect data to ensure equilibrium state would be achieved.

3.1.2 Measurement of bubble dislodging pressure in complex capillary networks

The dislodging pressure (ΔP) of a bubble is defined as the pressure difference between the inlet and outlet of the network that just initiates the movement of a bubble lodged in the microfluidic network. It is measured through the experimental setup, as shown in Fig 3.1a. The measurement procedure was as follows, 1) One bubble was injected into the microfluidic network which was placed horizontally and initially filled with DI water, and the liquid pump was operated with a flowrate of 0.1 ml/min. 2) The bubble was driven by a constant

pressure applied between the entrance of the network and its outlet. As the initial pressure applied was very low, it only maintained the bubble to move into one of the bifurcation branch. The bubble would then be lodged in somewhere of the branch. 3) Through slowly increasing the driving pressure, the bubble would be initiated to move once the driving pressure was adequate to overcome the overall resistance. This driving pressure is the bubble dislodging pressure, which was recorded by the pressure transducer and Labview.

During the experiments, the bubble dislodging pressure profiles in different microfluidic networks (Network A and B, as shown in Fig 3. 3) were recorded and one single bubble was injected into the network to eliminate the influence of other bubbles on the accuracy of measured pressure. More than 50 individual measurements were conducted for each microchannel to eliminate the effect of some noise or operation fluctuations on the measurement. The measurement error of the bubble dislodging pressure is below 10%.

3.1.3 Estimation of pressure drop in a microchannel *j* in a complex capillary network through electric circuit analogy

The hydraulic resistance (R_H) for the rectangular microchannel can be predicted theoretically according to equation (3-1)[1, 2]. As the capillary effect dominates the flow of the channel where a bubble is locked ($Ca \sim 10^{-4}$), the resistance of the blocked channel is significantly higher than the resistance of other channels

where there is no bubble or interfaces. The channel in which the bubble lodges/blocks can be analogized to a resistor with infinite electric resistance. The equivalent electric circuit and equivalent resistors are shown in Fig. 3.2. The pressure across the blocked channel then can be predicted through Simulink, Matlab. For example, the pressure difference between the two ends of channel A12 (ΔP_{A12}) can be calculated through equations (3-1) and (3-2),

$$R_H = \frac{12\sigma L}{wh^3[1-\frac{h}{w}[\frac{192}{\pi^5}\sum_{n=1,3,5}^{\infty}\frac{1}{n^5}\tanh(\frac{n\pi w}{2h})]]} \quad (3\text{-}1)$$

$$\Delta P_{A12} = \Delta P_{overall} - Q_A R_{H(A)} - Q_{A1} R_{H(A1)} - Q_{A3} R_{H(A3)} - Q_{A4} R_{H(A4)} - Q_{A5} R_{H(A5)} \quad (3\text{-}2)$$

where *w*, *h* and *L* are the microchannel width, height and length, respectively, ΔP_{total} is the experimental overall pressure required to dislodge one bubble from channel A12.

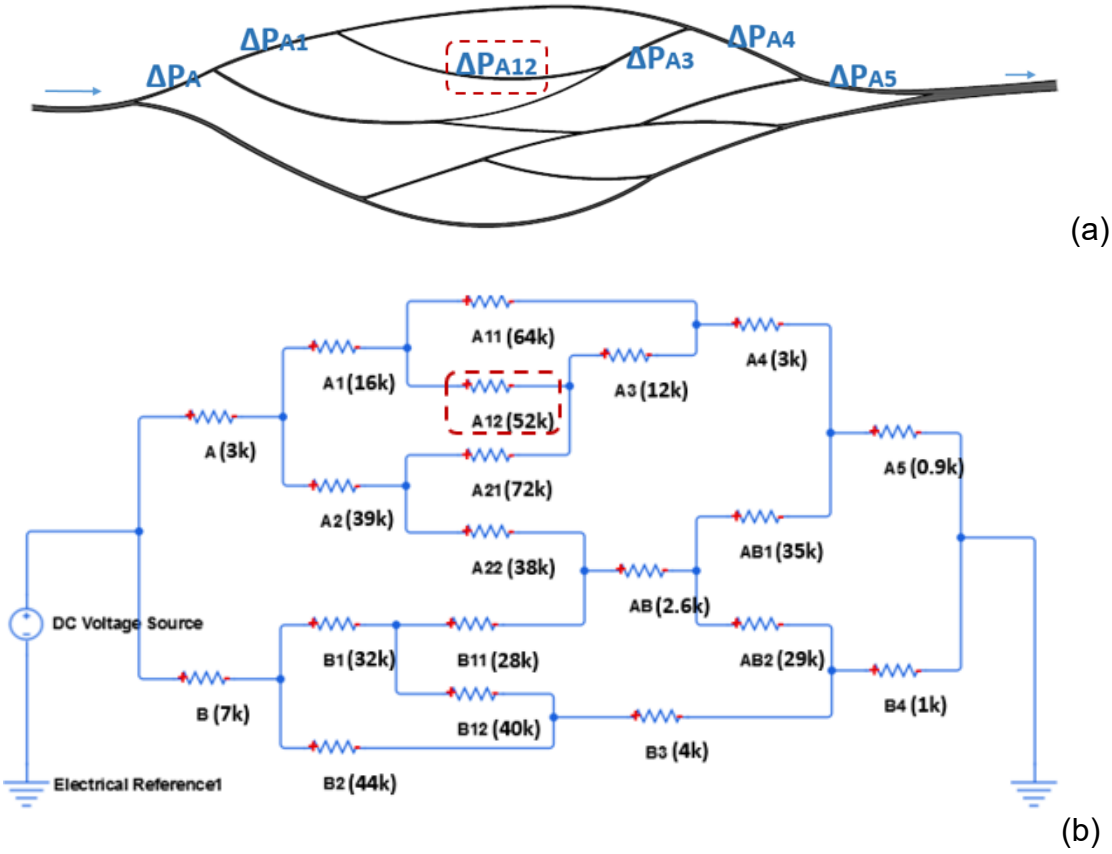

Fig. 3. 2 Illustration of the prediction of ΔP_{A12} (pressure drop in microchannel A12) for dislodging a bubble from channel A12: (a) schematic of Network A, and (b) equivalent electric circuit and resistor (the hydraulic resistance R_H has been labelled, unit: Pa·s·cm^{-3})

3.2 Materials

3.2.1 Liquids with different surface tensions and viscosities

The effect of surface tensions and viscosities on the resistance to two-phase flows in microchannel was investigated through using liquids with various surface tension and viscosities. The physical properties of the fluids were

shown on the Table 3.1. 2-propanol (99+ %, extra pure, ACROS Organics, New Jersey, U.S.A). To measure the impact of fluid surface tension on the resistance, 2-propanol aqueous solutions with various mass fraction provide a good contrast in surface tension, but almost constant in their viscosity. Their surface tension ranges from 21.22 mN/m for pure 2-propanol to 72.0 mN/m for DI water. Their viscosities were very close, ranging from 8.94×10^{-4} Pa·s (for DI water) to 2.07×10^{-3} Pa·s (for 2-propanol), and thus the difference in viscosity among these solutions can be ignored. To measure the impact of fluid viscosity, silicone oils (sourced from MAPLLC Petroleum Crude Oil) were used as their viscosity varies greatly (as shown in Table 3.2) while their surface tension is similar, ranging from 20.1 to 21.2 mN/m.

Table 3. 1 Physical properties of aqueous solutions of 2-propanol and DI water (at 25°C and atmospheric pressure[3, 4])

Concentration (w/w %)	**Density (kg/m^3)**	**Viscosity (Pa·s)**	**Surface tension (mN/m)**
0 (DI water)	997.05	8.94×10^{-4}	71.99
5	974.12	1.725×10^{-3}	49.58
20	913.17	3.040×10^{-3}	30.57
100	718.11	2.070×10^{-3}	21.22

Table 3. 2 Physical properties of silicone oils [5-7]

Silicone oil	Density (kg/m^3)	Viscosity (Pa·s)	Surface tension (mN/m)	Interfacial tension against water (mN/m)
10cst	930	9.3×10^{-3}	19.4	43.4
50cst	960	4.8×10^{-2}	20.8	41.2
100cst	960	9.6×10^{-2}	20.9	41.0
500cst	970	4.85×10^{-1}	21.1	40.5

3.2.2 Gases

As CO_2 (C40-VB, BOC, Manchester), CH_4 (CP Grad (100%), BOC, Surrey) and air are the gases commonly used in fuel cells, gas reservoir and microbubble-aided drug delivery, respectively, they were used to understand the flow resistance to the most common used gas in microchannels. The properties of these gases are shown in Table 3.3. During experiments, 0.1 ml of gas was injected respectively to create the gas-water interface in constricted capillaries.

Table 3. 3 Physical properties of air, CO_2 and CH_4 (at 25°C and atmospheric pressure[8-10])

Gas	Density (kg/m^3)	Surface tension in water (mN/m)	Viscosity (Pa·s)
Air	1.18	71.99	18.5×10^{-5}
CO_2	1.98	72.0 [11]	15.0×10^{-5}
CH_4	0.66	75.5 [9, 10]	11.1×10^{-5}

3.2.3 Constricted capillaries

Constricted capillaries with various size and gradients were made from standard cylindrical glass tubes (borosilicate, bore size 3 mm, 0.5 m long, 6 mm (ext.) diameter; FB51467 Fisher Scientific, UK). The glass tubes were firstly cut into 12 cm tubes. The borosilicate glass is highly hydrophilic, and high-cleaned conditions were required in the entire manufacture and measurement processes. The glass tubes were washed using 5 M sodium hydroxide solution (Fisher Scientific) and acetone (Fisher Scientific, A/0600/15), and rinsed thoroughly with deionized water (C540 Deionizer, Veolia Water Solutions Technologies). The cleaned glass tubes were then heated up to 550 ^oC on butane flame (butane Battery, D2-BS 0617) to remove any organic residue and kept in the dust-proof enclosure. Constricted capillaries with various size were obtained through melting the middle section of the clean glass tubes on flame

and pulling the middle section into capillaries with suitable size. The length of all tapered section was fixed at about 3.5 cm and the tapered section of the capillary was marked to identify the position of the gas-liquid interface corresponding to the measured resistant pressure.

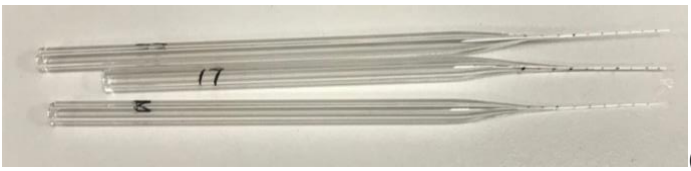
(a)


(b)

Fig. 3. 3 Photos of (a) some tapered capillaries and (b) complex capillary network

3.2.4 Complex capillary network

The capillary network used in this study was engraved on an Acrylic sheet (2mm, Acrylic Cast, AMARI, contact angle is around 68º[12]) with a fusion laser engraving and cutting system (Epilog laser fusion M2). The network structures, as shown in Figs 3. 3(b) and 3.4, were designed based on Murray's law, which states that under ideal conditions, when a parent blood vessel branches into daughter vessels, the cube of the radius of the parent vessel is equal to the sum of the cubes of the radii of daughter blood vessels[13]. Network A mainly focuses on the effect of the network structure, i.e. network complexity, multiple

channels and multiple bifurcations on the flow resistance to bubble in porous media, and Network B is used to characterize the effect of the bifurcation angle on the flow resistance to bubbles. As the leaser cutting cannot make a circular cross section, the shape of the channel cross sections was rectangular in this study. In practice, for example in electronic device, electrodes and porous rocks, the micro-channels are not necessary to have circular cross section. The blood vessels in human body also have non-circular cross-sections according to the anatomic quantifications. The circular shape of blood vessels can distort and change with dilation and constriction [14].

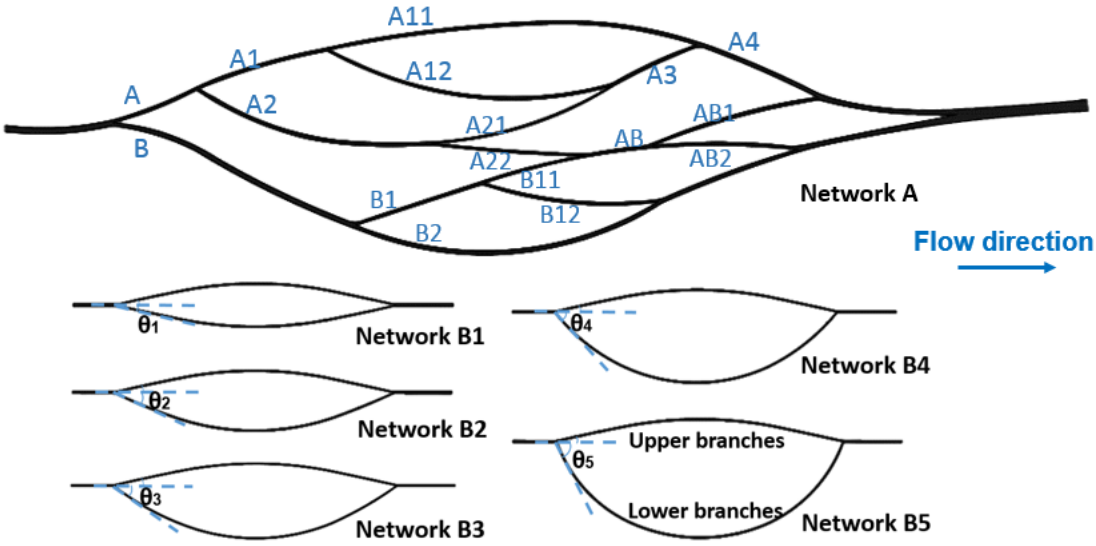

Fig. 3. 4 Schematics of the designed Network A and Network B1-B5 (each channel in capillary network is labelled)

The microfluidic Network A and B were engraved by soft lithography techniques (Epilog laser fusion M2) in an Acrylic sheet (2mm, Acrylic Cast, AMARI, contact

angle is around 68º[15]). The cross sections of microchannels are rectangular due to the nature of the soft-lithography techniques. All parameters of Network A are shown in Table 3. 4. In Networks B1-B5, the widths and heights of upper and lower branches are identical (0.4 mm), and the branching angles (θ_1-θ_5) ranges from 12- 66˚.

Table 3. 4 Width and length of microchannels in Network A (The microchannel height is uniform, approximately 0.32 mm)

Channel	**Width (mm)**	**Length (cm)**	**Channel**	**Width (mm)**	**Length (cm)**
A11	0.46	6.15	AB1	0.45	2.65
A12	0.46	5.05	AB2	0.45	2.40
A21	0.26	2.95	B11	0.36	1.55
A22	0.37	2.40	B12	0.41	3.00

3.3 Reference

1. Oh, K.W., et al., *Design of pressure-driven microfluidic networks using electric circuit analogy.* Lab Chip, 2012. **12**(3): p. 515-45.10.1039/c2lc20799k

2. Kim, D., N.C. Chesler, and D.J. Beebe, *A method for dynamic system characterization using hydraulic series resistance.* Lab on a Chip, 2006. **6**(5): p. 639-644.10.1039/b517054k

3. Pang, F.M., et al., *Densities and viscosities of aqueous solutions of 1-propanol and 2-propanol at temperatures from 293.15 K to 333.15 K.* Journal of Molecular Liquids, 2007. **136**(1-2): p. 71-78.10.1016/j.molliq.2007.01.003

4. Vazquez, G., E. Alvarez, and J.M. Navaza, *Surface-Tension of Alcohol Plus Water from 20-Degrees-C to 50-Degrees-C.* Journal of Chemical and Engineering Data, 1995. **40**(3): p. 611-614.Doi 10.1021/Je00019a016

5. Chan, W.K. and C. Yang, *Surface-tension-driven liquid-liquid displacement in a capillary.* Journal of Micromechanics and Microengineering, 2005. **15**(9): p. 1722-1728.10.1088/0960-1317/15/9/014

6. Giordano, G.G. and M.F. Refojo, *Silicone oils as vitreous substitutes.* Progress in Polymer Science, 1998. **23**(3): p. 509-532.Doi 10.1016/S0079-6700(97)00046-4

7. Peterson, J.W. and J.C. Berg, *Surface Fractionation of Multicomponent Oil Mixtures.* Industrial & Engineering Chemistry Fundamentals, 1986. **25**(4): p. 668-677.Doi 10.1021/I100024a032

8. Hebach, A., et al., *Interfacial Tension at Elevated PressuresMeasurements and Correlations in the Water + Carbon Dioxide System.* Journal of Chemical & Engineering Data, 2002. **47**(6): p. 1540-1546.10.1021/je025569p

9. Hough, E.W., M.J. Rzasa, and B.B. Wood, *Interfacial Tensions at Reservoir Pressures and Temperatures - Apparatus and the Water-Methane System.* Pet. Trans. AIME, 1951. **192**(02): p. 57-60, <Go to ISI>://WOS:A1951XR34500008

10. Jennings Jr, H.Y. and G.H. Newman, *The effect of temperature and pressure on the interfacial tension of water against methane-normal decane mixtures.* Soc. Pet. Eng. J, 1971. **11**(02): p. 171-175,

11. Hebach, A., et al., *Interfacial tension at elevated pressures - Measurements and correlations in the water plus carbon dioxide system.* Journal of Chemical and Engineering Data, 2002. **47**(6): p. 1540-1546.10.1021/je025569p

12. Cavanagh, D.P. and D.M. Eckmann, *Interfacial dynamics of stationary gas bubbles in flows in inclined tubes.* Journal of Fluid Mechanics, 1999. **398**: p. 225-244.Doi 10.1017/S0022112099006230

13. Chen, Y.P. and Z.L. Deng, *Gas flow in micro tree-shaped hierarchical network.* International Journal of Heat and Mass Transfer, 2015. **80**: p. 163-169.10.1016/j.ijheatmasstransfer.2014.09.016

14. Gao, Y.R. and P.J. Drew, *Determination of vessel cross-sectional area by thresholding in Radon space.* J. Cereb. Blood Flow Metab., 2014. **34**(7): p. 1180-7.10.1038/jcbfm.2014.67

15. Kwok, D.Y., et al., *Contact angle measurements and interpretation: wetting behavior and solid surface tensions for poly(alkyl methacrylate) polymers.* J Adhes Sci Technol, 2000. **14**(5): p. 719-743.Doi 10.1163/156856100742843

Chapter 4: Effect of gas-liquid interfaces on the two-phase flows in constricted microchannels[1]

4.1 Introduction

Immiscible two-phase flow in porous media is of great importance to many fields, such as oil recovery [1], CO_2 sequestration [2], underground water remediation [3], water management in fuel cells [4], micro reactors [5], electronic chips [6], compact heat exchangers [7, 8], biotechnology and microbubbles for drug delivery [9-11]. Bead/sand-packed models, glass capillary models or a bundle of capillaries have been frequently used to mimic the complex inner structure of the porous media [12-14], which represents the geometrical feature of porous media to some degree. The pore and pore throat, as the basic geometrical element, can be represented by single microchannels with various pore diameter or with constricted section.

Commonly, a criterion to characterize the efficiency of the migration and transport processes is the resistance to two-phase flows in porous media, which can be evaluated through the pressure drops across fluids flowing through the porous media. The pressure drop is controlled by pore structure (such as pore size, pore shape, and pore throat) [15-17], pore surface wettability [18-20], fluid properties (such as viscosity and surface tension), fluid

[1] Some contents of this chapter have been published in Chemical Engineering Science 192 (2018) 114–125

velocity and the interface of two fluids[21]. Even though there are many numerous investigations reported in literature, to author's best knowledge, many aspects in pore resistance to fluids in porous media are still unclear. For example, it is well known that capillary force is one of the important factors controlling the gas-liquid interface in micro-channels. However, we do not clearly know when the capillary force starts to take effect with the progress of the interface into the porous media; pore throat, as one of the essential parameters of pore structure, significantly controls the resistance to two-phase flows in porous media. However, there is no clear definition for what pore size can be seen as a hydrodynamic throat. In pore-scale network modelling, the throat is roughly defined by subtracting the two pore lengths, which is somewhat arbitrary as pointed out by Blunt[22]. Understanding the point at which the resistance starts to take effect on the fluids in the constricted section of the capillary will help to segment the pore and the throat concisely.

In this chapter, experiments were designed to investigate when the capillary force starts to take effect in a constricted micro-channel, the detailed contribution of gas-liquid interfaces to the capillary resistance in micro-capillaries, and to define an effective pore throat. A new correlation based on Darcy-Weisbach equation is developed to calculate the frictional pressure drop for constricted flow channels. The frictional pressure drop for two-phase flows will be predicted through our new-derived Darcy-Weisbach equation coupled with the homogenous flow model and the separated flow model. Our new-

derived equation will be verified through comparing with the experimental frictional pressure drop for two-phase flows in constricted capillaries.

4.2 Difference in pressure drop profiles for single-phase and two-phase flows in constricted capillaries

The typical pressure profiles for single-phase (DI water) flows and for two-phase (air-water) flows in constricted capillaries are presented in Figs. 4.1-4.2. The results indicate that the resistant pressure profile for a two-phase flow is significantly different from that for a single-phase flow. For a single-phase flow (as shown in Figs. 4.1a and 4.2a), the pressure profile has two sections, the initial increase section (0-A) and the pressure balance section (after point A). The initial increase in resistant pressure is due to the fluid acceleration as the resistant pressure is increased with the increase in fluid velocity. Once the fluid flowrate in the capillary is equal to the injection flowrate, the acceleration stops, thus the pressure reaches the balance, and the resistant pressure takes a constant value.

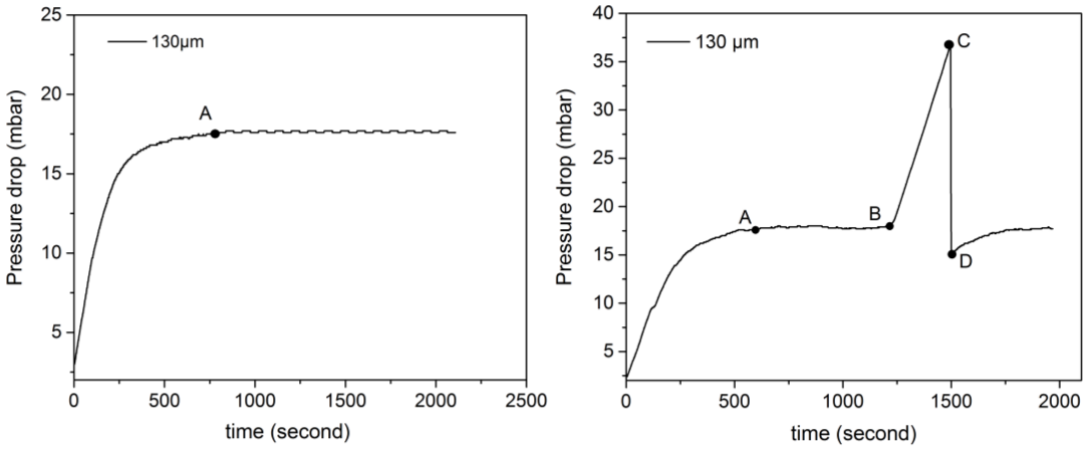

(a) (b)

Fig. 4. 1 Resistant pressure profiles for (a) the single-phase (water) flow and (b) the two-phase flow in a constricted capillary with a tip size of 130 μm

For a two-phase flow, the pressure profile can be divided into three sections, the initial increase section (fluid acceleration stage, 0-A), pressure balance section (A-B) and the dramatic increase section (B-C), as shown in Fig. 4.1b. The initial increase section is due to the acceleration of the fluid. The B point in Fig. 4.1b corresponds to the point P in Fig. 4.3, which is the 'effective pore throat' defined in the next section. From the pressure profiles for two-phase flows, it can be seen that the resistant pressure not only varies with the fluid velocity and capillary size, but also varies with the position of the air-water interface in the constricted capillary. Before the air-water interface approaches the point B in a constricted capillary, the pressure profile for a two-phase flow took a constant value, and was almost the same as the pressure profile for the single-phase flow. Once the air-water interface reached the position with a pore

diameter less than the point B (or *P* as shown in Fig. 4.3), a sharp increase at a constant rate in the resistant pressure profile was observed. The resistant forces applied to the air-water interface are mainly composed of the frictional force and the capillary force. The frictional force caused by the air-water interface is very small due to the low viscosity of air. Therefore, this sudden occurrence of 'sharp increase' can be explained that the capillary resistance to the air- water interface starts to take effect from this critical pore diameter.

The dramatic increase in resistant pressure profiles can be observed for two-phase flows in all constricted capillaries with tip sizes from 91 to 257 μm, but was not in pressure profiles of single-phase flows. Figs. 4.2a and 4.2b also show that the effect of capillary tip size on the resistant pressure profiles for both single-phase and two-phase flows in constricted capillaries. The results indicate that at the equilibrium state, the pressure drop to single-phase (DI water) flows decreases significantly with the increase in the capillary tip size (as shown in Fig. 4.2a). This can be explained by the Hagen-Poiseuille or Darcy-Weisbach equation. As the main resistance to single-phase flows is the frictional force, under the same injection flowrate, the frictional pressure decreases with the increase in the radius of the flow channel. Fig. 4.2b shows that in two-phase flows, the capillary tip size affects the resistant pressure to both the phase body and the two-phase interface. Generally, the larger the capillary tip size, the smaller the resistant pressure to the two-phase flows.

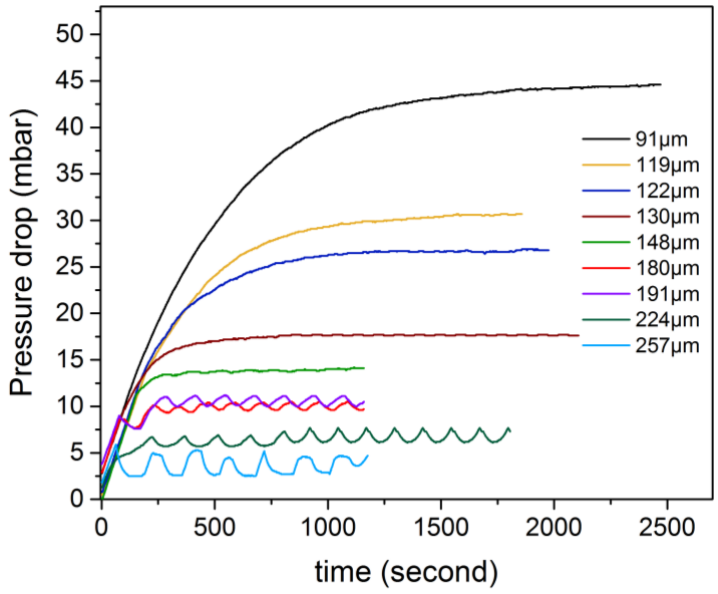

(a)

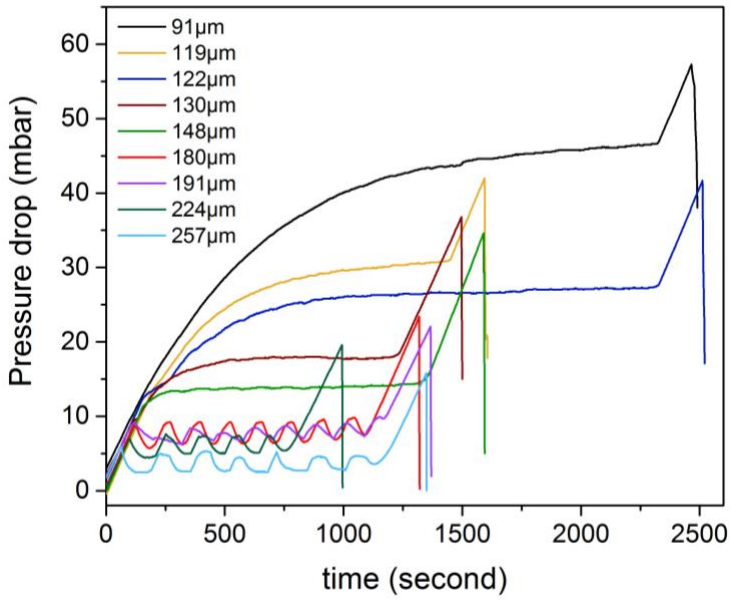

(b)

Fig. 4. 2 Resistant pressure profiles for (a) single-phase (DI water) flows and (b) two-phase flows in constricted capillaries with tip size ranging from 91-257 μm

4.3 Effective pore throat

To define the point at which capillary force to the two-phase interface starts taking effect, the change in the pressure drop with the position of the two-phase interface in the constricted capillary is presented in Fig. 4.4. The diameter on x-axis corresponds to the position of two-phase interface in the constricted capillary. For example, the point (220 μm, 27 mbar) in Fig. 4.4 means that the measured resistant pressure is 27 mbar when the two-phase interface flows to the position with an inner diameter of 220 μm. The relationship between the pressure and the position of the two- phase interface was obtained through recording the pressure drop and the corresponding interface motion micrographs. The results clearly show that, when the two-phase interface moves along the capillary with a pore diameter greater than point *P*, the resistant pressure to the air-water interface is almost zero, and the resistant pressure to the two-phase flow is the same as the resistant pressure to a single-phase flow. However, once the pore diameter of capillary is less than point *P*, the pressure drop for the air-water interface increases sharply. We define this point *P* as the ‘effective pore throat’, and the schematic of an effective pore throat was shown in Fig. 4.3.

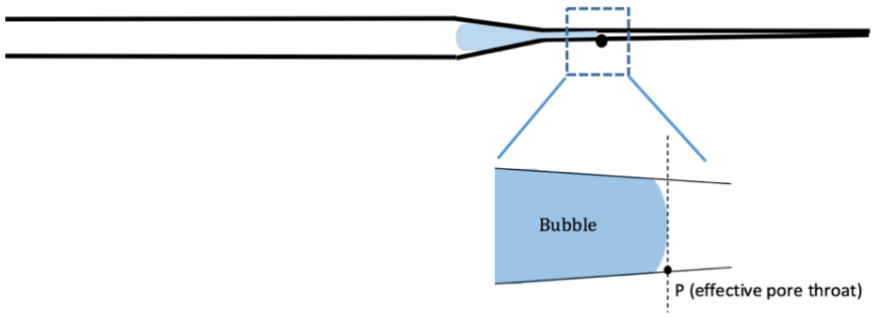

Fig. 4. 3 Schematic of an effective pore throat in a constricted capillary

To identify the effective pore throat based on the measured pressure profile, two linear lines were obtained through the fitting of the experimental data as shown in Fig. 4.4a. The diameter corresponding to the value of the intersection of the two lines is seen as the effective pore throat. In Fig. 4. 4a, the effective pore throat for the constricted capillary with a tip size of 130 μm is on the capillary with the pore diameter of 293 μm. To verify the pore throat obtained through this method, we recorded the motion of two-phase interfaces in the capillaries and the pressure drop simultaneously, and then found the effective pore throats corresponding to the sudden increase in the measured pressure drop profiles. The effective pore throat obtained through these two methods matches very well. Using the same approach, the diameter of effective pore throat for all constricted capillaries with tip sizes ranging from 91 to 257 μm is obtained and the results are shown in Fig. 4. 4b. It is interesting to notice that the smaller the tip size of a constricted capillary, such as 91 μm, 105 μm, 119 μm and 122 μm, the greater the increase rate of resistant pressure would be.

For constricted capillaries with larger tip sizes, such as 180 μm, 191 μm, 224 μm and 257 μm, the resistant pressure increases at a relatively gentle rate after the effective pore throat.

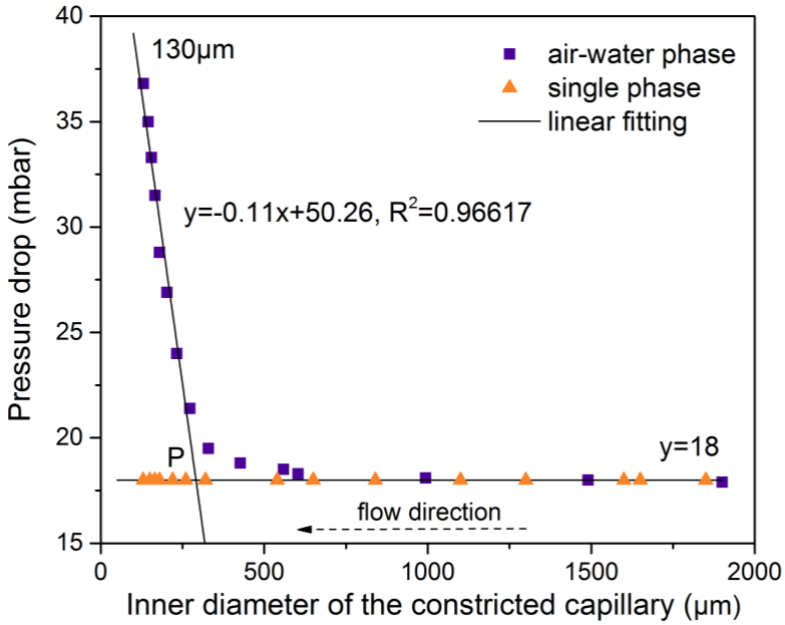

(a)

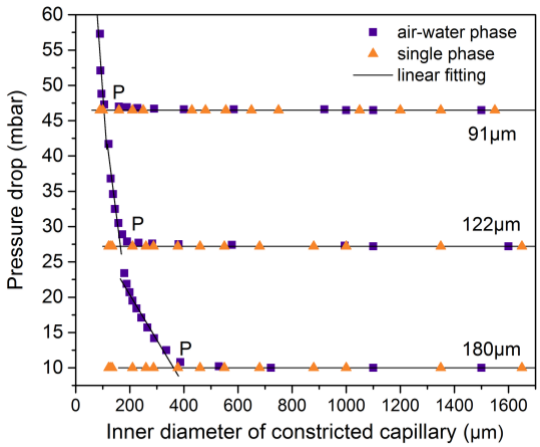

(b1)

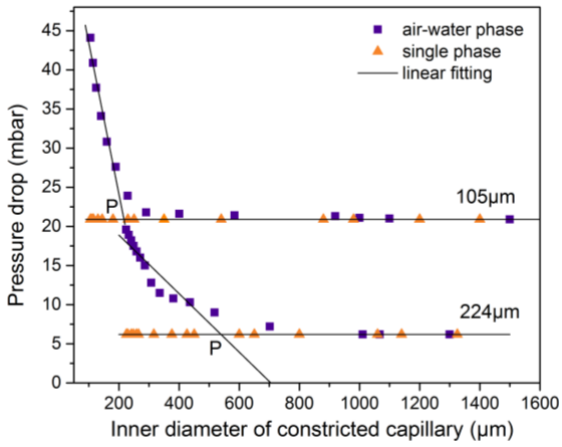

(b2)

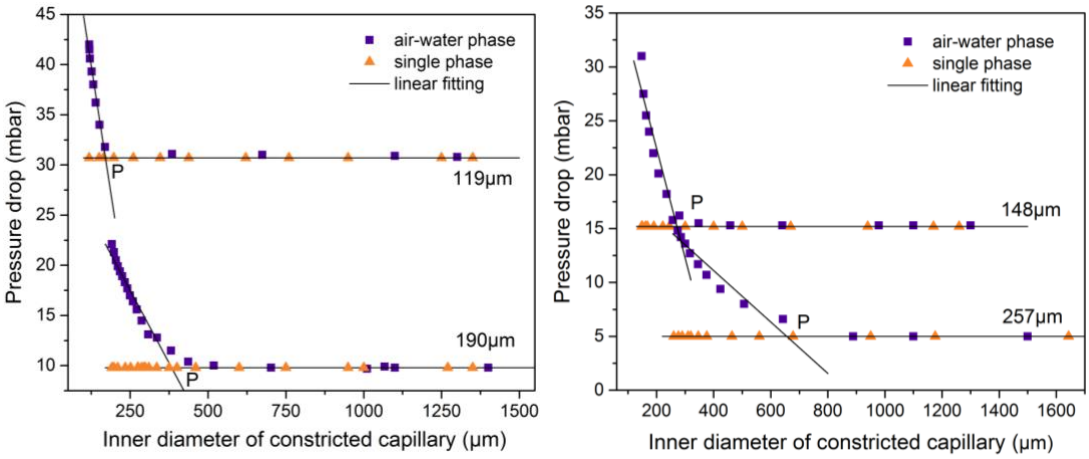

(b3) (b4)

Fig. 4. 4 Effect of the position of two-phase interface on the pressure drop in the constricted capillary with (a) the tip size of 130 μm, and (b) tip sizes ranging from 91-257 μm

This effective pore throat tells where the capillary resistance to two-phase interface takes effect in constricted capillaries. The overall resistance to two-phase flows can be regarded as two parts: the resistance to air-water interface and the resistance to the water phase. The resistant pressure profiles for two-phase and single-phase flows overlap before the Point P. This indicates that the resistance to the air-water interface is almost zero before interface touches the effective pore throat. Once the air-water interface flows to the effective pore throat, the resistance to the two-phase flows suddenly increases. Thus, the effective pore throat is the critical point to tell whether the capillary resistance would take a significant influence on the two-phase flows in constricted

capillaries. Fig. 4.5 shows that the effect of capillary tip diameter on the size of the effective pore throat in constricted flow channels. The larger the capillary tip diameter, the larger the effective pore throat size would be. This is in good agreement with the result obtained by Zou et al. (2012). They measured pore throat diameter of sandstone core samples and found that the pore throat size increased with the pore diameter of sandstone. Needs to mention that, this effective pore throat only exists in microscopic capillaries. The constricted capillary with a diameter greater than 870 μm barely has this 'sharp increase in resistant pressure drop' and the effective pore throat.

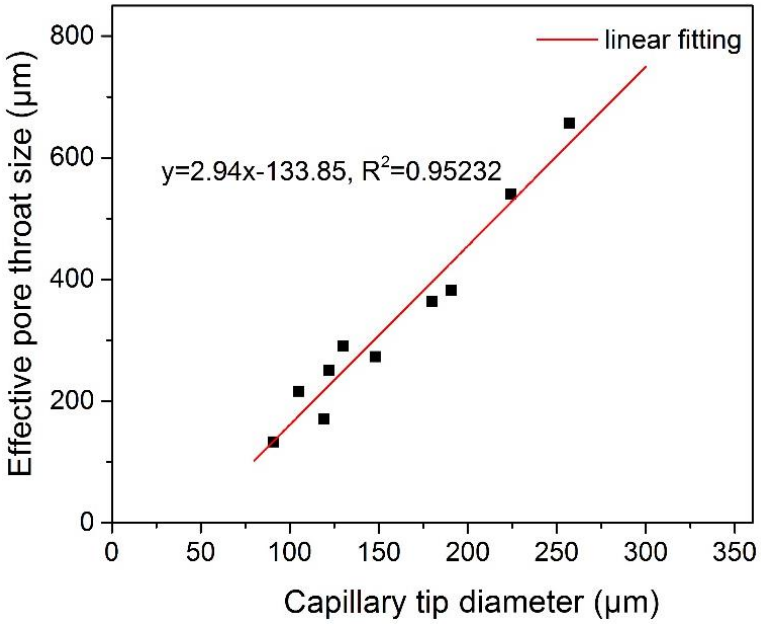

Fig. 4. 5 Effect of capillary tip diameter on the effective pore throat

4.4 Simulation of pressure drop to two-phase flows in constricted capillaries

4.4.1 Pressure drop to two-phase flows in constricted capillaries

The pressure drop of a two-phase flow in a constricted capillary is formed by the effect of capillary force, viscosity force, buoyancy force, inertial force and gravity force. The inertial effects and gravitational or buoyancy effects is neglected as the *We* and *Bo* number are much less than 1 [45] [23, 24]. For the case that capillary number is less than 10^{-5}, capillary force should be included. In this study, the thickness of the liquid film near the capillary wall, *d*, calculated by Equation (2-2) is negligible and thus the effective flow diameter of fluids can be assumed to be equal to the capillary diameter.

Table 4. 1 The value of each parameter in this chapter

u	2.36×10^{-5}- 0.0262 m/s	***Re***	7.9×10^{-2}- 2.65
Ca	2.90×10^{-7}- 3.24×10^{-4}	***We***	1.16×10^{-8}- 4.33×10^{-4}
Bo	1.10×10^{-3}- 1.22		

4.4.1.1 Derived frictional pressure equation based on Darcy-Weisbach equation

The Darcy-Weisbach equation is used to calculate the frictional pressure drop

to fluids flow in channels with a constant diameter. In our experiments, the inner diameter of the tapered section of capillaries is not constant and the geometry of constricted capillary is a circular truncated cone. In order to fit the geometry, a new correlation is derived based on Darcy-Weisbach equation to calculate the frictional pressure loss. We assume that the inner diameter of the tapered section of constricted capillary is decreased at a constant gradient, *k*, defined as:

$$k = (r_{et} - r_{tip})/L \tag{4-1}$$

where r_{et} and r_{tip} are the radius of the effective pore throat and the capillary tip, respectively. *L* is the capillary length from the effective pore throat point to the tip, as shown in Fig. 4.6.

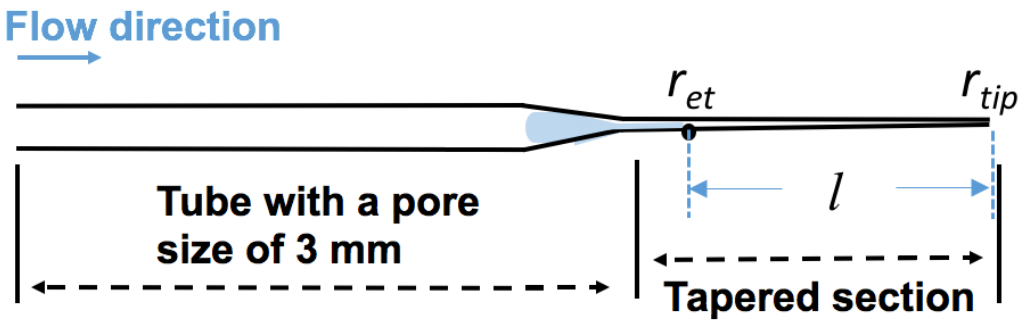

Fig. 4. 6 Schematic of a constricted capillary

For the interface flows into the point with a radius of *r*, the distance of the interface to the effective pore throat, l can be expessed as:

$$l = (r_{et} - r)/k \tag{4-2}$$

Then, differentiating equation (4-2), gives,

$$dl = -\frac{1}{k}dr \tag{4-3}$$

The superficial velocity of fluids in capillaries, u gives,

$$u = \frac{Q}{A} = \frac{Q}{\pi r^2} \tag{4-4}$$

Substituting (4-3) and (4-4) into Darcy-Weisbach equation (2-15) gives,

$$\sum P_f = \int -\frac{f\rho Q^2}{4k\pi^2 r^5}dr \tag{4-5}$$

Integrating equation (4-5), gives,

$$\Delta P_f = \frac{f\rho Q^2}{\pi^2 k r^4} \tag{4-6}$$

This new derived equation (4-6) will be used to calculate the frictional pressure drop for two-phase flows in constricted capillaries.

4.4.1.2 Simulation of frictional pressure drop for two-phase flows in constricted capillaries

The frictional pressure drop for two-phase flows in constricted capillary will be predicted through our newly-derived equation coupled with (1) the homogeneous flow model and (2) the separated flow model.

In the homogeneous flow model, the new derived equation (4-6) becomes,

$$\Delta P_{TP} = \frac{f_{TP}\rho_m Q^2}{\pi^2 k r^4} \tag{4-7}$$

For laminar flow,

$$f_{TP} = \frac{64}{Re_m} \tag{4-8}$$

the Reynolds number of mixture is given by,

$$Re_m = \frac{\rho u D}{\mu_m} \tag{4-9}$$

Substituting (4-8) and (4-9) into equation (4-7), gives,

$$\Delta P_{TP} = 32 \frac{\mu_m Q}{\pi k r^3} \tag{4-10}$$

In HFM, the frictional pressure drop for two-phase flows in constricted capillaries can be predicted through new-derived equation (4-10) coupled with viscosity correlations (given in Table 4.2) which is used to evaluate the mixture viscosity, μ_m.

Table 4. 2 Dynamic viscosity correlations for two-phase flows

Authors	**Correlations**
McAdams **[25]**	$\frac{1}{\mu_m} = \frac{x}{\mu_g} + \frac{1-x}{\mu_l}$
Cicchitti et al. **[26]**	$\mu_m = x\mu_g + (1-x)\mu_l$
Dukler et al. **[27]**	$\mu_m = \beta\mu_g + (1-\beta)\mu_l;\ \beta = \frac{Q_g}{Q_g+Q_l}$, Q is the volumetric flow rate of gas (g) and liquid (l).
Beattie and Whalley **[28]**	$\mu_m = \beta\mu_g + (1-\beta)(1+2.5\beta)\mu_l$
Lin et al. **[29]**	$\mu_m = \frac{\mu_l\mu_g}{\mu_g + x^{1.4}(\mu_l - \mu_g)}$
Garcia et al. **[30]**	$\mu_m = \frac{\mu_l\rho_g}{x\rho_l + (1-x)\rho_g}$

In the separated flow model, the frictional pressure drop for two-phase flows, ΔP_{TP} is obtained through combining our new derived equation (4-6) with equation (2-18), i.e.

$$\Delta P_{TP} = \phi^2 \Delta P_{SP} = \phi^2 \frac{f \rho_l Q^2}{\pi^2 k r^4} \quad (4\text{-}11)$$

where ϕ^2 is determined by the constant *C* according to equation (2-19). The *C* value of 5 was commonly used under the condition where the *Re* number is less than 1000. However, Chung and Kawaji [31], Yue, et al. [14], and Saisorn and Wongwises [13], reported that in microchannels, the *C* value of 5 gave a large deviation for the prediction of pressure drop for two-phase flows. To reduce this deviation, we use the correlation (4-12) from Saisorn and Wongwises to calculate the *C* value. The reason to choose this correlation is that the inner diameter of cylindrical capillary used by Saisorn and Wongwises is 150 μm and the capillary material is silica [13], similar to our experiments.

$$C = 7.599 * 10^{-3} \lambda^{-0.631} \psi^{0.005} Re_l^{-0.008} \quad (4\text{-}12)$$

where λ and ψ were defined by Suo and Griffith [32], given as,

$$\lambda = \frac{\mu_l^2}{\rho_l \gamma D} \quad (4\text{-}13)$$

$$\psi = \frac{\mu_l u_l}{\gamma} \quad (4\text{-}14)$$

4.4.1.3 Overall pressure drop for two-phase flows in constricted capillaries

The overall pressure drop to two-phase flows ΔP, in a glass tube with an inner diameter of 3 mm and the tapered section as shown in Fig. 4. 6, is given by,

$$\Delta P = \Delta P_{f1} + \Delta P_{f2} + \Delta P_c + \Delta P_{contraction} \quad (4\text{-}15)$$

where ΔP_{f1} is the frictional pressure drop in the tube with an inner diameter of 3 mm, ΔP_{f2} is the frictional pressure drop for fluid flowing through the tapered section of the capillary, $\Delta P_{contraction}$ is the pressure loss due to the sudden contraction and ΔP_c is the capillary pressure.

The frictional pressure for two-phase flows in constricted capillaries ΔP_f will be calculated by new equation (4-6) combined with the homogenous flow model and the separated flow model. The capillary pressure will be calculated through Young-Laplace equation, as shown as Equation (2-12). $\Delta P_{contraction}$ is calculated through Equation 2-13, and the calculated results indicate that in this study, the pressure loss due to capillary geometry contraction is negligible. For example, for a constricted capillary with a tip size of 130 μm and the effective pore throat size of 293 μm, $\Delta P_{contraction}$ was only 7.7×10^{-6} mbar.

4.4.2 The accuracy of new-derived equation

To verify our newly derived equation, the frictional pressure drop for two-phase

flows in constricted capillaries predicted using our newly derived equation is compared with the experimental results. Fig. 4.7 suggests that the frictional pressure drop predicted through our new-derived equation with different flow models is fairly accurate (Fig. 4.7a) in comparison with the results calculated through Darcy-Weisbach equation (Fig. 4.7b). The frictional pressure drop calculated through Darcy-Weisbach equation is far away from the experimental results. However, combined with the Separated flow model, our new-derived equation can obtain the frictional pressure drop for two-phase flows with a deviation of near ±10% for all capillaries with tip diameters ranging from 116.8 to 257 μm (Fig. 4.7c). Compared with SFM which adapts to all capillaries, our new-derived equation combined with Beattie model can predict the frictional pressure drop within a deviation of ±20% for capillaries with relatively small size (below 200 μm). Other five viscosity models underestimated the frictional pressure drop for two-phase flows in all constricted capillaries.

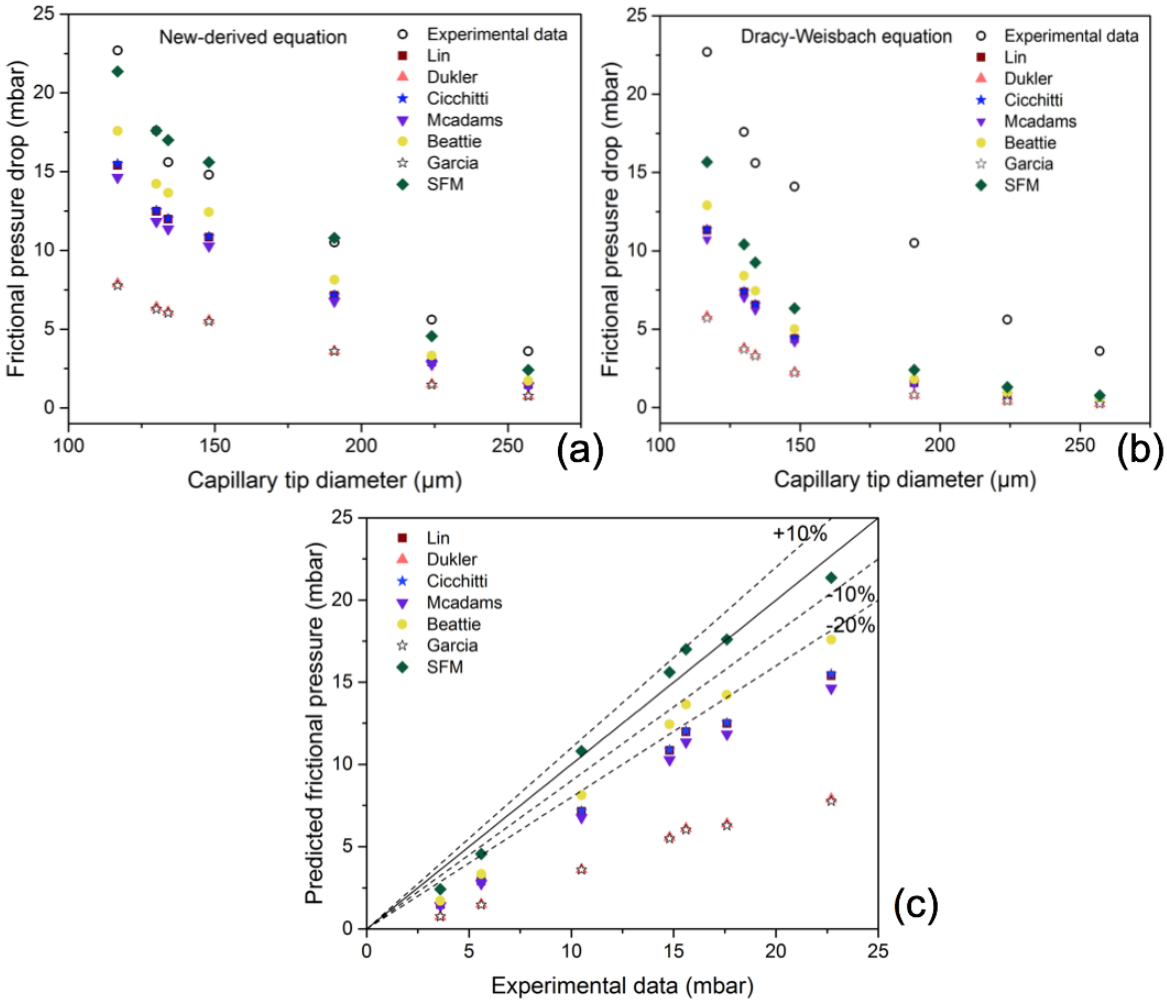

Fig. 4. 7 Simulated frictional pressure drop through (a) the new-derived equation, (b) conventional Darcy-Weisbach equation, and (c) the accuracy of simulated frictional pressure compared with measured frictional pressure drop for two-phase flows in constricted capillaries ranging from 116.8 to 257 μm

Although the new-derived equation is less than ideal, it is more adaptable than Darcy-Weisbach equation for predicting the frictional pressure drop in constricted capillaries. It is expected that a more applicable *C* value will improve the accuracy of our new derived equation to predict the frictional pressure drop

for constricted capillaries. The *C* value used in current SFM simulation may be relatively larger than the actual value. Saisorn and Wongwises correlation fits the superficial liquid velocity between 0.37- 42.36 m/s, while the velocity in our study (about 0.0262 m/s) was much lower than that. As the parameter *C* is dependent on fluid velocity and capillary diameter [31, 33], the actual *C* under our experimental conditions should be smaller than the value evaluated through Saisorn and Wongwises correlation.

4.4.3 Discussion

The prediction of overall resistant pressure for two-phase flows is obtained by adding up the capillary pressure drop and frictional pressure drop. Fig. 4.8 indicates that the overall pressure drop for two-phase flows in constricted capillaries with an inner diameter less than the effective pore throat, to some degree, can be predicted (within a deviation of ±20%) through the combination of our new-derived equation and Young-Laplace equation. However, the predicted resistant pressure profile (as shown in Fig. 4.8 and Fig. 4.9) cannot fit the entire measured pressure profile, i.e. the simulation results are not satisfactory before the two-phase interface is approaching the effective pore throat.

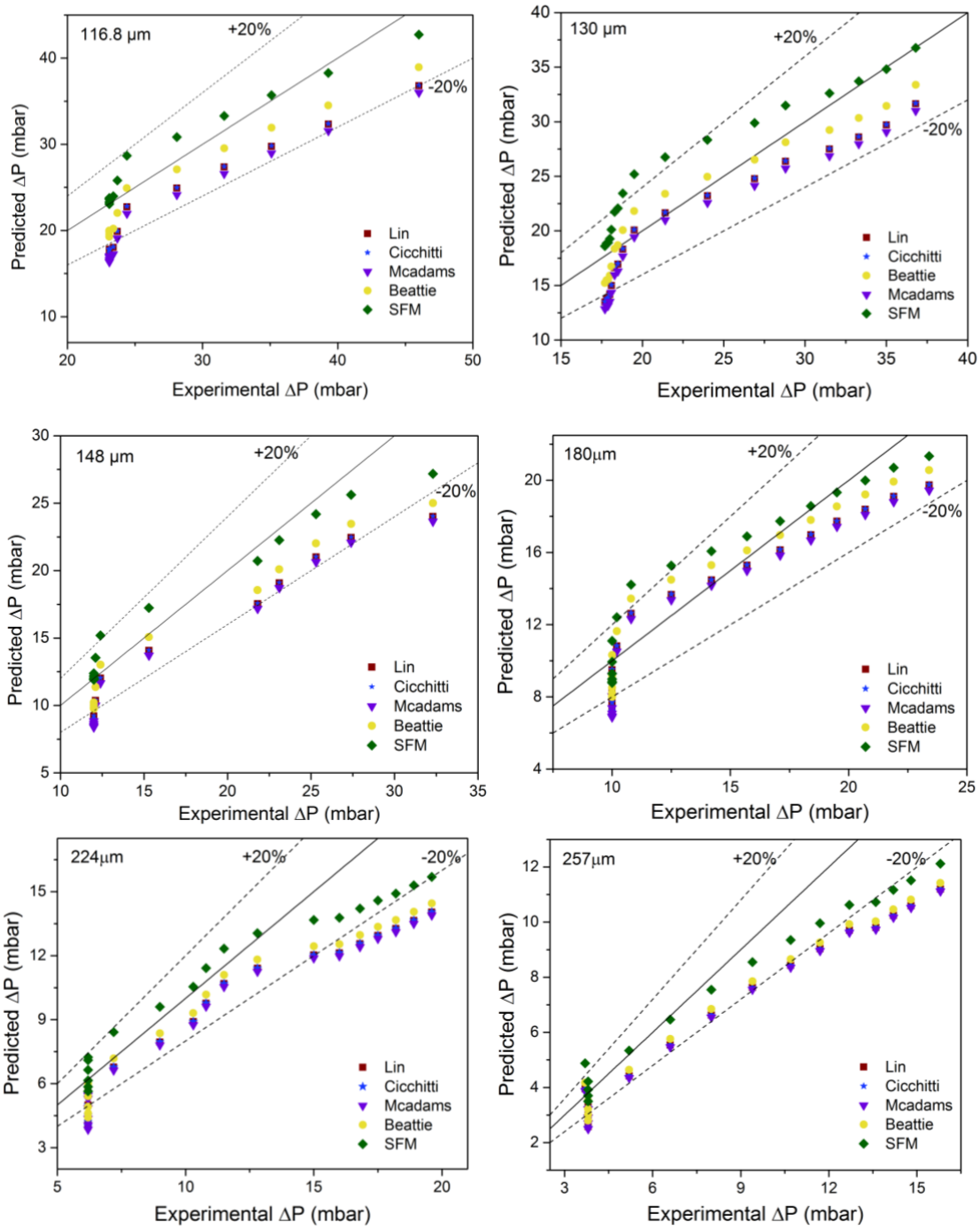

Fig. 4. 8 Measured pressure drop versus the predicted pressure drop for two-phase flows in constricted capillaries with tip size ranging from 116.8 to 257 µm

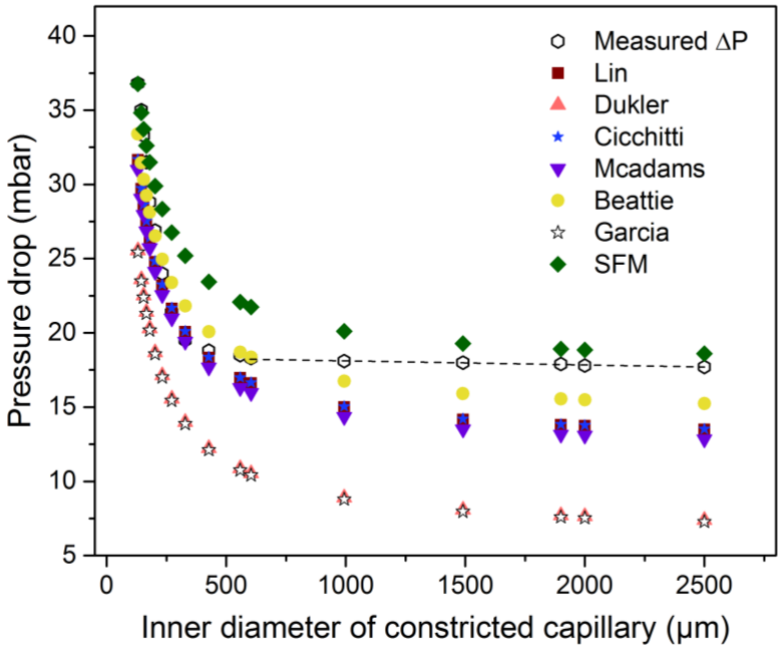

Fig. 4. 9 Change of predicted and measured pressure drop with the flow path diameter in a constricted capillary with a tip size of 130 μm

Moreover, the effective pore throat cannot be identified through the predicted pressure drop profiles. Fig. 4.9 compares the measured pressure drops (the hollow hexagon) for two-phase flows in a constricted capillary with the predicted results. The predicted pressure drop profiles take reciprocal relationship with the diameter of flow path, increasing smoothly with the decease of the inner diameter of the constricted capillaries. However, the measured pressure drop profiles clearly show the effective pore throat. Before the two-phase interface meets the effective pore throat, the pressure drop does not change with the pore diameter (the horizontal line), different with the predicted pressure profile in which the pressure drop smoothly changes with the pore diameter within a

large range. The simulation also fails to explain the sudden increase in resistant pressure once the interface meets the effective pore throat point. The reasonable explanation is that Young-Laplace equation did not consider the effective pore throat. The capillary force calculated is smoothly varied with the pore diameter, while the experiment results show that capillary force starts to take effect only when the pore diameter is smaller than the diameter of the effective pore throat

4.5 Summary

In this chapter, experimental measurements have been designed to investigate the impact of the interface on the fluids flows in constricted microchannels through comparing the difference in the pressure drop for single-phase flows and two-phase flows, and the threshold of pore size where capillary force starts to take effect in micro-channels, and to define the effective pore throat. Simulation work is also conducted to predict the resistant pressure for two-phase flows in constricted capillaries. The results indicate that:

1. The results indicate that for a single-phase flow the pressure drop takes a constant value once the flow acceleration is zero. For a two-phase flow, the pressure drop is equal to the resistance to the single-phase flow, plus the resistance to the gas-water interface.
2. There is a critical point on the constricted capillaries. Before the gas-

water interface reaches this critical point, the capillary resistance to the interface is zero. After this critical point, the capillary resistance to the interface starts to take effect and increase suddenly and sharply. We define this critical point as the 'effective pore throat'. There is no effective pore throat for a single-phase flow.

3. Simulation results of overall pressure drop for two-phase flows agreed well with the measured data only when the flow channel with a pore diameter less than the effective pore throat, but cannot match the entire pressure profiles. Theory and simulation used in this chapter cannot identify the effective pore throat of a constricted microchannel, and cannot explain why the increase in resistant pressure occurs suddenly at the effective pore throat.

4.6 Reference

1. Ringrose, P.S., et al., *Immiscible flow behaviour in laminated and cross-bedded sandstones.* Journal of Petroleum Science and Engineering, 1993. **9**(2): p. 103-124.Doi 10.1016/0920-4105(93)90071-L

2. Cvetkovic, V. and G. Dagan, *Reactive Transport and Immiscible Flow in Geological Media. II. Applications.* Proceedings of the Royal Society A:

Mathematical, Physical and Engineering Sciences, 1996. **452**(1945): p. 303-328.10.1098/rspa.1996.0017

3. Tsakiroglou, C.D. and A.C. Payatakes, *Characterization of the pore structure of reservoir rocks with the aid of serial sectioning analysis, mercury porosimetry and network simulation.* Advances in Water Resources, 2000. **23**(7): p. 773-789.Doi 10.1016/S0309-1708(00)00002-6
4. Quan, P. and M.C. Lai, *Numerical study of water management in the air flow channel of a PEM fuel cell cathode.* Journal of Power Sources, 2007. **164**(1): p. 222-237.10.1016/j.jpowsour.2006.09.110
5. Tanimu, A., S. Jaenicke, and K. Alhooshani, *Heterogeneous catalysis in continuous flow microreactors: A review of methods and applications.* Chemical Engineering Journal, 2017. **327**: p. 792-821.10.1016/j.cej.2017.06.161
6. Lian, Z., et al., *Measurements and modeling of two-phase flow in microchannels with nearly constant heat flux boundary conditions.* Journal of Microelectromechanical Systems, 2002. **11**(1): p. 12-19.10.1109/84.982858
7. Marchitto, A., et al., *Experiments on two-phase flow distribution inside parallel channels of compact heat exchangers.* International Journal of Multiphase Flow, 2008. **34**(2): p. 128-144.10.1016/j.ijmultiphaseflow.2007.08.005

8. Vist, S. and J. Pettersen, *Two-phase flow distribution in compact heat exchanger manifolds.* Experimental Thermal and Fluid Science, 2004. **28**(2-3): p. 209-215.10.1016/S0894-1777(03)00041-4

9. Wu, R., A. Kharaghani, and E. Tsotsas, *Two-phase flow with capillary valve effect in porous media.* Chemical Engineering Science, 2016. **139**: p. 241-248.10.1016/j.ces.2015.09.028

10. Parmar, R. and S.K. Majumder, *Microbubble generation and microbubble-aided transport process intensification-A state-of-the-art report.* Chemical Engineering and Processing, 2013. **64**: p. 79-97.10.1016/j.cep.2012.12.002

11. Sharan, M. and A.S. Popel, *A two-phase model for flow of blood in narrow tubes with increased effective viscosity near the wall.* Biorheology, 2001. **38**(5-6): p. 415-28, http://www.ncbi.nlm.nih.gov/pubmed/12016324

12. Chung, P.M.-Y., et al. *Two-Phase Flow Through Square and Circular Microchannels: Effect of Channel Geometry*. in *ASME/JSME 2003 4th Joint Fluids Summer Engineering Conference*. 2003. American Society of Mechanical Engineers.

13. Saisorn, S. and S. Wongwises, *The effects of channel diameter on flow pattern, void fraction and pressure drop of two-phase air-water flow in circular micro-channels.* Experimental Thermal and Fluid Science, 2010. **34**(4): p. 454-462.10.1016/j.expthermflusci.2009.02.006

14. Yue, J., G.W. Chen, and Q. Yuan, *Pressure drops of single and two-phase flows through T-type microchannel mixers.* Chemical Engineering Journal, 2004. **102**(1): p. 11-24.10.1016/j.cej.2004.02.001

15. Wu, J.S. and B.M. Yu, *A fractal resistance model for flow through porous media.* International Journal of Heat and Mass Transfer, 2007. **50**(19-20): p. 3925-3932.10.1016/j.ijheatmasstransfer.2007.02.009

16. Yu, J., X.J. Hu, and Y. Huang, *A modification of the bubble-point method to determine the pore-mouth size distribution of porous materials.* Separation and Purification Technology, 2010. **70**(3): p. 314-319.10.1016/j.seppur.2009.10.013

17. Rossen, W.R. and P.A. Gauglitz, *Percolation Theory of Creation and Mobilization of Foams in Porous-Media.* Aiche Journal, 1990. **36**(8): p. 1176-1188.DOI 10.1002/aic.690360807

18. Reeves, P.C. and M.A. Celia, *A functional relationship between capillary pressure, saturation, and interfacial area as revealed by a pore-scale network model.* Water Resources Research, 1996. **32**(8): p. 2345-2358.Doi 10.1029/96wr01105

19. Celia, M.A., P.C. Reeves, and L.A. Ferrand, *Recent Advances in Pore Scale Models for Multiphase Flow in Porous-Media.* Reviews of Geophysics, 1995. **33**(S2): p. 1049-1057.Doi 10.1029/95rg00248

20. Choi, C., D.I. Yu, and M. Kim, *Surface wettability effect on flow pattern and pressure drop in adiabatic two-phase flows in rectangular*

microchannels with T-junction mixer. Experimental Thermal and Fluid Science, 2011. **35**(6): p. 1086-1096.10.1016/j.expthermflusci.2011.03.003

21. Lee, C.Y. and S.Y. Lee, *Pressure drop of two-phase plug flow in round mini-channels: Influence of surface wettability.* Experimental Thermal and Fluid Science, 2008. **32**(8): p. 1716-1722.10.1016/j.expthermflusci.2008.06.007
22. Andrew, M., B. Bijeljic, and M.J. Blunt, *Pore-scale imaging of trapped supercritical carbon dioxide in sandstones and carbonates.* International Journal of Greenhouse Gas Control, 2014. **22**: p. 1-14.10.1016/j.ijggc.2013.12.018
23. Vizika, O., D.G. Avraam, and A.C. Payatakes, *On the Role of the Viscosity Ratio during Low-Capillary-Number Forced Imbibition in Porous-Media.* Journal of Colloid and Interface Science, 1994. **165**(2): p. 386-401.DOI 10.1006/jcis.1994.1243
24. Chakrabarti, D.R., G. Das, and S. Ray, *Pressure drop in liquid-liquid two phase horizontal flow: Experiment and prediction.* Chemical Engineering & Technology, 2005. **28**(9): p. 1003-1009.10.1002/ceat.200500143
25. McAdams, W.H., *Heat transmission*. third ed. 1954, New York: McGraw-Hill.

26. A. Cicchitti, C.L., M. Silvestri, G. Solddaini, R. Zavalluilli, *Two-phase cooling experiments–Pressure drop, heat transfer and burnout measurement.* Energia Nucl., 1960. **7**(6): p. 407-425,

27. Dukler, A.E., M. Wicks, and R.G. Cleveland, *Frictional pressure drop in two-phase flow: A. A comparison of existing correlations for pressure loss and holdup.* AIChE Journal, 1964. **10**(1): p. 38-43,

28. Beattie, D.R.H. and P.B. Whalley, *A simple two-phase frictional pressure drop calculation method.* International Journal of Multiphase Flow, 1982. **8**(1): p. 83-87,

29. Lin, S., et al., *Local Frictional Pressure-Drop during Vaporization of R-12 through Capillary Tubes.* International Journal of Multiphase Flow, 1991. **17**(1): p. 95-102.Doi 10.1016/0301-9322(91)90072-B

30. Awad, M.M. and Y.S. Muzychka, *Effective property models for homogeneous two-phase flows.* Experimental Thermal and Fluid Science, 2008. **33**(1): p. 106-113.10.1016/j.expthermflusci.2008.07.006

31. Chung, P.M.Y. and M. Kawaji, *The effect of channel diameter on adiabatic two-phase flow characteristics in microchannels.* International Journal of Multiphase Flow, 2004. **30**(7-8): p. 735-761.10.1016/j.ijmultiphaseflow.2004.05.002

32. M. Suo, P.G., *Two-phase flow in capillary tubes.* Journal of basic engineering 1964. **86**(1964): p. 576-582,

33. Metz, T., et al., *StarTube: a tube with reduced contact line for minimized gas bubble resistance.* Langmuir, 2008. **24**(17): p. 9204-6.10.1021/la801194j

Chapter 5 Effect of surface tension, viscosity, and pore geometry on the resistance to two-phase flows and on the effective pore throat[2]

5.1 Introduction

Resistance to two-phase flows is governed by pore morphology, size of the pore and its throat [1, 2]), pore surface wettability [3, 4], and fluid properties (e.g. viscosity and surface tension[5, 6]), etc. Pore and throats are regarded as the section or point with a minimal cross-sectional area in a flow path [7-9], and it can be evaluated directly through tomographic methods, e.g. micro-X-ray imaging and magnetic resonance imaging (MRI) [10-14]. The tomographic methods coupled with mercury injection porosimetry estimate the distribution of pore volume and pore size [12, 15] in reservoir or aquifer rocks. The data from mercury injection porosimetry is useful to describe the permeability of porous materials in a macroscopic sense. However, it is not helpful for understanding the impact of the topology and geometry of individual pore on the resistance to fluids, which is particularly important in improving the efficiency of processes and treatments for micro reactors, electronic chips and microbubble-aided drug delivery.

The effective pore throat was defined in Chapter 4 based on the pressure-drop

[2]Some contents of this chapter have been published in Chemical Engineering Science 197 (2019) 269–279

profiles of two-phase flows in constricted capillaries. In this chapter, the effect of surface tension, different gas and viscosity on the effective pore throat and the pressure drop was studied through adjusting the surface tension of the liquids. Silicone oils with similar surface tensions, but a large difference in viscosities, were employed to investigate the effect of fluid viscosity on the effective pore throat.

Table 5. 1 The value of each parameter in this chapter

u	2.36×10^{-5}- 0.0212 m/s	***Re***	1.41×10^{-5}- 2.3
Ca	2.79×10^{-7}- 8.81×10^{-3}	***We***	1.1×10^{-8}- 3.57×10^{-4}
Bo	1.41×10^{-3}- 0.0353		

5.2 Effect of gas phase on the effective pore throat and pressure drop for two-phase flows in constricted capillaries

The effect of different gases on the effective pore throat and the resistance to gas-liquid flows in constricted capillaries have been investigated. Air, CO_2 and CH_4 were chosen as these gases are very common in fuel cells, electronic devices, CO_2 storage, shale gas recovery and microbubble-aided drug delivery. The typical experimental data have been presented in Figs 5.1a-5.1d. All figures indicate that capillary resistance to the interfaces starts from the

effective pore throat. Under the same capillary tip diameter, a larger surface tension of gas-water interface suffers a higher resistance. The effective pore throat diameter is very similar for three types of gas-water flows due to the similar surface tensions of three gases (as shown in Figs. 5.2).

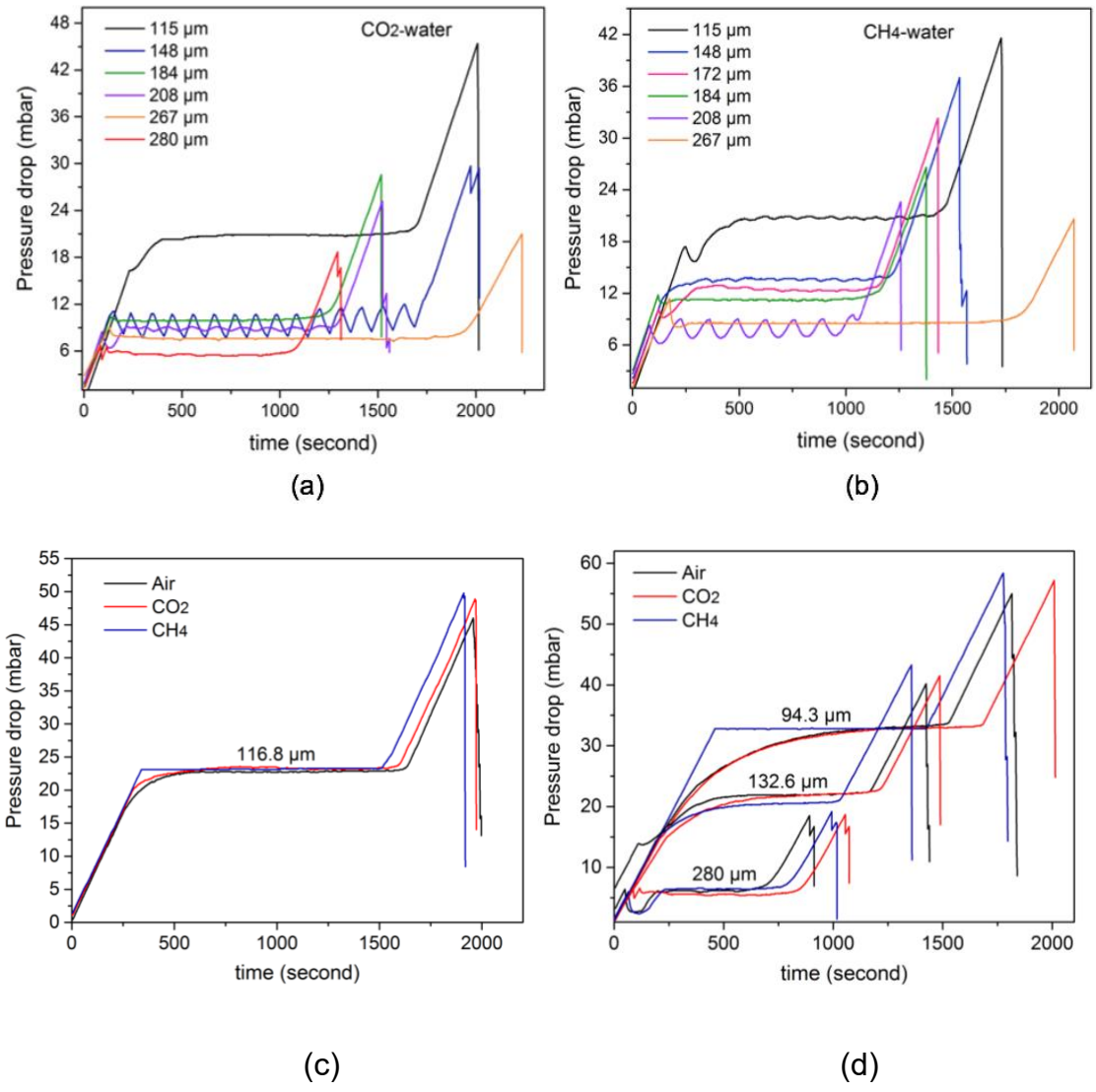

Fig. 5. 1 Pressure-drop profiles for (a) CO_2-water and (b) CH_4–water flows in constricted capillaries with tip diameters in the range from 115 to 280 μm; comparison of pressure drop profiles of three gas phase in the capillary with (c)

the tip diameter of 116.8 μm, and (d) the tip diameter of 94.3, 132.6 and 280 μm

The pressure profiles for three gas-water flows are very similar (Figs. 5.1a-5.1d), with a slight difference in magnitudes of pressure drop. For example, in the constricted capillary with a tip diameter of 116.8 μm (Fig. 5.1c), the CH_4-water interface has the highest pressure increase after the effective pore throat due to the greatest surface tension of CH_4-water (75.5 mN/m), while the air-water interface gives the lowest increase (lowest surface tension of air-water, 71.99 mN/m). Before the gas-water interface moves towards the effective pore throat, the pressure drop for the three type of gas-water flows is almost the same, as shown by the overlapping horizontal lines in Figs. 5.1c-5.1d.

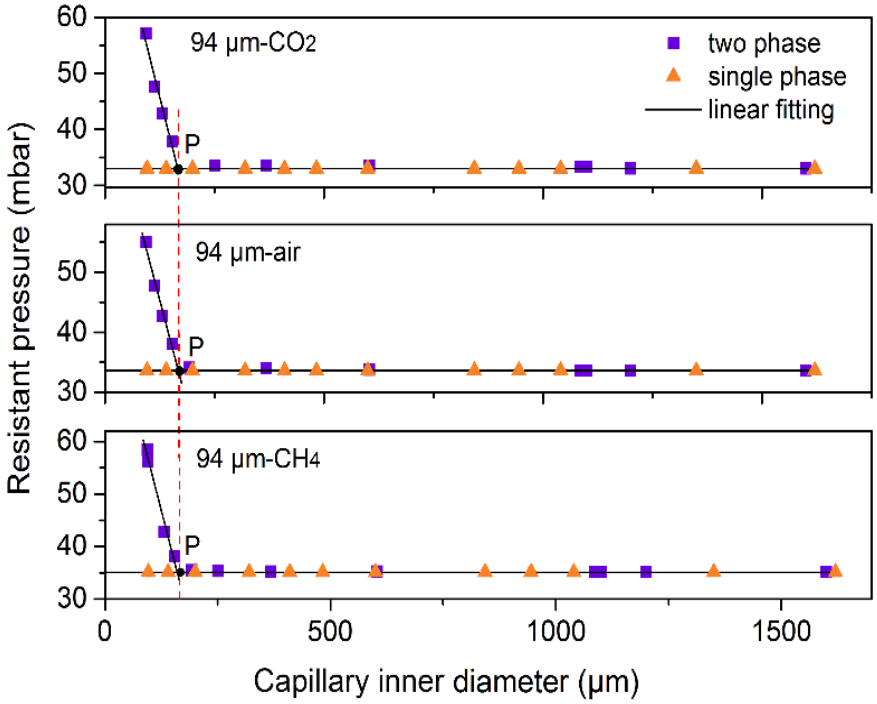

(a)

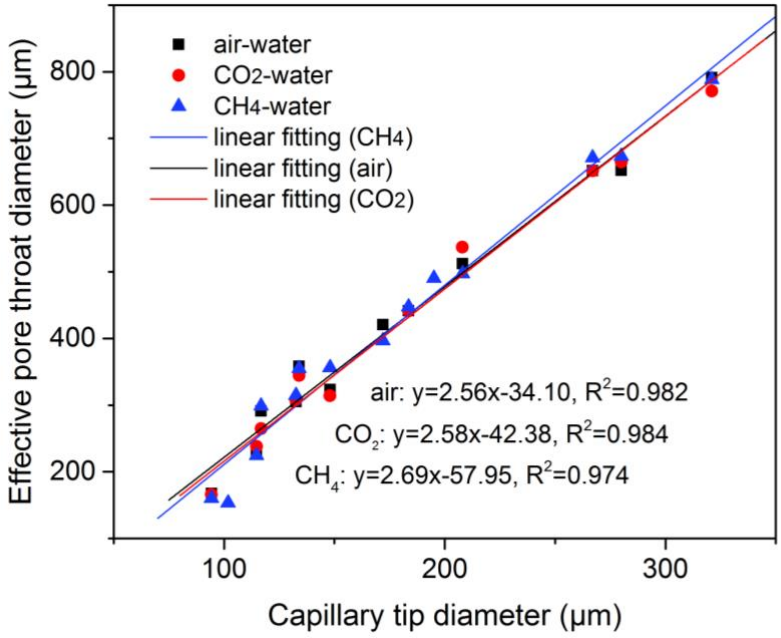

(b)

Fig. 5. 2 (a) Effective pore throat (*P* point) of the constricted capillaries for air-water, CO_2-water and CH_4-water flows, (b) the relationship of effective pore throat and the capillary tip diameter

5.3 Effect of liquid surface tension on effective pore throat

2-proponal was used to adjust the liquid surface tension from 71.99 to 30.57 mN/m. Fig. 5.3 shows the pressure-drop profiles for the flows of air-water, air-5%wt 2-propanol and air-20%wt 2-propanol in constricted capillaries. In Fig. 5.3(a), the horizontal lines are the balanced pressure for two-phase flows before the interfaces touch the effective pore throat. The balanced pressure for air-water, air-5%wt 2-propanol and air-20%wt 2-propanol were about 6.1, 7.2, and 10.1 mbar, respectively. Although the surface tension of air-20%wt 2-propanol is the lowest (30.57 mN/m), the balanced pressure to air-20%wt 2-propanol flow is the highest as the capillary tip diameter is the smallest (218.6 μm). The surface tension of air-water is the highest but the balanced pressure is the lowest because of the relatively large capillary tip diameter (224 μm). This indicates that when the pore diameter of microchannel is greater than the effective pore throat, the resistant pressure drop is directly dependent on the capillary tip sizes, rather than the surface tension. Fig. 5.3 (b) and (c) further prove the dominant effect of capillary tip size on the resistant pressure before the effective pore throat.

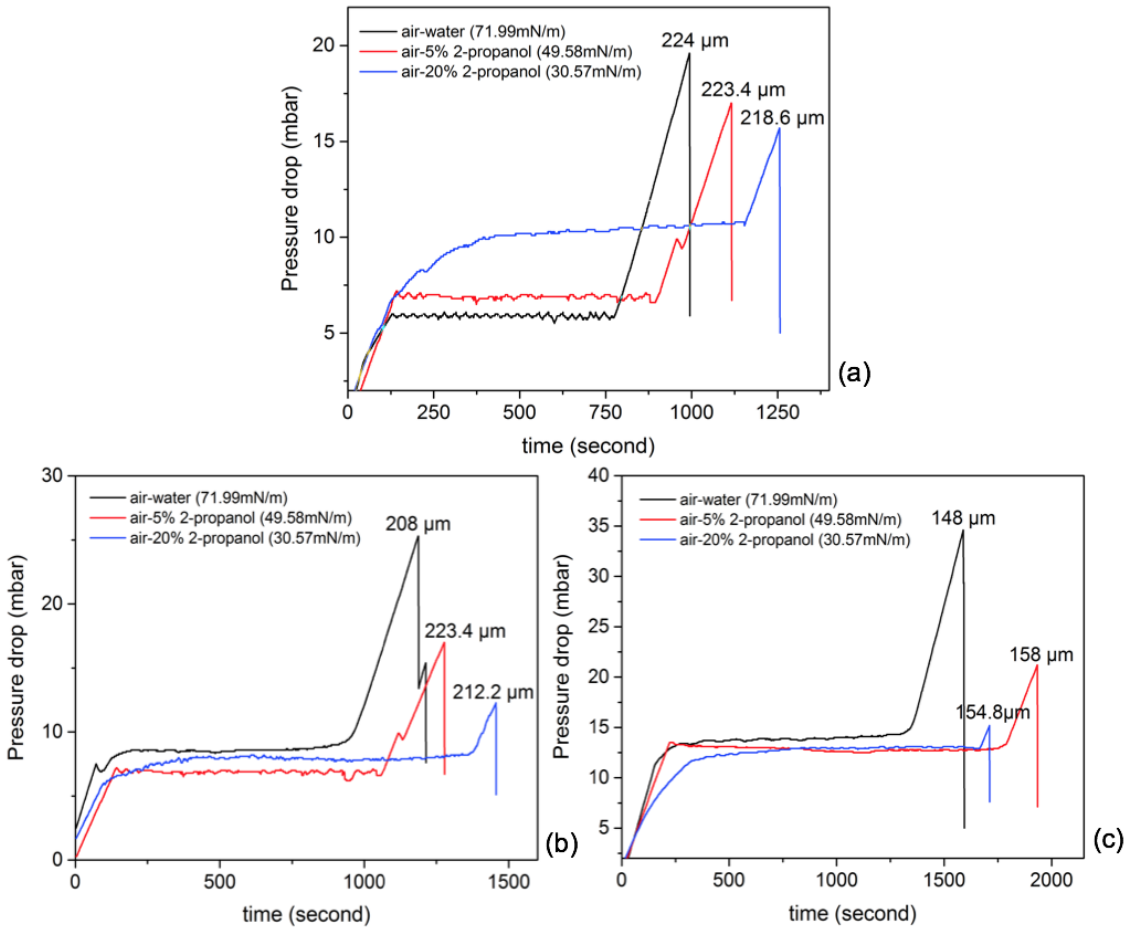

Fig. 5. 3 Effect of liquid surface tension and capillary tip diameter on the pressure-drop profiles of two-phase flow in constricted capillaries (The surface tensions: air-water = 71.99 mN/m, air-5%wt 2-propanol = 49.58 mN/m and air-20%wt 2-propanol = 30.57 mN/m)

The three fitted lines in Fig. 5.4 suggest that fluid surface tension affects the effective pore throat of constricted capillaries for two-phase flows. For the gas-liquid flows with a smaller surface tension, the effective pore throat diameter in the microchannel would be smaller. For example, in a capillary with a tip

diameter of 200 μm, the effective pore throat is the highest for air-water flow (around 480 μm, as shown in Fig. 5.4,) because of the highest surface tension of air-water interface (71.99 mN/m). On the contrary, the effective pore throat diameter for air-20%wt 2-propanol interface is the smallest (about 300 μm) among the three cases, as it has the lowest surface tension (39.57 mN/m). It is interesting to note that the gradients of three fitted lines are nearly the same. During the experiments, viscosity of DI water, 5%wt 2-propanol and 20%wt 2-propanol, and the capillary geometry were very similar, and the gas volume and liquid flowrate were the same. The same gradient of the lines in Fig. 5.4 indicates that the impact of the capillary tip size on the effective pore throat diameter is the same even though the air-liquid interfaces have various surface tensions.

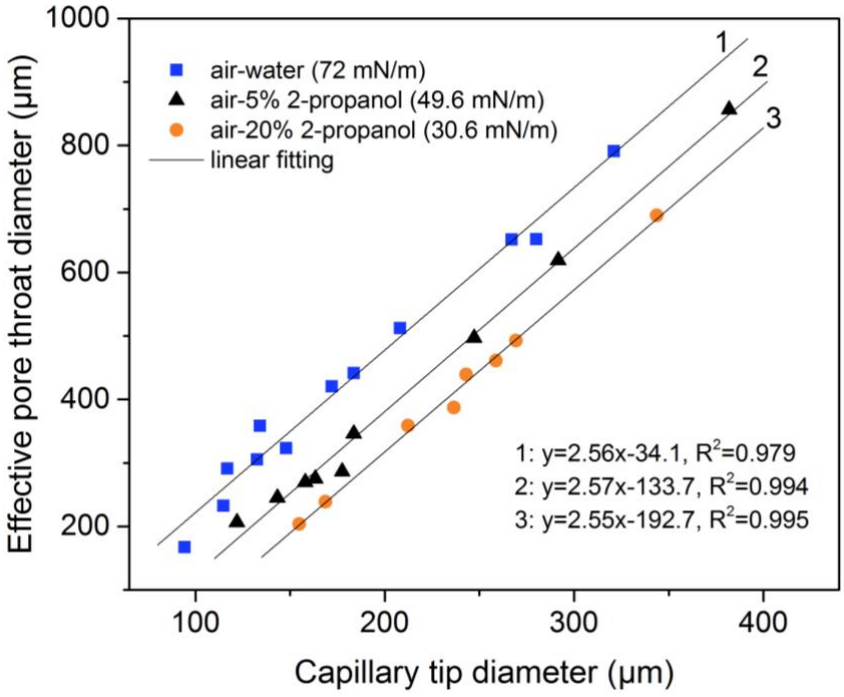

Fig. 5. 4 Effect of surface tension on the effective pore throat

5.4 Effect of liquid viscosity on the effective pore throat

The effect of viscosity on the effective pore throat was investigated through injecting silicone oil with viscosities from 10 to 500 cst to create a silicone oil-water flow in constricted capillaries. The experimental results are presented in Figs. 5.5, indicating that viscosity significantly affects the magnitude of the pressure drop in fluids flows (Fig. 5.5a), but does not affect the diameter of the effective pore throat (Fig. 5.5b). The resistant pressure drop of silicone oil flow in constricted capillaries increases with fluids viscosity. When the viscosity increases from 10 to 100 cst, the pressure drop for the silicone oil increases from 5 to 35 mbar in a constricted capillary with a tip diameter of 339 μm.

Fig. 5.5(b) shows the effect of viscosity (ranging from 10 to 500 cst) on the effective pore throat for silicone oil-water flows in constricted capillaries. The diameter of effective pore throat is similar even the viscosity of silicone oil varies significantly from 10 to 500 cst. The data indicates that the effective pore throat diameter is independent of fluid viscosity. Viscosity can affect the magnitude of resistance to phase body, but does not affect the resistance to the two-phase interface. A larger fluid viscosity will result in a higher frictional pressure drop, which is easily explained by Hagen-Poiseuille equation, thus the resistance to fluid body is greater. As the surface tension, rather than viscosities induces the resistance to the interface, viscosity does not influence the diameter of effective pore throat.

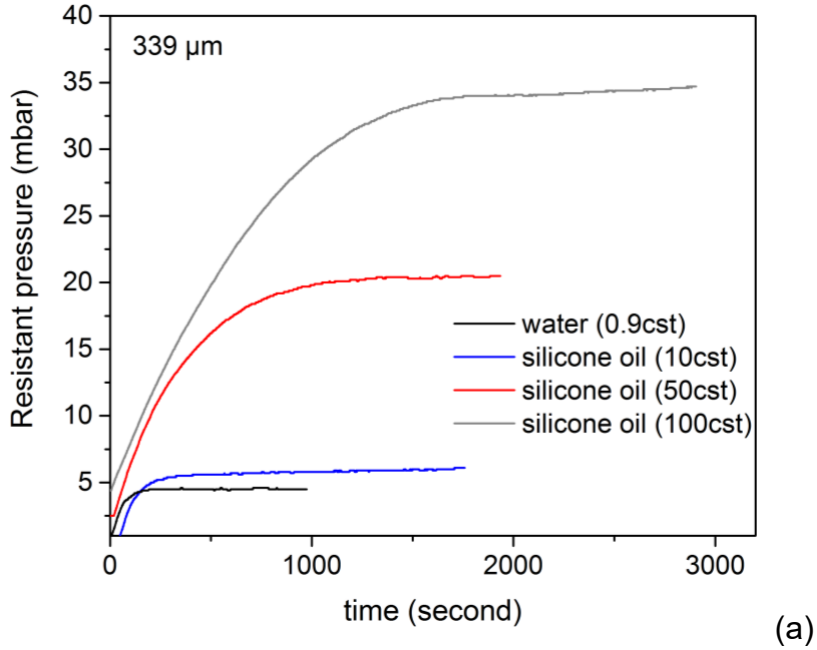

(a)

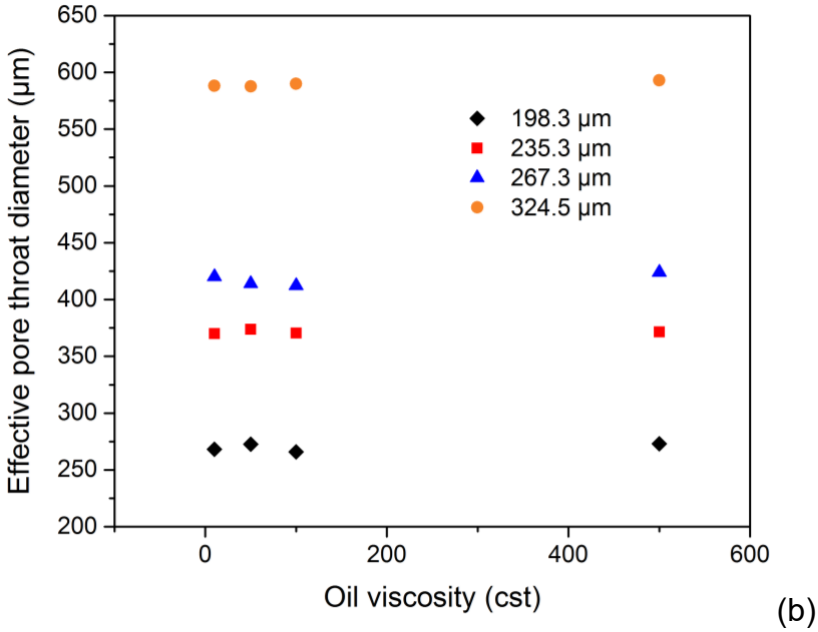

(b)

Fig. 5. 5 (a) Effect of viscosity on the pressure drop for silicone oil flows in a constricted capillary with a tip diameter of 339 μm; (b) effect of viscosity on effective pore throat for silicone oil-water interfaces with different viscosities

5.5 Effect of capillary geometry on the effective pore throat

In this study, the effect of capillary geometry on the effective pore throat is investigated in terms of the capillary length, capillary gradient and capillary tip diameter. Figs. 5.2 and 5.4 show that, within a certain range, the effective pore throat diameter linearly increases with the capillary tip diameter. For liquids with various surface tension, a large capillary tip diameter gives a large effective pore throat. As the capillary length is fixed in this study, the gradient of the capillary tapered section can be simply calculated by dividing the diameter difference at the two end of the capillary by the length. Fig. 5.6 illustrates the impact of capillary gradient on the diameter of effective pore throat diameter. Effective pore throat diameter almost linearly increases with the capillary gradient. Interestingly, the pressure increase rate does not show any obvious dependence on the capillary tip diameter or the capillary gradient. As shown in Fig. 5.1, the pressure increase sections in the pressure profiles have a similar increase rate for all gas-liquid flows in capillaries with diameters ranging from 94 to 291.6 μm.

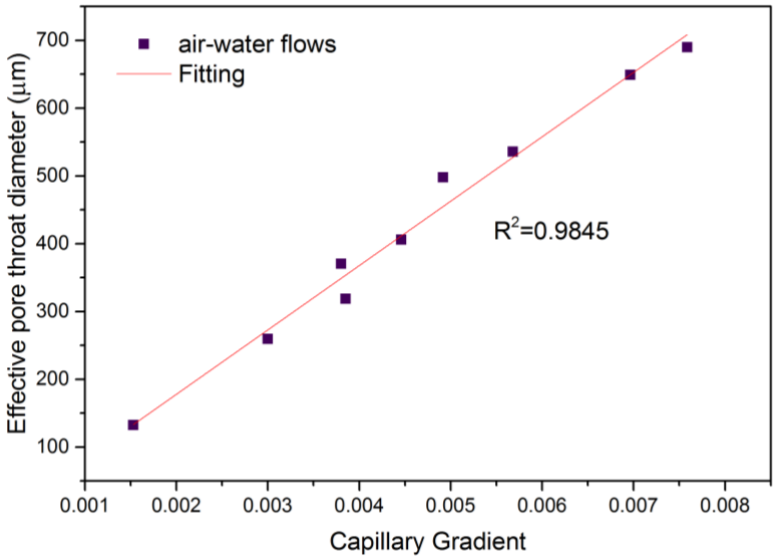

Fig. 5. 6 Effect of capillary gradient on the effective pore throat diameter in constricted capillaries

5.6 Discussion

As discussed in Chapter 4, the increase in the flow resistance is attributed to the capillary force induced by the bubble phase, while no theory explained this sudden increase as well as the effective pore throat. According to 'Jamin' effect and literature [16], the capillary pressure resulting from the motion of bubble in constricted microchannel equals the difference of capillary pressure between two sides of the bubble (as shown in Fig. 5.7) which can be calculated through equation (5-1).

$$\Delta P_c = P_B - P_A = \frac{2\gamma cos\theta_A}{r_A} - \frac{2\gamma cos\theta_B}{r_B} \quad (5\text{-}1)$$

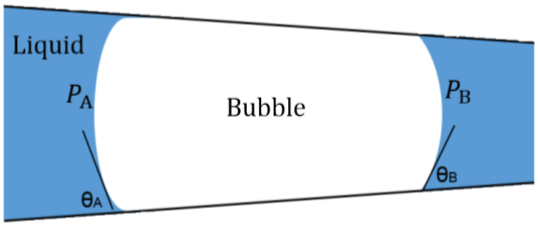

Fig. 5. 7 Schematic of the two sides of a bubble in a circular tapered capillary

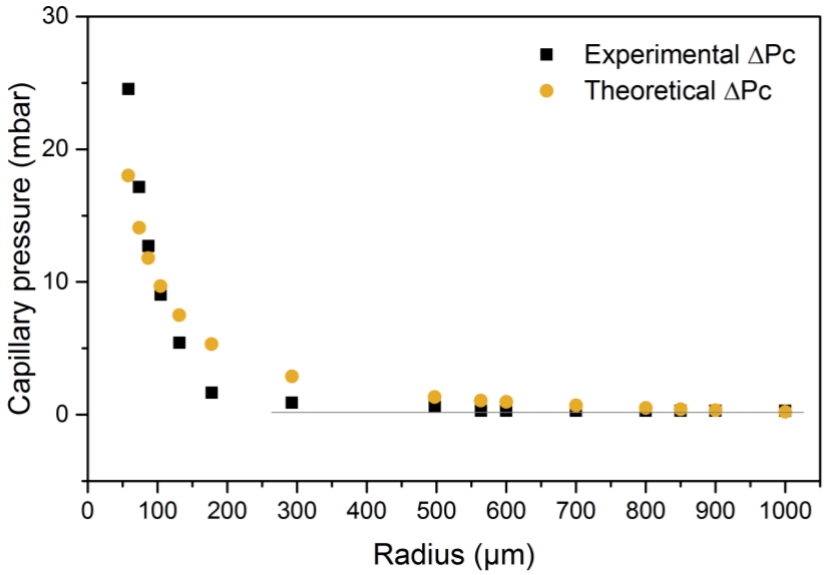

Fig. 5. 8 A plot of the change of capillary pressure with the flow path radius for air-water flow in the constricted capillary with the tip size of 94 μm

Fig. 5.8 compares the experimental capillary pressure and the theoretical capillary pressure for air-water flows in a constricted capillary, and it indicates that the capillary pressure calculated through equation (5-1) is smoothly and continuously changed with flow path radius under the condition that the contact angle and the surface tension are fixed. However, the experimental capillary

pressure is not smoothly changed with flow radius (as shown in Figs. 5.9-5.10), and the effective pore throat separates the capillary pressure profile into two straight lines with different gradients. When the channel pore diameter is greater than the effective pore throat, capillary pressure does not vary with the pore diameter. After the effective pore throat, capillary pressure suddenly increases with the decrease of pore diameter. The theoretical equations cannot indicate the size of effective pore throat and capillary pressure drop of fluid interface in constricted capillaries within a large range of pore diameter.

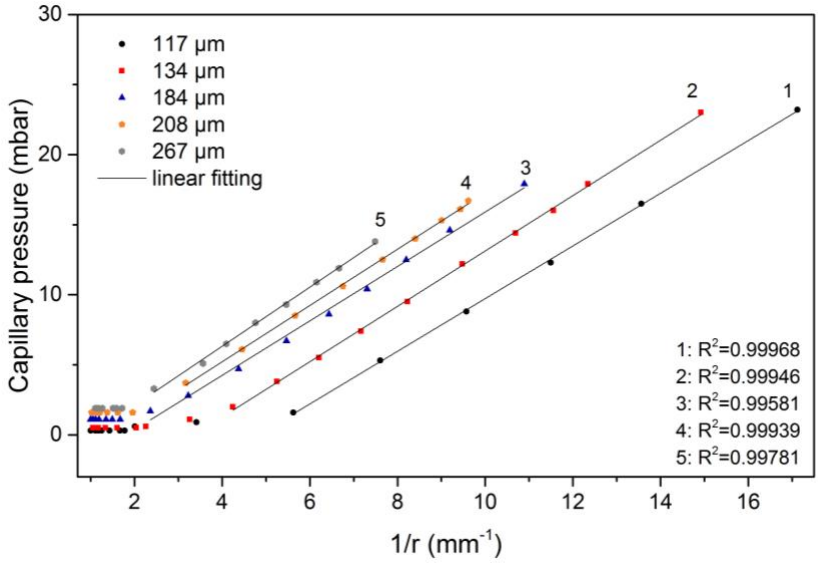

Fig. 5. 9 ΔP_c vs. *1/r* for air-water flows in constricted capillaries with different tip diameters

However, the effective pore throat and the sudden increase in the resistant pressure profiles could be qualitatively explained by the pore contact angle published by our group [17, 18]. Contact angle measured from a pore space

differs significantly from that on a flat surface. For a certain vapour-liquid interface and solid surface, the static contact angle on a flat surface is a constant. In a pore space, the static pore contact angle for air-water interface increases with the decrease of pore diameter until around 200-400 μm, and then takes a constant value of around 33 degrees (as shown in Fig. 5.10) [17]. When the pore diameter is greater than the effective pore throat, the pore contact angle increases with the decrease of pore diameter, i.e. $cos\theta$ decreases. The capillary pressure may remain constant in this section due to the decrease of $cos\theta$ and the decrease of r at the same time. Once the pore diameter is smaller than the effective pore throat, the pore contact angle is roughly a constant. The capillary pressure therefore linearly increases with $1/r$. The turning point in the contact angle profile roughly matches the effective pore throat.

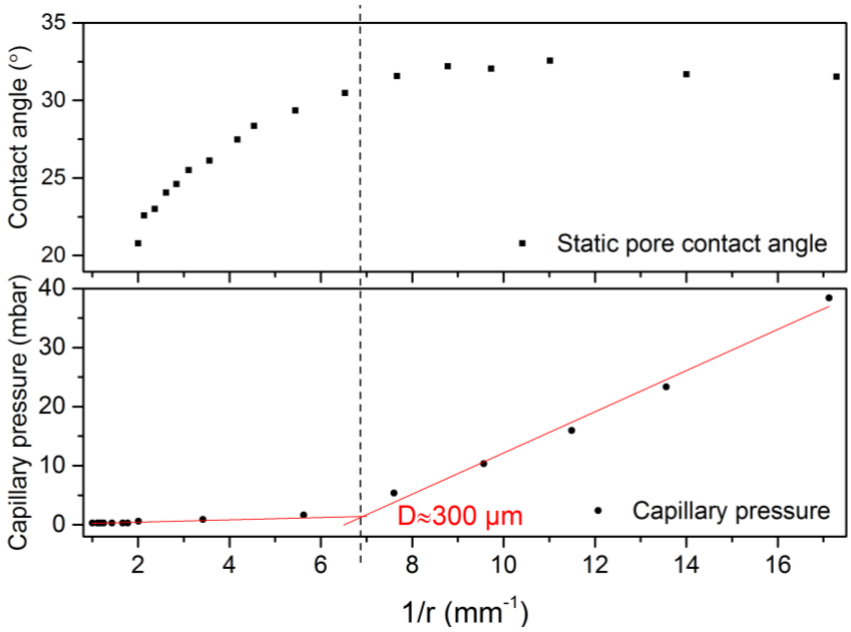

Fig. 5. 10 Change of static pore contact angle with *1/r*, and change of capillary pressure with *1/r* for the air-water flows in the constricted capillary with a tip size of 117 μm

From the aspect of the interfacial free energy, pore contact angle can also explain the measured pressure profile and the effective pore throat. For an isothermal, closed system, the interfacial free energy (dF) can be calculated through equation (5-2) [19], [20],

$$dF = \gamma_{sg} dA - \gamma_{sl} dA - \gamma_{lg} dA \cos\theta \quad (5\text{-}2)$$

Where γ is the interfacial tension for the liquid-gas (*lg*), solid-gas (*sg*) and solid-liquid (*sl*) interfaces, dA is the moving area of interface and θ is the equilibrium contact angle among the three-phase.

When the pore diameter is larger than the effective pore throat, the pore contact angle increases with the decrease of pore diameter, i.e. $cos\theta$ is decreasing. The interfacial free energy (dF) increases correspondingly, which means more energy is stored in the interface, therefore the energy dissipation which is reflected through pressure drop is not significant. This corresponds to the horizontal section of capillary pressure profile. When the channel pore diameter is smaller than the effective pore throat, the pore contact angle does not vary with pore diameter, and the two-phase interface cannot store extra energy, therefore the capillary pressure drop (ΔP_c) starts to increase sharply with the decrease of pore diameter.

5.7 Summary

The effect of the gas types, surface tension, fluids viscosity, capillary gradient and capillary tip diameter on the size of effective pore throat of a constricted microchannel has been investigated in this chapter. The results are as follows:

1. For air, CO_2 and CH_4 interface flows in constricted capillaries, capillary resistance to the interface starts from the effective pore throat. Under the same capillary tip diameter, a larger surface tension of gas-water interface suffers a higher resistance. The effective pore throat diameter is very similar for three types of gas-water flows due to the similar surface tensions of three gases.

2. The effect of surface tension on the pressure drop for two-phase flows takes effect only after the effective pore throat, and a larger surface tension gives a larger resistance in the constricted section of the capillary. For the flow path with a pore diameter greater than the effective pore throat, the pressure drop to the two-phase flows is mainly governed by the capillary tip size, rather than the surface tension. Small capillary tip gives a high resistance to two-phase flows. The diameter of the effective pore throat increases with the increase of interface surface tension under the same flow conditions (flowrate, liquid viscosities) and capillary tip size.
3. Viscosity significantly affects the magnitude of the pressure drop in fluids flows, but does not affect the diameter of the effective pore throat.
4. Within a certain range, the effective pore throat diameter linearly increases with the capillary tip diameter. Effective pore throat diameter almost linearly increases with the capillary gradient.

5.8 Reference

1. Sarma, H.K., B.B. Maini, and K. Jha, *Evaluation of emulsified solvent flooding for heavy oil recovery.* Journal of Canadian Petroleum Technology, 1998. **37**(7): p. 55-62.Doi 10.2118/98-07-06

2. Ramstad, T., et al., *Relative Permeability Calculations from Two-Phase Flow Simulations Directly on Digital Images of Porous Rocks.* Transport in Porous Media, 2012. **94**(2): p. 487-504.10.1007/s11242-011-9877-8

3. Reeves, P.C. and M.A. Celia, *A functional relationship between capillary pressure, saturation, and interfacial area as revealed by a pore-scale network model.* Water Resources Research, 1996. **32**(8): p. 2345-2358.Doi 10.1029/96wr01105

4. Choi, C., D.I. Yu, and M. Kim, *Surface wettability effect on flow pattern and pressure drop in adiabatic two-phase flows in rectangular microchannels with T-junction mixer.* Experimental Thermal and Fluid Science, 2011. **35**(6): p. 1086-1096.10.1016/j.expthermflusci.2011.03.003

5. Lin, S., et al., *Local Frictional Pressure-Drop during Vaporization of R-12 through Capillary Tubes.* International Journal of Multiphase Flow, 1991. **17**(1): p. 95-102.Doi 10.1016/0301-9322(91)90072-B

6. Lee, C.Y. and S.Y. Lee, *Pressure drop of two-phase plug flow in round mini-channels: Influence of surface wettability.* Experimental Thermal and Fluid Science, 2008. **32**(8): p. 1716-1722.10.1016/j.expthermflusci.2008.06.007

7. Olbricht, W.L., *Pore-scale prototypes of multiphase flow in porous media.* Annual Review of Fluid Mechanics, 1996. **28**(1): p. 187-213.DOI 10.1146/annurev.fl.28.010196.001155

8. Sahimi, M., *Characterization of Pore Space Connectivity: Percolation Theory*, in *Flow and Transport in Porous Media and Fractured Rock*. 2011, Wiley-VCH Verlag GmbH & Co. KGaA. p. 15-37.

9. Blunt, M.J., *Flow in porous media - pore-network models and multiphase flow.* Current Opinion in Colloid & Interface Science, 2001. **6**(3): p. 197-207.Doi 10.1016/S1359-0294(01)00084-X

10. Nelson, P.H., *Pore-throat sizes in sandstones, tight sandstones, and shales.* Aapg Bulletin, 2009. **93**(3): p. 329-340.10.1306/10240808059

11. Zou, C.N., et al., *Tight gas sandstone reservoirs in China: characteristics and recognition criteria.* Journal of Petroleum Science and Engineering, 2012. **88-89**: p. 82-91.10.1016/j.petrol.2012.02.001

12. Lindquist, W.B., et al., *Pore and throat size distributions measured from synchrotron X-ray tomographic images of Fontainebleau sandstones.* Journal of Geophysical Research-Solid Earth, 2000. **105**(B9): p. 21509-21527.Doi 10.1029/2000jb900208

13. Dong, H. and M.J. Blunt, *Pore-network extraction from micro-computerized-tomography images.* Phys. Rev. E., 2009. **80**(3 Pt 2): p. 036307.10.1103/PhysRevE.80.036307

14. Liu, Z., et al., *Pore-scale remaining oil distribution under different pore volume water injection based on CT technology.* Adv. Geo-Energ. Res., 2017. **1**(3): p. 171-181,

15. Nabawy, B.S., et al., *Pore-throat characterization in highly porous and permeable sandstones.* Aapg Bulletin, 2009. **93**(6): p. 719-739.10.1306/03160908131

16. Green, D.W. and G.P. Willhite, *Enhanced oil recovery*. Vol. 6. 1998: Henry L. Doherty Memorial Fund of AIME, Society of Petroleum Engineers Richardson, TX.

17. Li, X.X., X.F. Fan, and S. Brandani, *Difference in pore contact angle and the contact angle measured on a flat surface and in an open space.* Chemical Engineering Science, 2014. **117**: p. 137-145.10.1016/j.ces.2014.06.024

18. Li, X.X., et al., *An experimental study on dynamic pore wettability.* Chemical Engineering Science, 2013. **104**: p. 988-997.10.1016/j.ces.2013.10.026

19. Morrow, N.R., *Physics and Thermodynamics of Capillary Action in Porous Media.* Industrial and Engineering Chemistry, 1970. **62**(6): p. 32-56.Doi 10.1021/Ie50726a006

20. Andrade, J.D., L.M. Smith, and D.E. Gregonis, *The Contact Angle and Interface Energetics*, in *Surface and Interfacial Aspects of Biomedical Polymers: Volume 1 Surface Chemistry and Physics*, J.D. Andrade, Editor. 1985, Springer US: Boston, MA. p. 249-292.

Chapter 6 Resistance to lodged bubble and bubble dislodgment in complex capillary network[3]

6.1 Introduction

Understanding of bubble flows in porous media is of particular interest in enhanced oil recovery [1], intravascular gas embolism treatment[2, 3], fuel cells[4-6], and chemical reactors[7, 8] etc. For example, the infusion of bubbles into liquid can promote the mass or heat transfer in porous media, whereas bubbles may block the microchannel, thus disturb the performance and reduce the efficiency of the fluid transport and migration in microfluidics. In medical applications, embolotherapy a potential cancer treatment utilizes bubble lodgement to achieve the occlusion of the arteriole or capillary in targeted sites. The lodged bubbles block microvessel to restrict blood supply to tumors, and thus control the growth of tumor cells [2, 9-11]. A thorough understanding of resistance to lodged bubble in complex capillary network helps to precisely control bubble flow in blood vessels, and to improve the feasibility and efficiency of transport. It will help to answer the questions, such as where the bubble ultimately lodges, whether the bubble can be dislodged properly under a certain driving pressure, and the persistence time of microbubble lodged around the

[3] Some contents of this chapter have been published in Langmuir 2019, 35, 3194−3203

targeted sites[12].

Few studies were performed to investigate bubble dislodgment in complex capillary network. Works related to bubble flow behavior are mainly conducted in single straight channels [6, 12, 13], Y-type or U type channels [3, 14-16]. A single channel cannot simulate the flow conditions of bubble lodgement in complex capillary network. For example, when an elongated bubble lodges in a single cylindrical channel, it will be pushed by the driving force which is the pressure difference between the two ends of the bubble, as there is no other pathway for the liquid to move forwards. However, fluids in a network with multiple bifurcations have several paths to choose, and will consciously travel to the channel with a smaller resistance (without bubbles/with less bubbles). In this case, the bubble will be more difficult to dislodge. Capillary network with multi-bifurcation feature enables to demonstrate the effect of multichannel and bifurcations on the flow resistance and bubble dislodgment.

In this chapter, the capillary network is designed with smooth flowpath to closely mimic the structure of the physiological vascular networks[17], which is featured by multiple channels and bifurcations. The distribution of branching channel size nearly obeys the Murray's law, which is the basic principle for designing transfer networks. This chapter experimentally investigates the effect of channel complexity, diverging/converging angles, channel dimensions, and bubble length on the bubble flow resistance and bubble dislodging pressure in the capillary network. A theoretical model which further explains the underlying

physics of bubble dislodgement in a capillary network will be established in next chapter.

6.2 Effect of bubble length on the bubble dislodging pressure

The dislodging pressure is defined as the pressure required to remove a bubble from the lodged site of the microchannel or the microfluidic network. Bubble length is defined as the length measured from the bubble front to bubble back, as shown in Fig. 7.1 (a). The dislodging pressure profiles for bubbles with different lengths in the same channel of the capillary network were plotted in Figs. 6.1 and 6.2. The graphs clearly demonstrate that there is a critical bubble length (about 2 mm in this study). When the bubble length is less than the critical length, the dislodging pressure for smaller bubbles is greater than that for bubbles with a larger length in the same channel, and the dislodging pressure increases with the decrease of bubble length. Once the bubble length is greater than 2 mm, the dislodging pressure is almost constant and independent of the bubble length.

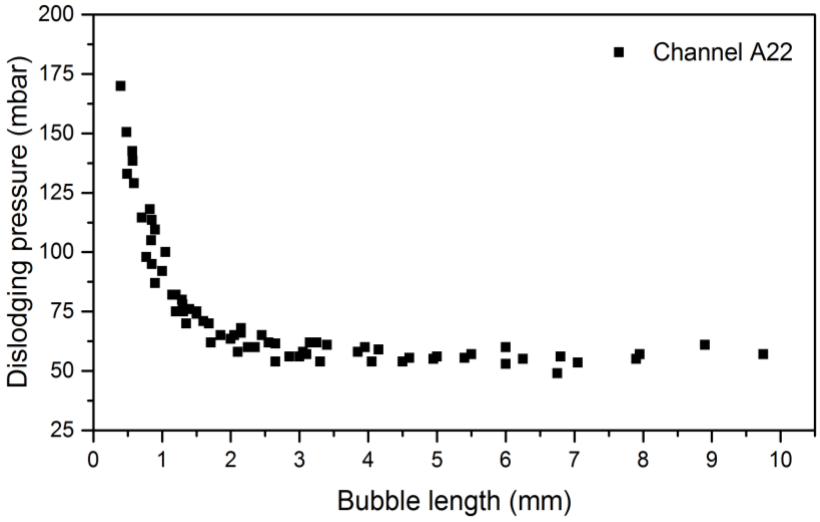

Fig. 6. 1 Dislodging pressure for bubbles with different lengths in channel A22

Fig. 6.1 shows bubble dislodging pressure profile in the channel A22 of network. The same trend has been observed in all other channels of the capillary network, but the magnitude of dislodging pressure varies significantly with channels. Taking a bubble with a length of 1 mm as an example, the dislodging pressure is about 92 mbar in channel A22, 32 mbar in channel A11, 47.5 mbar in channel A21, and 20 mbar in channel B11, as shown in Figs 6.1 and 6.2. The significant difference in the dislodging pressure is not only caused by the channel dimension, but also the network structure. This will be discussed in next section.

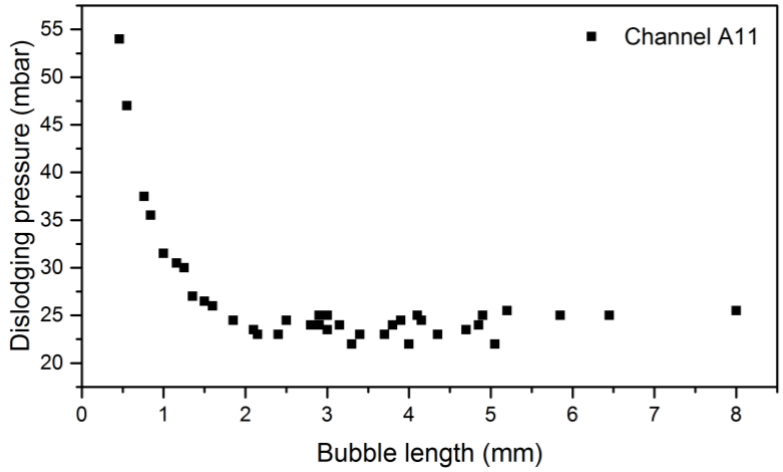

(a)

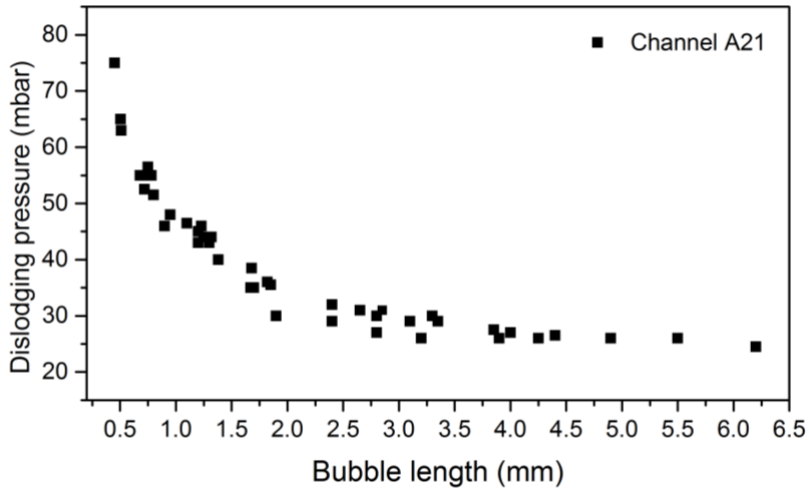

(b)

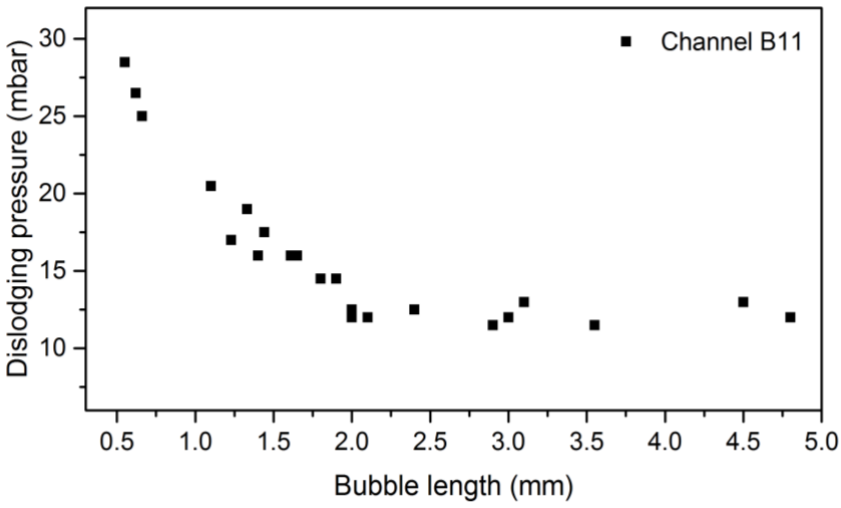

(c)

Fig. 6. 2 Dislodging pressure for bubbles with different lengths in channels (a) A11 (b) A21 and (c) B11

6.3 Effect of network structure and channel size on bubble dislodging pressure

The diverging/converging angles of bifurcations, channel dimension and the complexity of the flowpath affect the bubble dislodging pressure through affecting energy loss and fluid velocity. In this study, as $1<Re<10$, the inertia of the liquid cannot be neglected compared with viscous effect[18-20]. When the liquid flows through a channel with curvature, the liquid inertia will contribute to the velocity mismatch in the downstream direction between the liquid in the central and near-wall regions. The velocity mismatch causes the energy dissipation, and thus the liquid velocity will be smaller in the channel with a greater curvature under the same injection flowrate. The driving force which pushes the bubble to move is induced by liquid is proportional to the liquid velocity. For a bubble with same volume, the dislodging pressure provided externally by the network inlet will be higher in curved channels, in order to overcome the energy dissipation due to the liquid inertia induced by the curvature.

6.3.1 Network structure

The effect of network structure on the bubble dislodging pressure is discussed in terms of diverging/converging angle and complexity of flowpath. The

diverging angle of bifurcations is defined as the angle between the diverging fluid and the parent fluid velocity vector as illustrated in Figs. 6.3b, 6.4b and 6.6b. Converging angle is defined in similar way as shown in Fig. 6.3d.

Figs. 6.3-6.6 compare the dislodging pressure among different channels, and demonstrate how the impact of bubble length on the dislodging pressure varies with network structure. Through comparing the dislodging pressure profiles for different channels with similar size and flow condition, we found that the larger the diverging angle and/or converging angle, the higher the pressure is required to dislodge a bubble with the same length.

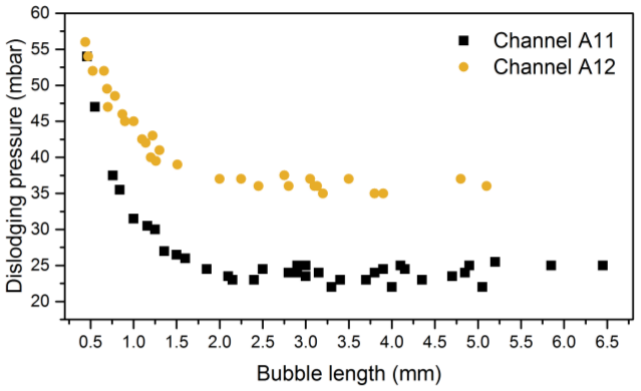

(a)

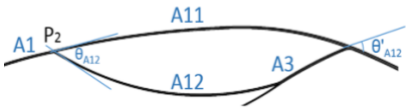

(b)

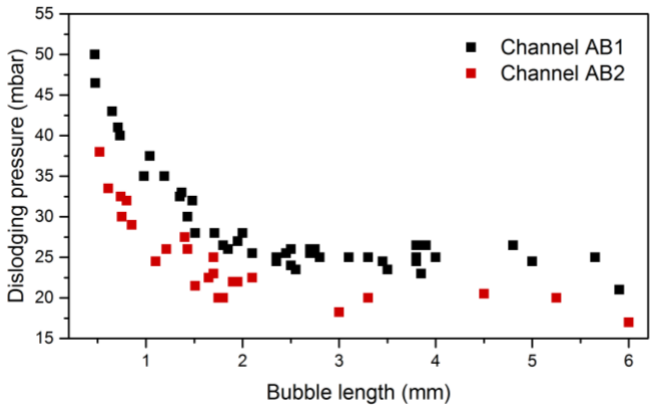

(c)

(d)

Fig. 6. 3 (a) Bubble dislodging pressure profiles in channels A11 (W≈0.46 mm) and A12 (W≈0.46 mm), (b) a schematic diagram of network structure around channels A11 and A12, (c) bubble dislodging pressure profiles in channels AB1 and AB2 (W≈0.45 mm, H≈0.32 mm), and (d) a schematic diagram of network structure around channels AB1 and AB2. θ_{A12} is the diverging angle of channel A12, θ'_{A12} is the converging angle of channel A12, and θ_{AB1} is the diverging angle of channel AB1.

For example, the bubble dislodging pressure in channel A12 is significantly higher than that in channel A11 as shown in Fig. 6.3a. Considering that channels A11 and A12 have similar size (W≈0.46 mm, H≈0.32 mm) and they share the same inlet (A1) and outlet (A4), the main difference between two channels is the diverging angle (θ_{A12}≈40.8º and θ_{A11}≈0º) and converging angle (θ'_{A12}≈48º and θ'_{A11}≈0º). Similarly, channels AB1 and AB2 have similar size (W≈0.45 mm, H≈0.32 mm), and they share the same inlet (channel AB), as shown in Fig. 6.3d. The dislodging pressure in channel AB1 is greater than that in channel AB2, and the diverging angle of channel AB1 (θ_{AB1}≈14.4º, θ_{AB2}≈0º) is slightly larger. The comparison of channels A11 and A12, channels AB1 and AB2 indicates that the diverging and converging angle may have effect on the bubble dislodging pressure in network.

Table 6. 1 Pressure difference across the single channel (ΔP_j is the predicted pressure across the single channel *j* where the bubble is lodged)

Bubble length (mm)	$\Delta \boldsymbol{P_{A11}}$ **(mbar)**	$\Delta \boldsymbol{P_{A12}}$ **(mbar)**	$\Delta \boldsymbol{P_{AB1}}$ **(mbar)**	$\Delta \boldsymbol{P_{AB2}}$ **(mbar)**
1.0	22.62	28.54	10.07	8.62
1.5	19.25	24.73	8.34	7.39
3.0	17.11	23.15	7.19	5.85

We employed the electric circuit analogy to predict the pressure drop across the single channel where the bubble lodges. The results are shown in Table 6.1, which indicates that ΔP_{A12} > ΔP_{A11} and ΔP_{AB1} > ΔP_{AB2} for dislodging bubbles with same lengths. The main difference between two sets of channels is the diverging angle (θ_{A12}≈40.8º> θ_{A11}≈0º and θ_{AB1}≈14.4º> θ_{AB2}≈0º) and converging angle (θ'_{A12}≈48º> θ'_{A11}≈0º). Therefore, the comparison of pressure across the single channels of A11 and A12, and channels of AB1 and AB2 demonstrated that the diverging angle and converging angle plays a non-negligible role in the bubble dislodging pressure in complex network.

Another factor affecting the bubble dislodging pressure is the complexity of flowpath. It is easy to understand that the fluid is prone to choose a relatively easier way with less flow resistance to travel under the same flow rate to avoid energy loss. For example, channel A22 (*W*=0.37 mm) and channel A21

(W=0.26 mm) have the same inlet (channel A2), and the diverging angle is similar ($\theta_{A21}\approx\theta_{A22}\approx7.8^{o}$), while the dislodging pressure in channel A22 is much higher than that in channel A21 as shown in Fig. 6.4a. This is mainly attributed to the network complexity, i.e. the existence of the channels AB, AB1 and AB2.

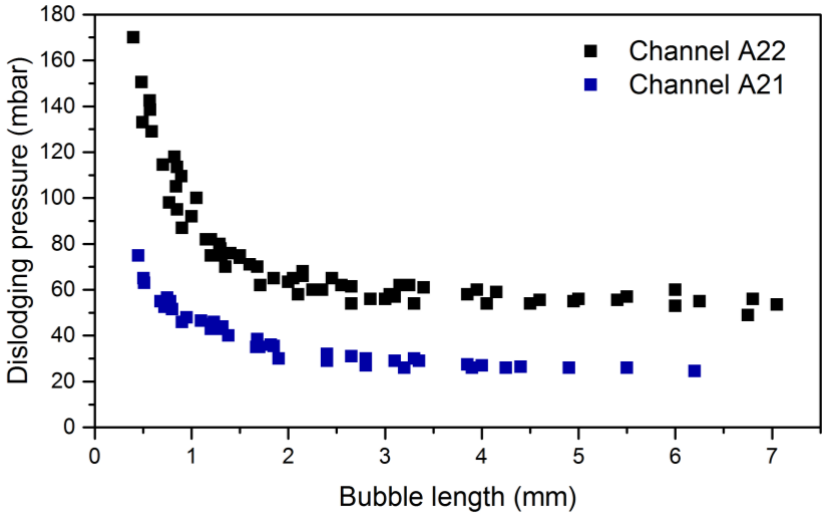

(a)

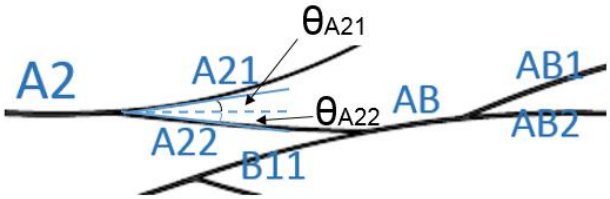

(b)

Fig. 6. 4 (a) Bubble dislodging pressure profiles in channels A21 and A22; (b) a schematic diagram of the network structure around channel A21 and A22 (θ_{A21} and θ_{A22} is the diverging angle of channel A21 and A22, respectively)

6.3.2 Channel size

In a single capillary, narrower channel will give a higher resistance to bubble

movement based on the reciprocal relationship between the channel diameter and pressure drop. However, this relationship may not be able to apply in complex capillary network with high interconnectivity, and the comprehensive effect induced by the complex structure and multichannel feature is required to be taken into account when analyzing the bubble dislodgement.

The effect of channel size in this capillary network is not obvious due to the effect of network structure. For example, channels A22 and B11 have the same width of about 0.36 mm, but the bubble dislodging pressure in channel A22 is significantly higher than that in channel B11 as shown in Fig. 6.5. Similar phenomenon has been discussed above in channels A11- A12 and channels AB1- AB2 (Fig. 6.3).

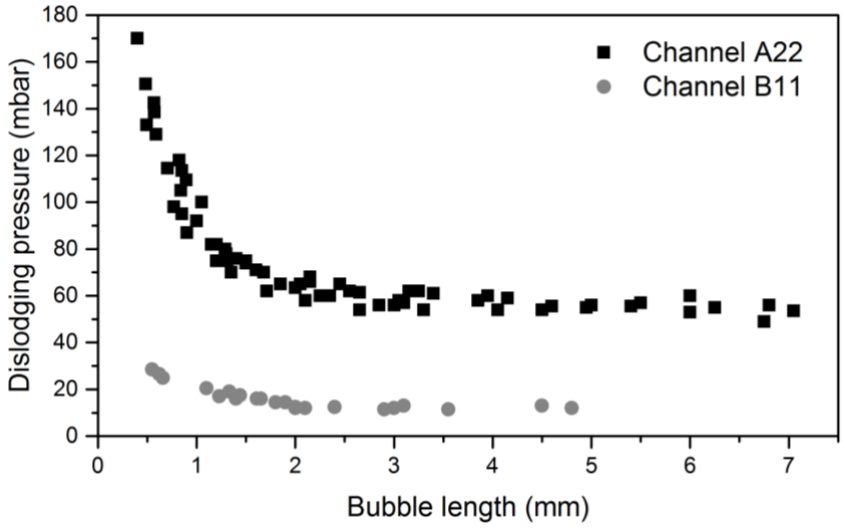

Fig. 6. 5 Bubble dislodging pressure profiles in channels B11 (W=0.36 mm) and A22 (W=0.37 mm)

The interplay between the impact of network structure and the impact of

channel size on the dislodging pressure varies with the bubble length. Taking channels A21 (W=0.26 mm) and A12 (W=0.46 mm) as an example, they have the same converged channel (A3), but different inlet channels. Theoretically, the narrower channel (channel A21) should provide a higher resistance to bubble movement. However, as shown in Fig. 6.6a, when bubble length is larger than around 1.5 mm, the dislodging pressure in channel A12 (wider) is higher than that in channel A21 (narrower). It suggests that for large bubbles, network structure, rather than the channel width dominates the bubble dislodging pressure in capillary networks. The fluid originated from P1 has the same velocity, and energy dissipated by passing the pathway (from P1 to channel A12) is much higher than passing the pathway (from P1 to channel A21) due to the high diverging angle in P2 (θ_{A12}≈40.8º and θ_{A21}=7.8º), as shown in Fig. 6.6b.

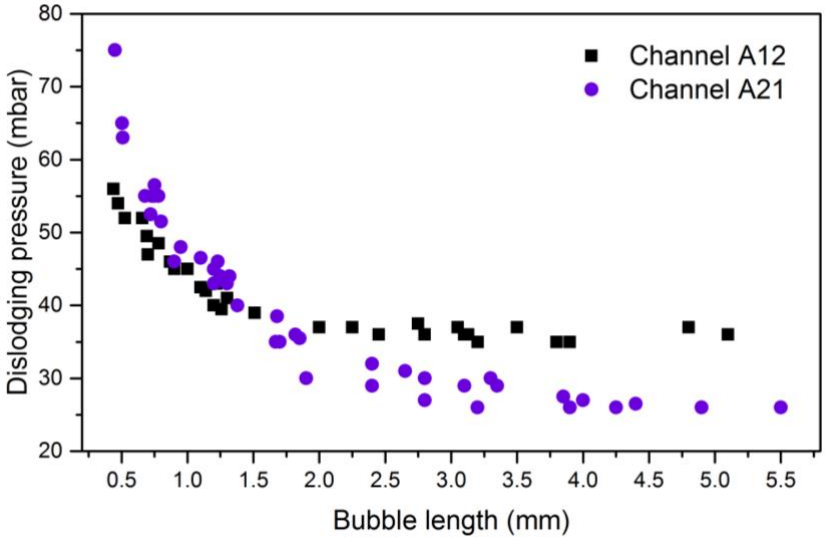

(a)

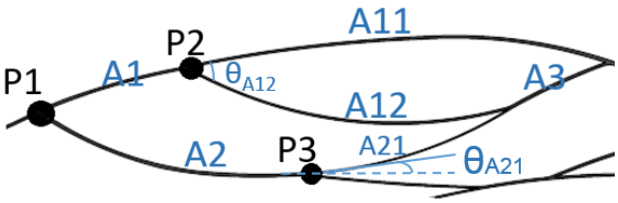

(b)

Fig. 6. 6 (a) Bubble dislodging pressure profiles in channels A12 (*W*=0.46 mm) and A21 (*W*=0.26 mm); (b) a schematic diagram of the network structure around channels A12 and A21, and θ_{A21} is the diverging angle of channel A21, θ_{A12} is the diverging angle of channel A12

For bubbles with the length less than 1.5 mm, the dislodging pressure for bubbles with a similar length in channel A21 (narrower) is higher than that in channel A12 (wider), which is opposite to the dislodging pressure profile for bubbles with a length greater than 1.5 mm. The pressure increase rate in channel A21 is larger than that in channel A12. For example, when the bubble length decreases from 3.1 mm to 0.5 mm, the dislodging pressure increases from 37.5 mbar to 55 mbar in channel A12, and from 28.5 mbar to 75 mbar in channel A21. This indicates that the channel width significantly influences the dislodging pressure increase rate when the bubble length is less than 1.5 mm. Narrower channels will be more sensitive to the variation of bubble length. Further explanation of these phenomena based on our proposed model has been detailed in next chapter.

6.4 Summary

In this chapter, the pressure required to dislodge a bubble from the complex capillary network has been investigated in terms of the bubble length, channel sizes and network structures.

1. When the bubble length is less than the critical length, the dislodging pressure is increased with the decrease of bubble length. Once the bubble length is greater than this critical length (2 mm in this study), the dislodging pressure is almost constant and independent of the bubble length.

2. For the channels with similar size and flow condition, we found that the larger the diverging angle and/or converging angle, the higher the pressure is required to dislodge a bubble with the same length.

3. The reciprocal relationship between the channel diameter and pressure drop may not apply in complex capillary network with high interconnectivity, and the comprehensive effect induced by the complex structure and multichannel features is required to be taken into account when analyzing the bubble dislodgement.

6.5 Reference

1. Farajzadeh, R., et al., *Foam-oil interaction in porous media: Implications for foam assisted enhanced oil recovery.* Advances in Colloid and Interface Science, 2012. **183**: p. 1-13.10.1016/j.cis.2012.07.002
2. Bull, J.L., *Cardiovascular bubble dynamics.* Crit. Rev. Biomed. Eng., 2005. **33**(4): p. 299-346, http://www.ncbi.nlm.nih.gov/pubmed/15982185
3. Valassis, D.T., et al., *Microbubble transport through a bifurcating vessel network with pulsatile flow.* Biomed Microdevices, 2012. **14**(1): p. 131-43.10.1007/s10544-011-9591-x
4. Yang, H., T.S. Zhao, and Q. Ye, *In situ visualization study of CO2 gas bubble behavior in DMFC anode flow fields.* Journal of Power Sources, 2005. **139**(1-2): p. 79-90.10.1016/j.jpowsour.2004.05.033
5. Calabriso, A., et al., *Bubbly flow mapping in the anode channel of a direct methanol fuel cell via PIV investigation.* Applied Energy, 2017. **185**: p. 1245-1255.10.1016/j.apenergy.2016.01.042
6. Steinbrenner, J.E., et al., *Impact of channel geometry on two-phase flow in fuel cell microchannels.* Journal of Power Sources, 2011. **196**(11): p. 5012-5020.10.1016/j.jpowsour.2011.02.032
7. Chen, X.Y., et al., *Numerical studies on different two-dimensional micromixers basing on a fractal-like tree network.* Microsystem Technologies-Micro-and Nanosystems-Information Storage and

Processing Systems, 2017. **23**(3): p. 755-763.10.1007/s00542-015-2742-x

8. Yue, J., G.W. Chen, and Q. Yuan, *Pressure drops of single and two-phase flows through T-type microchannel mixers.* Chemical Engineering Journal, 2004. **102**(1): p. 11-24.10.1016/j.cej.2004.02.001
9. Boehm, T., et al., *Antiangiogenic therapy of experimental cancer does not induce acquired drug resistance.* Nature, 1997. **390**(6658): p. 404,
10. Bull, J.L., *The application of microbubbles for targeted drug delivery.* Expert Opin. Drug Deliv., 2007. **4**(5): p. 475-93.10.1517/17425247.4.5.475
11. Samuel, S., et al., *In vivo microscopy of targeted vessel occlusion employing acoustic droplet vaporization.* Microcirculation, 2012. **19**(6): p. 501-9.10.1111/j.1549-8719.2012.00176.x
12. Suzuki, A. and D.M. Eckmann, *Embolism bubble adhesion force in excised perfused microvessels.* Anesthesiology, 2003. **99**(2): p. 400-8, http://www.ncbi.nlm.nih.gov/pubmed/12883413
13. Mohammadi, M. and K.V. Sharp, *The Role of Contact Line (Pinning) Forces on Bubble Blockage in Microchannels.* J Fluids Eng, 2015. **137**(3): p. 0312081-312087.10.1115/1.4029033
14. Calderon, A.J., et al., *A boundary element model of the transport of a semi-infinite bubble through a microvessel bifurcation.* Phys. Fluids 2010. **22**(6): p. 61902.10.1063/1.3442829

15. Calderón, A.J., J.B. Fowlkes, and J.L. Bull, *Bubble splitting in bifurcating tubes: a model study of cardiovascular gas emboli transport.* J. Appl. Physiol., 2005. **99**(2): p. 479-487,

16. Carlson, A., M. Do-Quang, and G. Amberg, *Droplet dynamics in a bifurcating channel.* International Journal of Multiphase Flow, 2010. **36**(5): p. 397-405.10.1016/j.ijmultiphaseflow.2010.01.002

17. Chen, Y.P. and Z.L. Deng, *Gas flow in micro tree-shaped hierarchical network.* International Journal of Heat and Mass Transfer, 2015. **80**: p. 163-169.10.1016/j.ijheatmasstransfer.2014.09.016

18. Debus, J.D., et al., *Energy dissipation in flows through curved spaces.* Scientific Reports, 2017. **7**: p. 42350.10.1038/srep42350

19. Zhang, J., et al., *Fundamentals and applications of inertial microfluidics: a review.* Lab Chip, 2016. **16**(1): p. 10-34.10.1039/c5lc01159k

20. Di Carlo, D., *Inertial microfluidics.* Lab Chip, 2009. **9**(21): p. 3038-46.10.1039/b912547g

Chapter 7 Effect of network structure on the bubble dislodgment and pressure distribution in microfluidic networks[4]

7.1 Introduction

Microfluidic networks have been frequently used to mimic human arterioles, airways in the lung[1], water distribution networks[2], solar panels, the cooling of electronics[3], etc. There are many advantages in microfluidics, such as lower hardware cost and reagents consumption, shorter response time[4, 5], higher mixing efficiency and lower thermal resistance[6], whereas, these are achieved at the expense of increased pressure drop which may be induced by the parallel or serpentine microchannels. However, in most microfluidic systems, bubble/particle accumulation is a frequent obstacle which considerably influences the system performance. Bubble/particle accumulation is difficult to avoid, especially around bifurcation regions in microfluidics [7, 8]. Therefore, investigations about fluids (gas or/and liquids) flows through a single symmetric or an asymmetric bifurcation, and multiple bifurcations in series[9, 10] have been conducted experimentally and numerically[11, 12].

Bubble lodgement and dislodgment in a confined microfluidic network is affected by a variety of factors, including liquid flow rate, gravity, bubble length

[4] Some contents of this chapter have been published in Chemical Engineering Science.

(size) surface wettability, and network/channel geometry [13-15]. To avoid the bubble lodgment or to detach the lodged bubble, many literature have studied the particle/bubble adhesion and suspension in single channels [13, 14, 16, 17] or networks with very simple structure [18]. To the author's best knowledge, very few investigation addressed on the effect of network complexity on bubble dislodgment in microfluidic networks. In this chapter, the impact of network complexity on the bubble dislodgment, and the distribution of overall pressure on the individual channel have been investigated experimentally and theoretically. The effect of network structure on the bubble dislodging pressure is experimentally investigated in terms of the bifurcating angles, bubble position and proximal channels. A theoretical model has been established to illustrate the underlying physics of bubble dislodgement in a capillary network, and to specify the relationship between bubble length and dislodging pressure. The effects of surface tension, viscosity, surface roughness, contact angle and thin film deposition have also been considered in the model. In the modelling, a parameter c_j introduced in the model aims to characterize the distribution of the overall pressure in each microchannel.

7.2 Theoretical modelling

A theoretical model is proposed to describe the behavior of bubble dislodgement from a microchannel with rectangular cross-section in complex capillary network in this chapter[15]. Considering the moment when the motion

of the bubble is initiated, a bubble slug as shown in Fig. 7.1 is selected for following discussion.

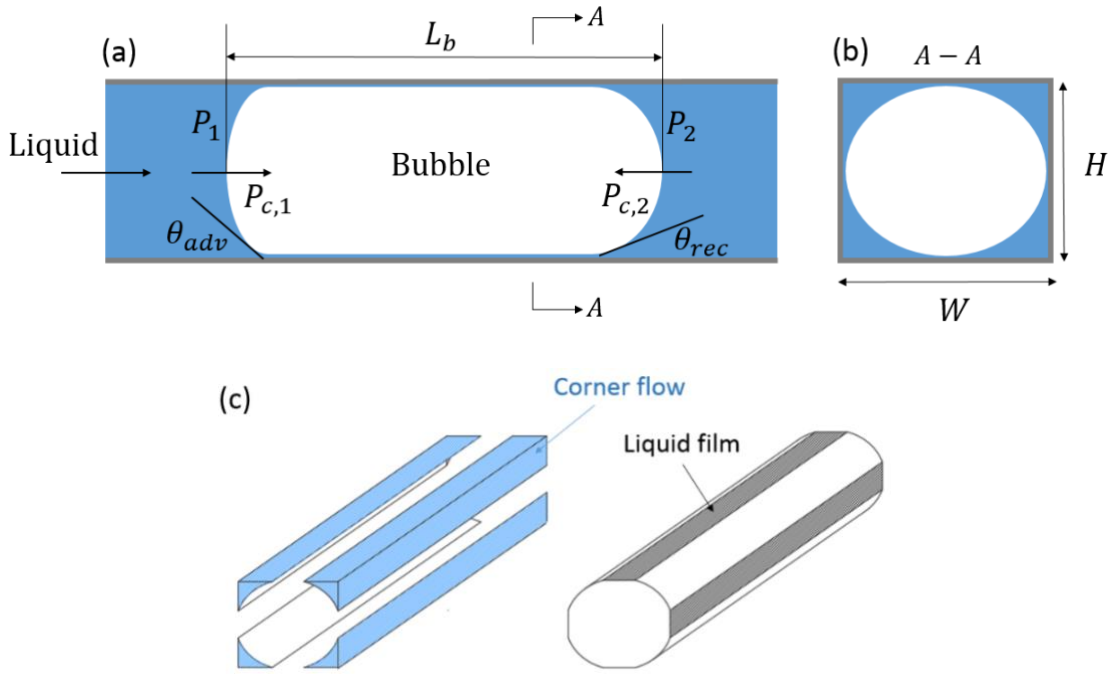

Fig. 7. 1 (a) A schematic diagram of a bubble slug in its static state in a microchannel of the capillary network, (b) a cross-sectional view of the gas/liquid distribution across the channel, and (c) a schematic diagram of the bubble flow through a microchannel in which liquid flows past the bubble through the corner. Blue section represents the liquid phase, and white section is the gas phase.

We assume that the pressure drop through the bubble slug is equal to the pressure difference between the pressure in bubble left end (P_1) and pressure in bubble right end (P_2), i.e.,

$$\Delta P_{bubble} = P_1 - P_2 \qquad (7\text{-}1)$$

By applying a driving pressure to the bubble, the shape of the bubble will be deformed first to against the driving force, thus the induced difference between the left and right curvatures will cause the capillary pressure drop[19, 20]. The frictional force exists between the liquid film and the bubble phase, acting as another resistant force for bubble moving[21]. The resistant pressure drop for the bubble movement (ΔP_{bubble}) is the sum of the frictional pressure drop (ΔP_f) and the capillary pressure drop (ΔP_c), i.e.,

$$\Delta P_{bubble} = \Delta P_f + \Delta P_c \quad (7\text{-}2)$$

The capillary pressure drop is calculated by equation (2-15) for rectangular channels. The frictional pressure drop caused by the liquid film can be calculated based on the Darcy-Weisbach equation which shows a good prediction in several previous studies [22-25]. In the bubble slug unit, the frictional pressure drop ΔP_f can be written based on equation (2-15) [25-27] as,

$$\Delta P_f = 2\rho_l f_f u_b^2 \frac{l_b}{H_j} \quad (7\text{-}3)$$

where ρ_l is the density of DI water, u_b is the mean superficial velocity of bubble, l_b is the length of bubble slug and H_j is the height of the corresponding microchannel.

The driving pressure around the bubble is maintained by the corner flow, as the corner liquid (the blue section, as depicted in Figs. 8b and 8c) drags the bubble to move. The pressure drop for the corner flow is equal to the driving pressure exerting on the bubble, which was also assumed by Wong et al. and Mohammadi[19, 20]. As the liquid flowing across the corner can be treated as

Poiseuille flow, the pressure drop for the corner flow can be approximately calculated based on Poiseuille law, gives as,

$$P_1 - P_2 = \frac{128\mu_l l_b Q_f}{\pi D_{eff}^4} \quad (7\text{-}4)$$

where μ_l is the viscosity of DI water, Q_f is volumetric flow rate and D_{eff} is the effective dynamic diameter of the liquid flow in corners which can be assumed as a constant for each microchannel in this study.

In capillary networks, the volumetric flow rate Q_f is the function of the pressure difference between inlet and outlet of the microchannel (ΔP_j), and can be expressed according to the Darcy's law[28],

$$Q_f = -\frac{KK_{r,f}A}{\mu_l}\frac{\partial p}{\partial x} = \frac{KK_{r,f}A_j}{\mu_l}\frac{\Delta P_j}{L_j} \quad (7\text{-}5)$$

$$\Delta P_j = c_j * \Delta P \text{ or } c_j = \Delta P_j/\Delta P \quad (7\text{-}6)$$

Where *K* is the absolute permeability of the microchannel, $K_{r,f}$ is the relative permeability of fluid, *A* is the sectional area of the microchannel, *L* is the length of the microchannel, ΔP_j is the pressure drop in microchannel *j*, ΔP is the overall pressure difference between the inlet and outlet of the capillary network.

Parameter c_j, a pressure loss factor of the corresponding microchannel *j*, is defined to characterize the pressure loss caused by network structures (such as multi-channel, multi-bifurcation, bifurcating angles), gives as equation (7-6). It can be seen as the contribution of the dislodging pressure in the individual channel *j* to the whole network.

Combining equations (7-1) - (7-6), the pressure difference required to initiate

the movement of lodged bubble can be expressed as,

$$\Delta P = \frac{\pi D_{eff}^4 L_j}{64KK_{r,f}W_jH_jc_j}\left[\frac{\sigma(\frac{1}{W_j}+\frac{1}{H_j})(\cos\theta_{rec}-\cos\theta_{adv})}{l_b}+\frac{\rho_l f_f u_b^2}{H_j}\right] \quad (7\text{-}7)$$

The relative permeability $K_{r,f}$ is related to the void fraction (the fraction of the channel cross-sectional area that is occupied by the bubble, as shown in Fig. 7-1b), and it can be approximately taken as an invariable. The difference in the cosine of the receding and advancing angle changes in a small range, which can be roughly neglected.

The equation (7-7) can be written as a simple form,

$$\Delta P = \frac{MA_j}{l_b} + NB_j \quad (7\text{-}8)$$

in which, $A_j = \frac{L_j}{W_jH_jc_j}\left(\frac{1}{W_j}+\frac{1}{H_j}\right)$, $B_j = \frac{L_j}{W_jH_j^2c_j}$ (7-9)

$$M = \frac{\sigma\pi D_{eff}^4}{64KK_{r,f}}(\cos\theta_{rec}-\cos\theta_{adv}),\ N = \frac{\pi D_{eff}^4\rho_l f_f u_b^2}{64KK_{r,f}} \quad (7\text{-}10)$$

where A_j and B_j are the parameters related to the corresponding microchannel, and *M* and *N* are constant for the same microchannel.

7.3 Analysis of experimental results through theoretical modelling in complex network A

The model proposed in equation (7-7) fully describes the factors affecting dislodging pressure for single bubble in a capillary network with multi-channel and multi-bifurcation. It closely relates to the channel dimension (width, length and height), bubble length, fluid flow rate, contact angle, and network structure.

This model demonstrates that the dislodging pressure is dependent on the bubble length (l_b) in a complex capillary network. For bubbles with small lengths, the dislodging pressure increases significantly with the decrease of bubble length, i.e. smaller bubble will require higher pressure to dislodge. When the bubble length is longer than a certain value, the dislodging pressure is nearly equal to a constant (NB_j) and is independent of bubble length for a fixed channel and flow conditions. This model matches very well with our experimental results, and dislodging pressure profile for every channel in this network fits equation (7-8) with a very high R-Square value, as shown in Fig. 7.2.

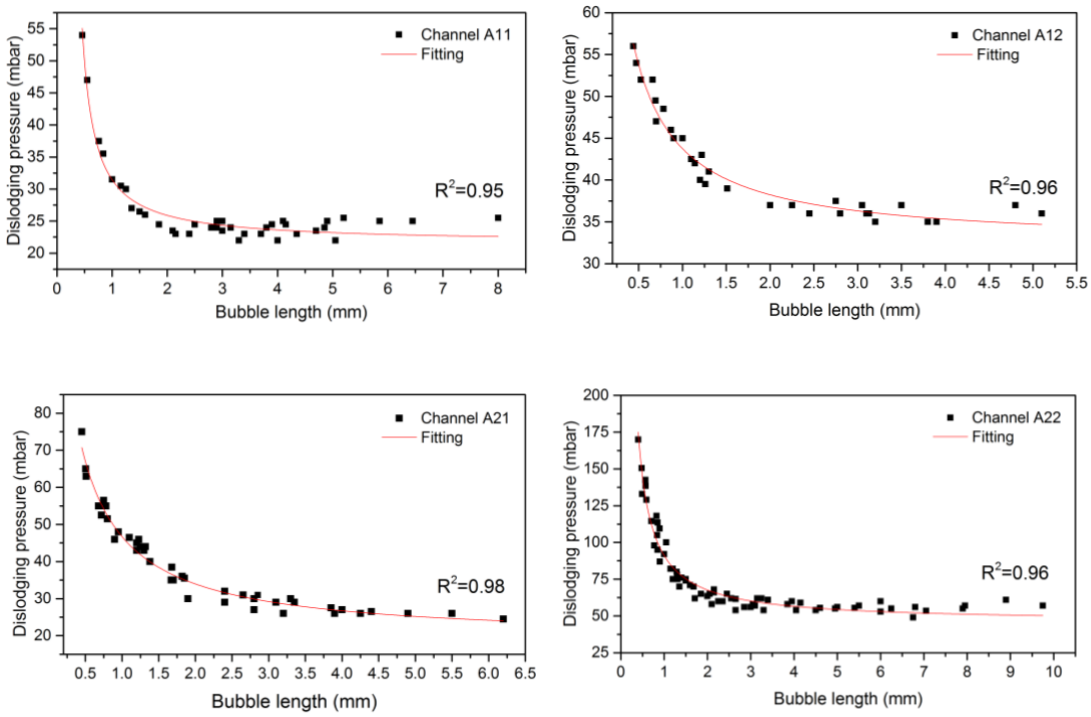

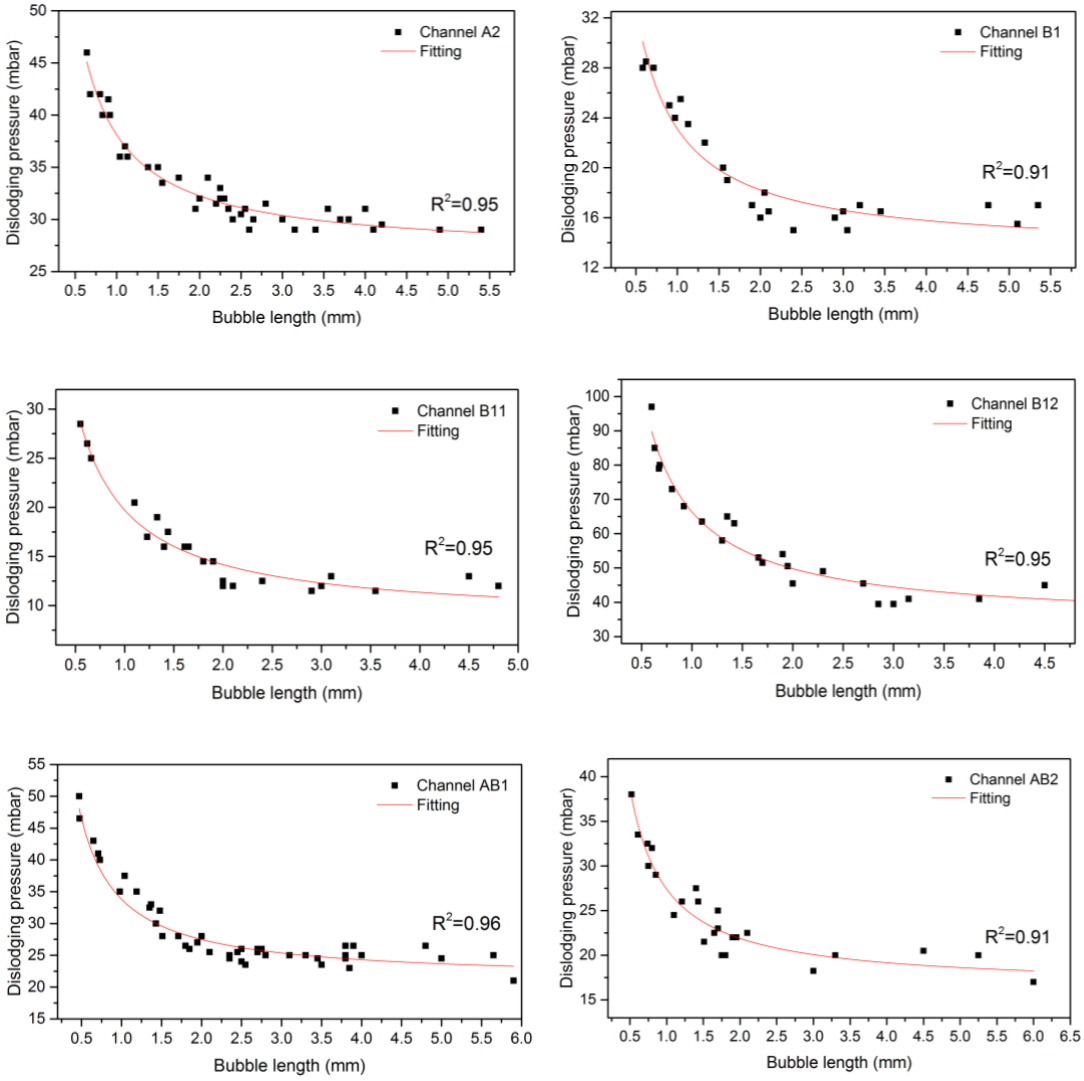

Fig. 7. 2 The plot of the bubble dislodging pressure profiles in different channels of the complex network A, and the red lines are the model-fitted values.

7.4 Effect of network structure on the dislodging pressure in Network A and Network B

Parameter c_j characterizes the contribution of the pressure drop in the bubble-lodged channel to the overall dislodging pressure when dislodging a bubble

from the microchannel *j* in the complex network. It also indicates the effect of surrounding channel (such as, channel dimension and geometry) and network structure on the flow resistance in the bubble-lodged channel. Based on the definition (Equation 7-6), the value of parameter c_j can be calculated as the ratio of pressure drop in the bubble-lodged microchannel *j* over the total dislodging pressure. The prediction of ΔP_j has been illustrated in the Chapter 6.3, and the total pressure drop (ΔP) was obtained experimentally.

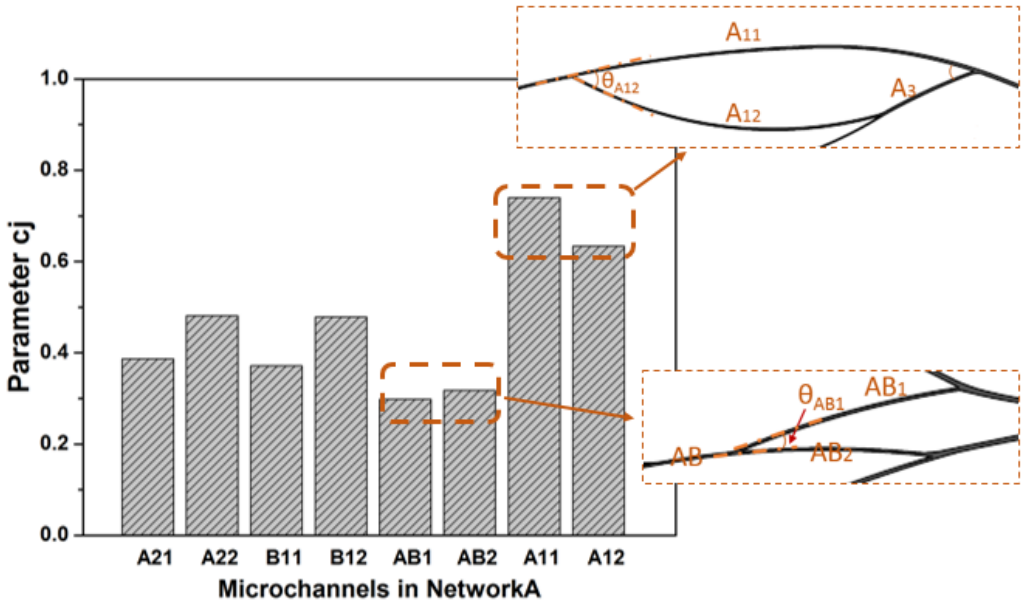

Fig. 7. 3 Magnitude of parameter c_j of different microchannels in Network A, and the illustration of the network structure around channels AB1, AB2 and A11, A12

Fig. 7.3 shows the magnitude of parameter c_j for different microchannels of Network A. The difference in c_j value is attributed to both the dimension of microchannel *j* and network structure surrounding the microchannel *j*. Generally, with the similar surrounding network conditions, the c_j value tends to be larger

if the bubble suffers a larger flow resistance from channel *j*, which may be caused by the smaller channel size and greater channel length. However, when two microchannels have similar dimensions, the c_j value will be smaller if the bubble is lodged in the channel with a more complicated surrounding network, such as multiple bifurcations and multiple microchannels. This is supported by the comparison of c_j value of channels AB1 and AB2, A11 and A12 in Network A. Channels AB1 and AB2 have the same width and height (W_{AB1}=W_{AB2}= 0.45 mm, H_{AB1}=H_{AB2}= 0.32 mm) and share the same inlet. The difference in the outlet condition of these two channels can be negligible as the outlet channel size is more than 1 mm which offering very low flow resistance to bubble motion. Channels A11 and A12 also have similar inlet and outlet flow conditions, and channel width and height are identical (W_{A11}=W_{A12}= 0.46 mm, H_{A11}=H_{A12}= 0.32 mm). The parameter c_j of channel AB1 (or channel A12) is smaller than that of channel AB2 (or channel A11). This demonstrates that the contribution of bifurcating angle to the magnitude of parameter c_j cannot be negligible.

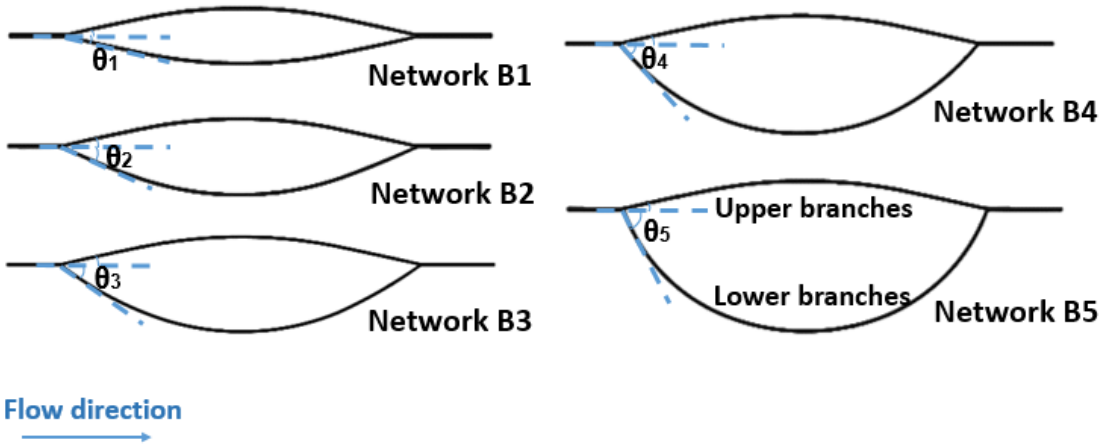

Fig. 7. 4 Schematics of Networks B1-B5 with various bifurcating angles (θ_1=12˚, θ_2=25˚, θ_3=38˚, θ_4=55˚ and θ_5=66˚); the terms 'upper' and 'lower' are defined based on the horizontal branch position, for easily describing the two branch of Network B.

In order to clarify the contribution of bifurcating angles to parameter c_j, Network B1-B5 which all have the identical widths and heights of upper and lower branches (0.4 mm) were used, and the schematics of the Networks B1-B5 were shown in Fig. 7.4. The branching angles (θ_1-θ_5) of Network B1-B5 range from 12- 66˚. The magnitude of c_j in Networks B1-B5 is obtained via the same method mentioned previously and verified through Equation (7-11) which is derived based on the Equation (7-7). The relationship of parameter c_j and MA_j is plotted in Fig. 7.5a, and the means of linear regression (R^2) shows that the parameter c_j in both upper and lower branches of Networks B is well predicted by employing the electric circuit theory.

$$c_j = \frac{L_j}{W_j H_j M A_j}\left(\frac{1}{W_j} + \frac{1}{H_j}\right) \quad (7\text{-}11)$$

For the upper branches of Networks B1- B5, the branches are of the same length and channel size, thus, given as,

$$c_j \propto \frac{1}{MA_j} \quad (7\text{-}12)$$

For the lower branches of Networks B1- B5, the branches are of the same channel size, and it gives,

$$c_j \propto \frac{L_j}{MA_j} \quad (7\text{-}13)$$

Fig. 7.5b illustrates how bifurcating angle affects the parameter c_j of the upper and lower branches in Networks B1- B5. It is observed that increasing the bifurcating angle of the lower branch will decrease its c_j value. When the bubble lodges in the lower channel, the flow resistance in the lower channel will increase with the increase of lower channel's bifurcating angle (from 12 to 66˚). This leads to a relatively lower ratio of liquid flowrate in the lower branch to the total flowrate, and thus a lower pressure drop ratio (i.e. c_j value). This not only is in a good agreement with the c_j comparison results among channel AB1 and AB2, A11 and A12 in Network A, but also clearly demonstrates how the bifurcating angle of microchannel *j* affects the c_j value of the channel *j*. When a bubble lodges in the branch with a higher bifurcating angle, the c_j value will be smaller, which indicates a greater impact of the network structure on the dislodging pressure.

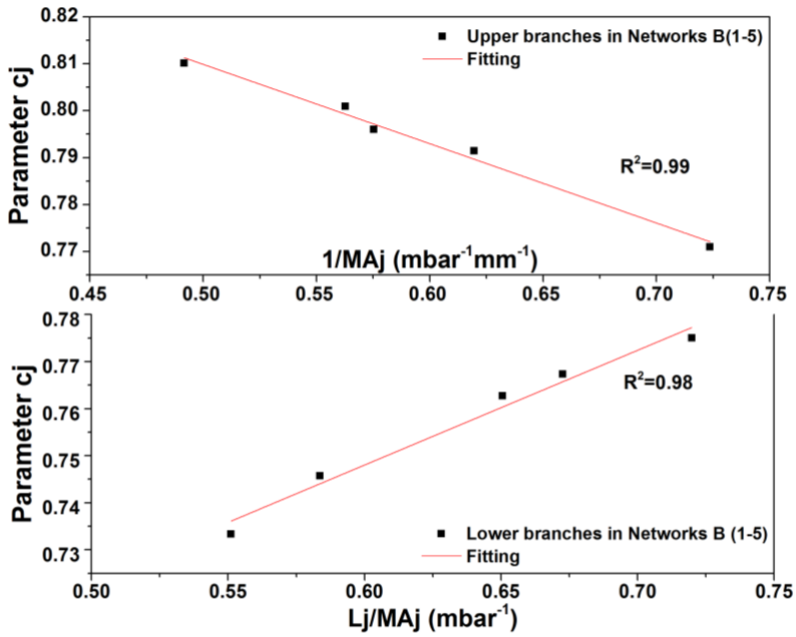

(a)

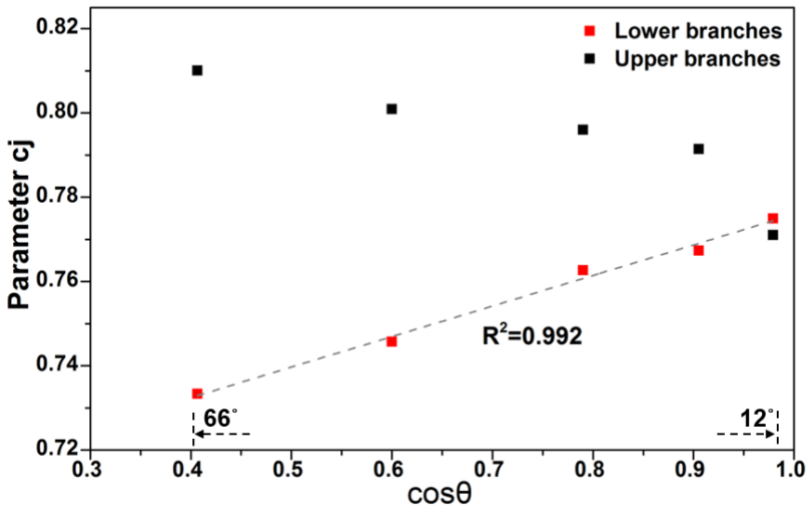

(b)

Fig. 7. 5 (a) Verification of parameter c_j of the upper and lower branches in Networks B1-B5, L_j is the length of the corresponding microchannel; (b) plot of c_j vs. $cos\theta$ for the upper and lower branches of Networks B1-B5

On the contrary, increasing the bifurcating angle of the lower branches will increase the c_j value of the upper branches, as shown in Fig. 7.5b. It suggests

that the c_j value of the microchannel *j* is also affected by the proximal channel. When a bubble lodges in the upper branch, increasing the bifurcating angle of lower branch (proximal channel) will increase the liquid flow resistance in the lower channel. Therefore, liquid allocated to the upper channel will be getting greater under the condition that the geometrical configuration of the upper branch stays the same. As the viscous pressure drop is proportional to the liquid flowrate, a higher ratio of flowrate in the upper branch to the overall flowrate indicates that its c_j value will increase correspondingly. Higher c_j value also suggests a smaller impact of the network structure on the bubble dislodgment. With the increase of the bifurcating angle of the proximal channel, the impact of the proximal channel on the dislodging pressure for bubbles lodged in the upper branch is getting smaller. This is possibly due to the increase of distance between the lower branch and the upper branch. Based on the investigation reported by Murakami et al.[29], when liquids flow in a microchannel with many elbows, the elbows interferes with the proximal elbows intensively when the distance between two elbows is less than 5 *L/D*, where *L* is the channel length, and *D* is the channel diameter. If the distance exceeds 10 *L/D*, the impact is considerably hindered. This inspires that there may be an effective distance between two branches, which determines if the interactions between two proximal channels take effect.

7.5 Summary

This chapter developed a theoretical model to illustrate the underlying physics of bubble dislodgment from capillary networks, and characterization of parameter c_j was accomplished in terms of the bifurcating angle through using Network B1-B5. The main findings are follows,

1. A one-dimensional model has been derived to predict the dislodging pressure, and fully describe the bubble dislodgement in complex capillary network in terms of bubble length, channel dimension, network structure. It explains the underlying physics of bubble dislodgment and the model agrees well with the experimental results in both complex Network A and Network B with a single bifurcation.

2. In the modelling, the parameter c_j evaluates the impact of network complexity on the dislodging pressure, and characterizes the distribution of the overall dislodging pressure to an individual channel where a bubble is lodged.

3. A small c_j value of a microchannel indicates a greater impact of network structure on the bubble dislodgment. The c_j value increases with the bifurcating angle of microchannel j, and a high bifurcating angle results in a decrease of c_j value of the proximal microchannel.

7.6 Reference

1. Varner, V.D. and C.M. Nelson. *Computational models of airway branching morphogenesis*. in *Seminars in cell & developmental biology*. 2017. Elsevier.
2. Wechsatol, W., S. Lorente, and A. Bejan, *Tree-shaped insulated designs for the uniform distribution of hot water over an area.* International Journal of Heat and Mass Transfer, 2001. **44**(16): p. 3111-3123.Doi 10.1016/S0017-9310(00)00338-0
3. Wang, X.Q., A.S. Mujumdar, and C. Yap, *Thermal characteristics of tree-shaped microchannel nets for cooling of a rectangular heat sink.* International Journal of Thermal Sciences, 2006. **45**(11): p. 1103-1112.10.1016/j.ijthermalsci.2006.01.010
4. Cygan, Z.T., et al., *Microfluidic platform for the generation of organic-phase microreactors.* Langmuir, 2005. **21**(8): p. 3629-34.10.1021/la0471137
5. Metzker, M.L., *Emerging technologies in DNA sequencing.* Genome Res, 2005. **15**(12): p. 1767-76.10.1101/gr.3770505
6. Sudarsan, A.P. and V.M. Ugaz, *Fluid mixing in planar spiral microchannels.* Lab Chip, 2006. **6**(1): p. 74-82.10.1039/b511524h
7. Marshall, I., et al., *MRI and CFD studies of pulsatile flow in healthy and stenosed carotid bifurcation models.* J. Biomech., 2004. **37**(5): p. 679-87.10.1016/j.jbiomech.2003.09.032

8. Prabhakarpandian, B., et al., *Bifurcations: focal points of particle adhesion in microvascular networks.* Microcirculation, 2011. **18**(5): p. 380-9.10.1111/j.1549-8719.2011.00099.x

9. Quintero, N.V., et al., *Behavior of liquid plugs at bifurcations in a microfluidic tree network.* Biomicrofluidics, 2012. **6**(3): p. 34105.10.1063/1.4739072

10. Wang, X.Q., A.S. Mujumdar, and C. Yap, *Effect of bifurcation angle in tree-shaped microchannel networks.* Journal of Applied Physics, 2007. **102**(7): p. 073530.Artn 07353010.1063/1.2794379

11. Calderón, A.J., J.B. Fowlkes, and J.L. Bull, *Bubble splitting in bifurcating tubes: a model study of cardiovascular gas emboli transport.* J. Appl. Physiol., 2005. **99**(2): p. 479-487,

12. Tadjfar, M. and F.T. Smith, *Direct simulations and modelling of basic three-dimensional bifurcating tube flows.* J. Fluid Mech., 2004. **519**: p. 1-32.10.1017/s0022112004000606

13. Eckmann, D.M. and D.P. Cavanagh, *Bubble detachment by diffusion-controlled surfactant adsorption.* Colloids and Surfaces a-Physicochemical and Engineering Aspects, 2003. **227**(1-3): p. 21-33.10.1016/S0927-7757(03)00375-3

14. Blackmore, B., D.Q. Li, and J. Gao, *Detachment of bubbles in slit microchannels by shearing flow.* Journal of Colloid and Interface Science, 2001. **241**(2): p. 514-520.10.1006/jcis.2001.7755

15. Chao, C., et al., *Bubble dislodgment in a capillary network with microscopic multi-channel and multi-bifurcation features.* Langmuir, 2019,

16. Suzuki, A., S.C. Armstead, and D.M. Eckmann, *Surfactant reduction in embolism bubble adhesion and endothelial damage.* Anesthesiology, 2004. **101**(1): p. 97-103.10.1097/00000542-200407000-00016

17. Suzuki, A. and D.M. Eckmann, *Embolism bubble adhesion force in excised perfused microvessels.* Anesthesiology, 2003. **99**(2): p. 400-8, http://www.ncbi.nlm.nih.gov/pubmed/12883413

18. Lamberti, G., et al., *Adhesion patterns in the microvasculature are dependent on bifurcation angle.* Microvasc Res, 2015. **99**: p. 19-25.10.1016/j.mvr.2015.02.004

19. Mohammadi, M. and K.V. Sharp, *The Role of Contact Line (Pinning) Forces on Bubble Blockage in Microchannels.* J Fluids Eng, 2015. **137**(3): p. 0312081-312087.10.1115/1.4029033

20. Wong, C.W., et al., *Transient capillary blocking in the flow field of a micro-DMFC and its effect on cell performance.* Journal of the Electrochemical Society, 2005. **152**(8): p. A1600-A1605.10.1149/1.1949067

21. Ma, S.X., G. Mason, and N.R. Morrow, *Effect of contact angle on drainage and imbibition in regular polygonal tubes.* Colloids and Surfaces a-Physicochemical and Engineering Aspects, 1996. **117**(3): p. 273-291.Doi 10.1016/0927-7757(96)03702-8

22. Walsh, E., et al., *Pressure drop in two phase slug/bubble flows in mini scale capillaries.* International Journal of Multiphase Flow, 2009. **35**(10): p. 879-884.10.1016/j.ijmultiphaseflow.2009.06.007

23. Chung, P.M.Y. and M. Kawaji, *The effect of channel diameter on adiabatic two-phase flow characteristics in microchannels.* International Journal of Multiphase Flow, 2004. **30**(7-8): p. 735-761.10.1016/j.ijmultiphaseflow.2004.05.002

24. Kreutzer, M.T., et al., *Multiphase monolith reactors: Chemical reaction engineering of segmented flow in microchannels.* Chemical Engineering Science, 2005. **60**(22): p. 5895-5916.10.1016/j.ces.2005.03.022

25. Younes, A., I. Hassan, and L. Kadem, *Investigation of Bubble Frequency for Slug Flow Regime in a Uniformly Heated Horizontal Microchannel.* Journal of Heat Transfer-Transactions of the Asme, 2017. **139**(6): p. 061501.Artn 06150110.1115/1.4035562

26. Yue, J., G.W. Chen, and Q. Yuan, *Pressure drops of single and two-phase flows through T-type microchannel mixers.* Chemical Engineering Journal, 2004. **102**(1): p. 11-24.10.1016/j.cej.2004.02.001

27. Kawahara, A., P.M.Y. Chung, and M. Kawaji, *Investigation of two-phase flow pattern, void fraction and pressure drop in a microchannel.* International Journal of Multiphase Flow, 2002. **28**(9): p. 1411-1435.Pii S0301-9322(02)00037-X Doi 10.1016/S0301-9322(02)00037-X

28. You, L.X. and H.T. Liu, *A two-phase flow and transport model for the cathode of PEM fuel cells.* Int. J. Heat Mass Tran., 2002. **45**(11): p. 2277-2287.Pii S0017-9310(01)00322-2 Doi 10.1016/S0017-9310(01)00322-2

29. Murakami, M., Y. Shimizu, and H. Shiragami, *Studies on fluid flow in three-dimensional bend conduits.* Bulletin of JSME, 1969. **12**(54): p. 1369-1379,

Chapter 8 Conclusions and future works

The main goal of this thesis is to advance the understanding of the flow resistance to multiphase flows in porous media at pore scale, the impact of network complexity on the pressure drop, and bubble dislodgment from pore network. The results obtained are of fundamental primary importance for the design of microfluidics, the enhanced oil recovery and microbubble-aided drug delivery.

8.1 Effect of interfaces on the two-phase flows in constricted microchannels

Capillary resistance to two-phase flows is mainly arisen from the capillary force acting on the two-phase interface, rather than on the body of the single phases. Capillary resistance to a two-phase interface occurs only when the pore diameter is smaller than a certain value. We defined this “certain value” as the ‘effective pore throat’ at which the capillary force starts to take effect on two-phase interface, therefore contributing to the pressure drop.

Simulations of pressure drop for two-phase flows in constricted capillaries have been conducted through using newly-derived Darcy-Weisbach equation combined with homogenous flow model and separated flow model. The predicted results have been compared with measured experimental data, and it was found that the simulation results agree well when the interface travels to the section of the microchannel with the pore diameter less than the effective pore throat. However, the predicted data

cannot identify the effective pore throat of a constricted microchannel, and cannot explain the sudden increase in the pressure drop at the effective pore throat. The effective pore throat and the sudden increase in the resistant pressure profiles can be qualitatively explained by the pore contact angle published by our group.

The effect of gas type, surface tension, fluid viscosity, capillary gradient and capillary tip diameter on the size of effective pore throat of a constricted capillary has been investigated in detail. It was found that under the same flow conditions and microchannel, a larger surface tension of gas-liquid interface has a relatively larger size of effective pore throat. The effect of surface tension on the pressure drop for two-phase flows takes effect only after the effective pore throat, and a larger surface tension gives a larger resistance in the constricted section of the capillary. For the flow path with a pore diameter greater than the effective pore throat, the pressure drop to the two-phase flows is mainly governed by the capillary tip size, rather than the surface tension. For air, CO_2 and CH_4 flows in constricted capillaries, the effective pore throat diameter is very similar for three types of gas-water flows due to the similar surface tensions of three gases. Viscosity significantly affects the magnitude of the pressure drop in fluids flows, but does not affect the diameter of the effective pore throat. The effective pore throat sizes linearly increase with the capillary tip diameter and capillary gradient within a certain range.

8.2 Dislodgment of bubbles from the complex networks

Interfaces, like bubbles in fluids flows will increase the flow resistance through the complex networks. As the bubble are easily accumulated in PMMA/ PDMS based

microfluidic devices, which is harmful for the systems performance, bubble dislodgment is necessary to investigate. The bubble dislodging pressure reflects the effect of the interface on the flow resistance in complex networks.

From the experimental results, it was found that the bubble dislodging pressure is decreased with the increase of the bubble length when the length is less than a certain value. Once the bubble length is greater than this certain value (2 mm in this study), the dislodging pressure is almost constant and independent of the bubble length. The reciprocal relationship between the channel diameter and pressure drop may not apply in complex network with high interconnectivity. The bubble dislodging pressure is also increased with the increase in the complexity of the network structure. Specifically, the pressure is greater for the channels with a larger diverging and/or converging angles when the channels have similar size and flow conditions.

One theoretical model has been developed to predict the dislodging pressure in terms of bubble length, channel dimension, network structure, surface tension and fluid viscosity. It fully illustrates the underlying physics of bubble dislodgment from capillary networks with multi-microchannel and micro-bifurcation features. The high value of R^2 indicates that the model agrees well with the experimental results in both complex network and the network with one bifurcation. The parameter c_j is introduced to characterize the distribution of an individual channel where the bubble is lodged to overall dislodging pressure. It also suggests the impact of network complexity on the bubble dislodging pressure. Combined the experimental results with the theoretical equation, the value of parameter c_j was found to increase with the bifurcating angle of microchannel j, and a high bifurcating angle results in a decrease of c_j value of the proximal microchannel.

8.3 Limitations and future works

- Due to the limitations of optical microscope used in this study, the measurement errors on pore diameter in small microchannels are larger than in large microchannels. The contact angle measurements are not so accurate as it is difficult to obtain a clear meniscus image when the interface travels in the constricted section of the microchannels. In the future, we should improve the microscopic measurement technique to minimize the distortion effect on meniscus in a pore and thus improve the measurement accuracy in small microchannels.
- Some conditions in this experiment are far away from the real conditions in practical applications, such as oil reservoirs and blood vessels. The channel diameters of the constricted capillaries and microfluidic network used in this study are not small enough, thus future work relating to channel diameter which is smaller to tens of microns should be conducted to simulate the real pore in oil reservoir and tiny capillaries for practical applications. For medical application, more bio-related materials (such as PDMS, PLA) can be used to fabricate the lab-on-a-chip platforms, and biocompatible microbubbles, blood-analog liquid should be employed and the experiments can be conducted at the human body temperature in the future work to mimic more appropriate conditions in blood vessels. In addition, ultrasound can be introduced to guide the drug-loaded bubble movement in microfluidic devices for the precise control of bubble movement, bubble stability and release of therapeutic chemicals to targeted sites.

- The microfluidic devices manufactured through laser techniques have rectangular cross-section. It is worth to find a method to manufacture the network with cross section of circular or other irregular shapes, and investigate the effect of pore shape on the bubble dislodging pressure. In addition, as the PMMA plate has been etched by the laser to fabricate the channel, the surface of microchannel is actually not ideal. The roughness of the surface is one important factor affecting the bubble dislodging pressure, requiring further investigations and roughness measurement through AFM or other techniques.
- Simulation work related to the prediction of pressure drop for two-phase flows in the constricted capillaries requires further investigations. Three-dimensional computational fluid dynamics (CFD) may be employed to simulate the flow conditions in microchannels and complex networks. The effect of network structure on the flow resistance will be investigated more systematically, and equation that expresses the relationship of the parameter c_j and network structure may be derived and can be applied in other network with different structures.